Analysis and manipulation of field inhomogeneity effects in magnetic resonance imaging

H. de Leeuw

Colophon

This thesis was typeset by the author using LaTeX 2_ε.

Analysis and manipulation of field inhomogeneity effects in magnetic resonance imaging.
H. de Leeuw - Utrecht, University Medical Center Utrecht.

PhD thesis Utrecht University - with a summary in Dutch.
Cover design: Hendrik de Leeuw.

This research was financially supported by the Dutch Technology Foundation STW (06648). Financial support for publication of this thesis was kindly provided by Philips Healthcare, Elekta B.V., and Röntgenstichting Utrecht.

Printed by Ipskamp Drukkers, Enschede, The Netherlands

ISBN: 978-90-393-5862-7

Analysis and manipulation of field inhomogeneity effects in magnetic resonance imaging

Analyse en manipulatie van de effecten van veldinhomogeniteiten bij magnetische resonantie beeldvorming

(met een samenvatting in het Nederlands)

PROEFSCHRIFT

ter verkrijging van de graad van doctor aan de
Universiteit Utrecht op gezag van de rector magnificus,
prof.dr. G.J. van der Zwaan,
ingevolge het besluit van het college voor promoties
in het openbaar te verdedigen op
donderdag 22 november 2012 des middags te 2.30 uur

door

Hendrik de Leeuw
geboren op 09 augustus 1984, te Schoonrewoerd

Promotor:	Prof. dr. ir. M.A. Viergever
Co-promotor:	Dr. C.J.G. Bakker

Creating a new theory is not like destroying an old barn and erecting a skyscraper in its place. It is rather like climbing a mountain, gaining new and wider views, discovering unexpected connections between our starting points and its rich environment. But the point from which we started out still exists and can be seen, although it appears smaller and forms a tiny part of our broad view gained by the mastery of the obstacles on our adventurous way up

---

A. Einstein

Contents

He who loves practice without theory
is like the sailor who boards ship
without a rudder and compass and
never knows where he may cast

Leonardo da Vinci

CHAPTER 1

Introduction

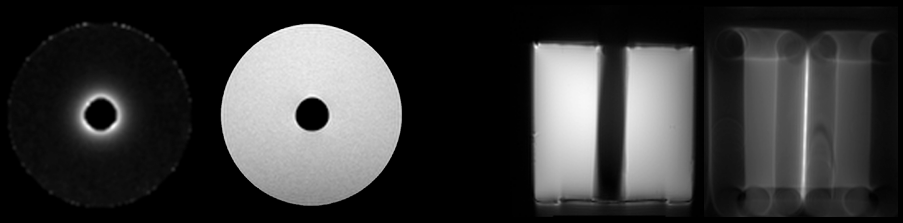

1.1 Outline

This thesis is concerned with the analysis and manipulation of the effects of macroscopic field inhomogeneities in MR imaging. In this introductory chapter an overview of a number of essential physical principles needed to appreciate the subject matter is provided. The first section describes the principles of signal formation in MRI. Furthermore, the main parameters governing the signal strength are discussed, including the spin density, the relaxation parameters R_1 and R_2, and microscopic, mesoscopic and macroscopic characteristics of the local magnetic field in the volume of interest. In the second section a 1D imaging experiment on a 1D object is described. This simple setup illustrates two basic schemes that may be used to encode the signal viz. frequency and phase encoding. Expressions are derived for the signal intensity in the reconstructed images in a homogeneous magnetic field and in the presence of macroscopic field inhomogeneities, respectively. The same exercise is subsequently repeated for a full 3D experiment. In this case, expressions for the reconstructed signal are derived for both Cartesian and radial sampling schemes. In the final section an outline of the topics discussed in the thesis is provided.

1.2 MR signal and contrast parameters

In this section, first the basic principles of the generation of signal in an MR experiment are discussed. This description is followed by an overview of the main parameters governing signal strength and contrast in MR imaging, with an emphasis on the role of magnetic field inhomogeneities.

1.2.1 Signal formation

Hydrogen protons (^{1}H) exhibit a nuclear spin. In the presence of a magnetic field, the nuclei start to precess around the magnetic field with the Larmor frequency:

$$\omega_0 = \gamma B_0 \tag{1.1}$$

with ω_0 the angular precession frequency in radians per second, B_0 the magnetic field strength in Tesla and γ the gyromagnetic ratio (268 MHz/T for ^{1}H). When a sample containing protons is placed into a homogeneous external magnetic field, the potential energy of proton spins aligned parallel with the magnetic field is lower than for proton spins aligned anti-parallel. The difference in potential energy of the spins aligned parallel and the spins aligned anti-parallel causes a net magnetization within the object. This net magnetization can be manipulated and converted into an observable signal. The equations of motion of the nuclear magnetization are given by the Bloch equations [1]:

$$\frac{dM_z}{dt} = R_1(M_0 - M_z) \tag{1.2}$$

$$\frac{dM_x}{dt} = \omega_0 M_y - R_2 M_x \tag{1.3}$$

$$\frac{dM_y}{dt} = -\omega_0 M_x - R_2 M_y \tag{1.4}$$

where M_0 denotes the equilibrium magnetization and M_z, M_x and M_y the longitudinal magnetization, the in-phase and out-of-phase component of the transverse magnetization, respectively. Further, R_1 and R_2 represent the longitudinal relaxation rate and transverse relaxation rate, respectively and ω_0 denotes the local resonance frequency, as described by Equation 1.1. The equilibrium magnetization M_0 is proportional to the spin density ρ, but also depends on the magnetic field strength, the detection hardware and the

temperature of the studied volume. The evolution of the magnetization over time, as expressed by Equations 1.2-1.4, describes the relation between the signal relaxation parameters R_1, R_2, the effective spin density and the local frequency ω_0. Ideally, the magnetic field within the sample is homogeneous, however, local variations of the magnetic field can be induced by objects, caused by non-idealities of the imposed field and originate from deliberately applied field or frequency offsets [2–4].

By applying an radiofrequency (RF) pulse, at the Larmor frequency, along an axis perpendicular to the main magnetic field, the spin isochromats start to precess around a different axis. The axis around which the spins start to precess is defined by the main magnetic field and the direction along which the RF pulse is applied. The duration and amplitude of the RF pulse together define the flip angle, the magnitude with which the spins are brought out of equilibrium [5, p40-43]. After the spins are brought out of equilibrium onto the transverse plane, the magnetization in the transverse plane evolves as governed by Equations 1.3, 1.4. However, at the same time the magnetization also returns to equilibrium, as described by Equation 1.2. By repeating the RF pulse several times, with repetition time (TR) between subsequent RF pulses, the transverse magnetization is brought into a steady state. For a 90° RF pulse and TR$\gg 1/R_2^\star$ this results in the following expression:

$$s(x', TE) = \rho_{eff}(x') e^{-R_2^\star(x')\mathrm{TE}} (1 - e^{-\mathrm{TR}\cdot R_1(x')}) \tag{1.5}$$

with x' the location at which the magnetization is observed, $\rho_{eff}(x')$ the effective spin density at location x' and the signal is acquired at time t=TE. The RF pulse can be applied prior to as well as during an experiment. For example, a 180° RF-pulse at t=TE/2 can be applied to invert all effects on the signal phase so as to create a spin echo at the time of encoding, i.e. t=TE [5, p118].

1.2.2 Longitudinal and transverse relaxation and spin density

The R_1 longitudinal relaxation rate represents the interaction of spins with the environment. The longitudinal relaxation governs the speed with which the spin ensemble returns to equilibrium after being perturbed from this equilibrium. The transverse signal relaxation rate, R_2, represents spin-spin interactions. The transverse relaxation rate determines the speed with which signal is lost within the transverse plane. Under all circumstances $R_2 \geq R_1$. The effective spin density ρ_{eff} is a measure for the net number of protons

per unit volume that contribute to the observed signal. This net number of protons is, amongst others, proportional to the resonance frequency, the spin density and the gyromagnetic ratio and is inversely proportional to the temperature of the volume studied [5]. Often, the effective spin density is used in which the detection hardware is incorporated. The spin density as well as the relaxation parameters are tissue dependent and therefore form the basic contrast mechanisms in MR imaging. The longitudinal relaxation depends on the strength of the main magnetic field [6]. Furthermore, the net magnetization and, therefore, the signal-to-noise ratio is approximately linearly proportional to the strength of the main magnetic field [5].

1.2.3 Local variations of the Larmor frequency

In a homogeneous sample and a homogeneous magnetic field, e.g. within an infinite cylinder or a sphere, the Larmor frequency is constant. On the other hand, variations of the magnetic field and heterogeneities within a sample can cause variations of the Larmor frequency. The local variations of the Larmor frequency are caused by differences in the magnetic shielding of nuclei in different chemical environments or object induced perturbations and system-related variations of the magnetic field [2]. The magnetic field offsets are usually induced by local variations of the magnetic susceptibility that induce a magnetic field, which affects an area larger than the area over which the susceptibility variations occur [2]. The expressions for the local frequency offset due to chemical shift and field inhomogeneity are given by:

$$\Delta\omega_{cs} = \gamma\sigma B_0 \tag{1.6}$$

$$\delta\omega_{susc} = \gamma\delta B(B_0, \Delta\chi) \tag{1.7}$$

with σ the chemical shift and δB the local magnetic field offset in T induced by the magnetic volume susceptibility offset $\Delta\chi$. The chemical shift between water and fat, for example, is approximately 3.34ppm [2]. The susceptibility is in general interpreted with respect to the susceptibility of water, which is approximately -9 ppm [2]. For example, blood is relatively paramagnetic when it is deoxygenated, oxygenated blood, on the other hand, is weakly diamagnetic. In other words, the exact susceptibility of blood depends on the oxygen level in the blood [7]. Another example is calcified tissue, which is diamagnetic with a magnetic susceptibility in the order of -11.4ppm [8].

The induced magnetic field offset depends on the shape, the volume and the orientation of the susceptibility distribution with respect to the main

magnetic field. Moreover, frequency offsets can be caused by the chemical composition of a molecule, which causes variations of the chemical shift [2] or field fluctuations on the short range level e.g. the Lorentz correction [9]. The susceptibility regimes consists of diamagnetic materials, which induce weak decreases of the local magnetic field ($-10^{-2} < \chi < 0$), paramagnetic materials that weakly increase the magnetic field ($0 < \chi < 10^{-2}$) and ferromagnetic materials that increase the magnetic field ($\chi > 10^{-2}$) [2].

1.2.4 Relaxation and field inhomogeneities

As illustrated by Equation 1.2, the longitudinal relaxation does not depend on the local precession frequency [5]. Variations of the magnetic field in a sample will therefore not affect the R_1. On the other hand, the transverse relaxation does depend on the local resonance frequency. The evolution of the transverse magnetization, as given by Equation 1.3 and 1.4, depends on the intrinsic R_2 decay and the local magnetic field. The observed transverse relaxation rate therefore reflects macroscopic, mesoscopic and microscopic effects, as schematically illustrated in Figure 1.1

The first mechanism, irreversible R_2 relaxation, characterizes molecular effects and is illustrated in Figure 1.1a. The R_2 signal relaxation is caused by variations of the magnetic field over distances smaller than the diffusion length of the protons, which result in signal loss. The R_2 relaxation therefore reflects an intrinsic tissue property [10–12]. Variations of the magnetic field over distances larger than the diffusion length, but smaller than the voxel size are the so called mesoscopic field inhomogeneities. The mesoscopic field inhomogeneities, which are illustrated in Figure 1.1b, reflect local tissue characteristics, that are usually induced by differences of the susceptibility within tissue. Familiar examples include micro-calcifications in breast tissue [13–15], microbleedings in the brain [16], tissues after uptake of $R_2^\star$-contrast agents [17], and deoxygenation of blood during activation [18]. Mesoscopic field inhomogeneities are characterized by the $R_2^{'}$ relaxation rate. $R_2^{'}$ is often applied to asses disease status, since it reflects local tissue changes [11, 12].

Macroscopic field inhomogeneities characterize changes of the magnetic field over distances larger than the voxel size [11, 19], which include object induced magnetic field disturbances invoked by, e.g., hemorrhagic lesions and micro-calcifications, system imperfections, e.g. residual field gradients after shimming, and field inhomogeneities at extremities of the body, e.g., at the back of the head [20]. Other, more extreme, examples of macroscopic field inhomogeneities are typically observed near air tissue interfaces, e.g.,

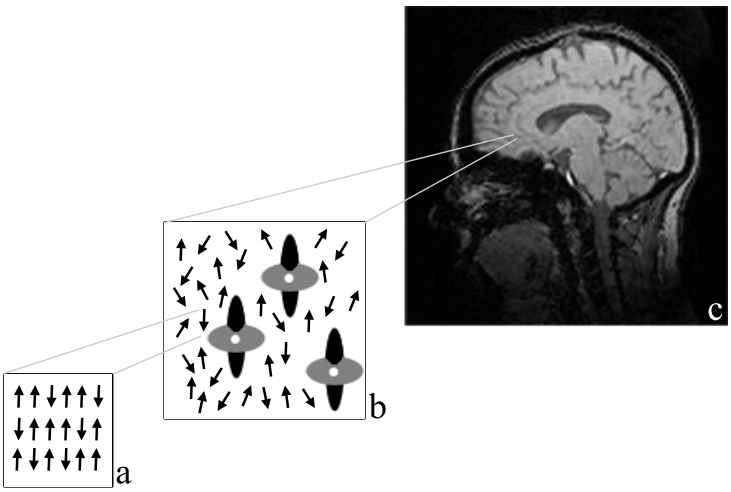

Figure 1.1: The three mechanisms that contribute to the effective transverse relaxation rate $R_2^\star$: relaxation due to microscopic, mesoscopic and macroscopic field inhomogeneities. The left image (a) shows the smallest scale, the microscopic scale. At the microscopic scale the (R_2) signal relaxation reflects interactions of individual spins. The middle image (b) illustrates mesoscopic signal dephasing, which reflects local variations of the magnetic field due to field perturbing structures within a voxel. Mesoscopic inhomogeneities are reflected by the R_2'-relaxation rate. The right image (c) shows the scale of the macroscopic field inhomogeneities, which span over areas larger than an imaging voxel. Macroscopic field inhomogeneities are determined by the susceptibility distribution as a whole. Macroscopic field inhomogeneities can, for example, be found near the nasal cavity. The sum of relaxation rates, induced by the inhomogeneities at the three ranges, composes the total ($R_2^\star$) relaxation rate i.e.

$$R_2^\star = R_2 + R_2^{'} + R_{2,macro}^\star.$$

near the lungs or at the nasal cavity, near metallic implants or near external devices. The observed relaxation rate, which includes microscopic, mesoscopic and macroscopic signal dephasing, is characterized by the effective relaxation rate $R_2^\star$: $R_2^\star = R_2 + R_2' + R_{2,macro}^\star$. As the signal is proportional to the transverse magnetization, the transverse relaxation results in an exponential reduction of the signal intensity, as illustrated in Equation 1.5. However, the

exact shape of the signal dephasing induced by macroscopic dephasing is determined by the magnetic field and is not in all cases exponential [21].

Despite differences in the spatial range over which the signal is affected, the effects of the mesoscopic and macroscopic field inhomogeneities are not easily discriminated. Many techniques have been developed to distinguish microscopic, mesoscopic and macroscopic dephasing [12, 22]. The effect of the macroscopic signal dephasing can be assessed by integrating the phase derivative over an image voxel. In chapter 4 we show that, by dividing the signal by the estimation of the signal loss, the macroscopic dephasing can be reduced, while maintaining the mesoscopic signal dephasing [23].

1.3 MRI in the presence of field inhomogeneities

In this section first a 1D imaging experiment on a 1D object is described. This simple setup serves to illustrate two basic encoding schemes that may be used to obtain an image, viz. frequency encoding and phase encoding. An expression for the signal intensity is derived in a homogeneous magnetic field and in the presence of macroscopic field inhomogeneities. Next, the same exercise is done for a full 3D imaging experiment. In this description, the derivation of the reconstructed signal includes both Cartesian sampling schemes and radial sampling schemes.

1.3.1 1D imaging of a 1D object

To describe signal acquisition in 1D, consider the two general 1D encoding schemes sketched in Figure 1.2. The sequence consists of three stages. First, transverse magnetization is created in the studied object by applying an RF pulse. Second, the magnetization is left to evolve and can be manipulated. Examples of the manipulation include signal encoding, e.g., the light gray field gradient in Figure 1.2a, and the formation of a spin echo by applying a 180° RF pulse to refocus the signal phase and to regain the signal loss induced by reversible signal dephasing (R_2', $R^\star_{2,macro}$). At the echo time TE, a spin echo is unaffected by field inhomogeneities and therefore the signal decay is only determined by the R_2-decay. The FID signal decays with $R^\star_2$. Third, the signal is sampled at a single time point (phase encoding, Figure 1.2a) or during N time intervals (frequency encoding, Figure 1.2a). Phase encoding requires N acquisitions, which apply different amplitudes of the encoding gradient. Frequency encoding results in an increase of efficiency, since each sample corresponds to a different encoding step.

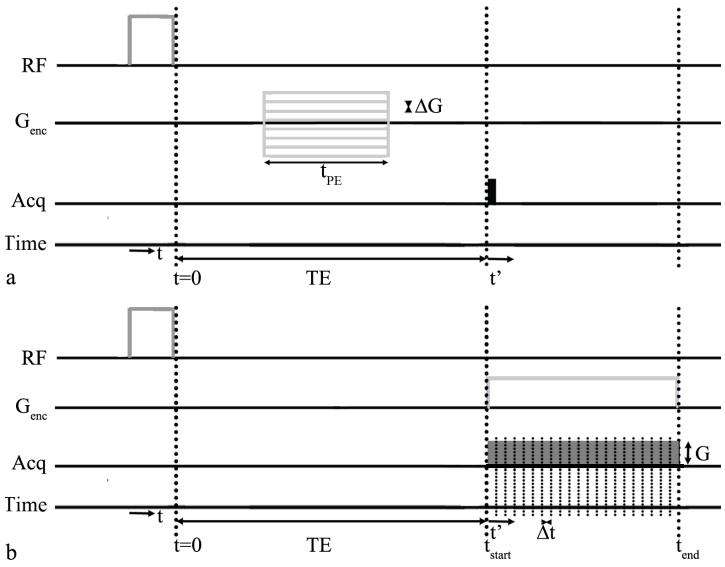

Figure 1.2: Two 1D pulse sequences, consisting of a radio-frequency pulse (first row), signal encoding (second row) and signal acquisition (third row). Shown are a phase encoded acquisition (image a) and a frequency encoded acquisition of a free induction decay (FID, image b). The pulse sequences can be subdivided into three intervals. During the first interval, an RF pulse is applied to generate transverse magnetization. During the second stage the magnetization evolves and can be manipulated, e.g., to encode the signal. During the third interval signal is sampled, which is optionally combined with encoding. Phase encoding applies a magnetic field gradient during the second stage (light gray box, image a) after which the signal is acquired at a single point (t'=0). This experiment is repeated N times during which the strength of the magnetic field gradient is varied with step size ΔG. During frequency encoding (image b) signal is acquired (N steps, width Δt), while a magnetic field gradient (light gray box, image b) is applied over the studied volume.

The encoded signal, obtained by both encoding schemes illustrated in Figure 1.2, is given by:

- Phase encoding:

$$S_{acq}(G) = \int_{V_{x'}} dx' s(x', TE) e^{-2\pi i \gamma t_{PE} G \cdot x'}$$
$$= S(k) = \int_{-\infty}^{\infty} dx'\ s(x', TE) rect\left(\frac{x' - x'_{c,exc}}{FOV}\right) e^{-2\pi i k \cdot x'} \quad (1.8)$$

  with $k = \gamma G t_{PE}$

- Frequency encoding:

$$S_{acq}(t') = \int_{V_{x'}} dx'\ s(x', TE) e^{-2\pi i \gamma t' G \cdot x'}$$
$$= S(k) = \int_{-\infty}^{\infty} dx'\ s(x', TE) rect\left(\frac{x' - x'_{c,exc}}{FOV}\right) e^{-2\pi i k \cdot x'} \quad (1.9)$$

  with $k = \gamma G t'$

with S_{acq} the acquired signal as a function of the gradient amplitude G or sampling rate t', $V_{x'}$ is the 1D excited volume, γ the gyromagnetic ratio (γ) divided by 2π, TE the echo time as depicted in Figure 1.2, t' the time during signal acquisition, t_{PE} the duration of the phase encoding, $rect$ the rectangular function, $x'_{c,exc}$ the center of the 1D excited volume, and s(x',TE) denotes the signal amplitude before signal acquisition, as given by Equation 1.5. The expressions for the acquired signal in Equation 1.8, 1.9 reflects a Fourier transform. The signal intensity, for each location in an image ($\hat{s}$(x)), is therefore obtained by an inverse Fourier transform of the acquired signal.

The signal acquisition, however, is done using sampling of the Fourier space in a limited interval. The sampling mathematically corresponds to a multiplication by a number of delta functions. The reconstructed signal intensity therefore corresponds to the true signal intensity convoluted with the inverse Fourier transform of the windowing function:

- Phase encoding:

$$\hat{s}(x) = s(x, TE) * SF(x) \quad (1.10)$$

- Frequency encoding:

$$\hat{s}(x) = s(x, TE) * SF(x) \quad (1.11)$$

with $\hat{s}$ the signal after image reconstruction and the sampling function SF(x) given by [5, p270-271]:

$$SF(x) = W\frac{sinc(\pi Wx)}{sinc(\pi\Delta kx)}e^{-i\pi\Delta kx} \tag{1.12}$$

where W is the width of the k-space and Δk the sampling step size. The sampling step size is defined by the incremental change in gradient strength ($\Delta k = \gamma\Delta G t_{PE}$) for phase encoding or, in case of frequency encoding, the step during the sampling ($\Delta k = \gamma G_x \Delta t'$). In the derivation of Equation 1.10 and 1.11, the signal relaxation during signal acquisition was considered to be zero. Transverse relaxation during the signal acquisition would result in an additional convolution of the reconstructed signal with the Fourier transform of signal decay over the sampling window [5, p286-287].

As illustrated by the expressions in Equation 1.10 and 1.11, the signal after image reconstruction provides an adequate representation of the object, for the phase encoded signal as well as the frequency encoded signal, as long as the magnetic field is homogeneous. However, the expressions for the phase encoded signal and frequency encoded signal differ in the presence of field inhomogeneities:

- Phase encoding:

$$S_{acq}(G) = \int_{V_{x'}} dx' s(x', TE) e^{-i\delta\omega(x')TE} e^{-2\pi i\gamma t_{PE} G\cdot x'} \tag{1.13}$$

  with $k = \gamma G t_{PE}$

- Frequency encoding:

$$S_{acq}(t') = \int_{V_{x'}} dx'\ s(x', TE) e^{-i\delta\omega(x')TE} e^{-2\pi i\gamma t' G\cdot x'} e^{-i\delta\omega(x')t'} \tag{1.14}$$

  with $k = \gamma G t'$

As the excitation of a volume ($V_{x'}$) is usually performed on a frequency basis, e.g., by applying a gradient while using an RF pulse with a limited bandwidth, field inhomogeneities and chemical shift can result in distortion of an imaged volume [24]. In the presence of frequency offsets the signal intensity after reconstruction is given by:

- Phase encoding:

$$\hat{s}(x) = s(x, TE)e^{-i\delta\omega(x)TE} * SF(x) \tag{1.15}$$

- Frequency encoding:

$$\hat{s}(x) = s(x + \delta x, TE)e^{-i\delta\omega(x+\delta x)TE} * SF(x) \tag{1.16}$$

with the sampling function as given by Equation 1.12 and δx given by:

$$\delta x = \frac{\delta\omega(x)}{\gamma G} \tag{1.17}$$

A frequency perturbation results in a phase offset to the reconstructed signal. However, the frequency encoded signal is, unlike the phase encoded signal, shifted spatially due to the frequency offset. This property of the two encoding schemes is illustrated in chapter 8. The efficiency gain obtained by frequency encoding is sometimes sacrificed for applications that require a high geometric fidelity.

The phase offset induced by a frequency offset has consequences for the reconstructed signal intensities in images. The image consists of voxels with size Δx. A field gradient, which results in a phase gradient, thereby induces signal loss.

$$\hat{s}_{voxel}(x_{vox}) = \hat{s}(x, TE)\, e^{i\gamma G_{\delta B} x_{vox} TE}\, \Delta x\, sinc(\gamma G_{\delta B} \frac{\Delta x}{2} TE) \tag{1.18}$$

with $G_{\Delta B}$ the magnetic field gradient and x_{vox} the center of the voxel. The sinc-function in Equation 1.18 shows that a field gradient results in signal loss, the so called intra-voxel signal dephasing [21]. In chapter 5 the intra voxel signal dephasing is assessed by integrating the phase derivative over a voxel. By dividing the signal by the estimate for the dephasing, the signal loss is shown to be reduced.

1.3.2 Imaging of a 3D object

In the previous section, the 1D signal acquisition applied phase encoding or frequency encoding. Signal encoding in 2D and 3D can be obtained by using combinations of the 1D encoding methods. A 2D imaging experiment can apply an RF pulse with limited bandwidth, while applying a field gradient

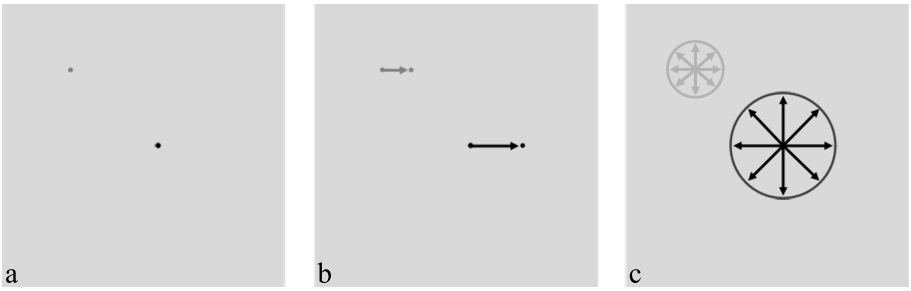

Figure 1.3: 2D image in which two locations are highlighted by a dot. Both locations experience a different chemical shift, the chemical shift at the gray dot is smaller than the chemical shift experienced at the black dot. Image a represents an image that is purely phase encoded, image b shows an image that is frequency encoded from left to right and phase encoded in the other direction. Image c shows an image that is frequency encoded on a radial grid. The arrows indicate the spatial mismapping of the signals after image reconstruction.

over the volume to excite a slice. The frequency based selection of the slice cause field inhomogeneities and chemical shifts to result in through-plane image distortion and displacements. For example, the fat in the intended slice is not excited, while fat in a slice below the intended encoded slice is.

To encode signal in 3D, at least three different sampling schemes can be used, which include: phase encoding in all imaging three directions, phase encoding for two directions and frequency encoding for the third imaging dimension and frequency encoding for all imaging dimensions. Figure 1.3 illustrates the implications for each of the three basic methods of encoding for two locations that experience different frequency offsets.

Figure 1.3a shows an image that is purely phase encoded. In such an experiment the phase encoding gradient, as illustrated in 1D in Figure 1.2a, is applied along all three imaging directions. A field or frequency offset in this case will only result in a phase offset:

$$\hat{s}(x,y,z) = s(x,y,z,TE)e^{-i\delta\omega(x,y,z)(TE)} \tag{1.19}$$

As was the case for the 1D phase encoded acquisition, each sampled point in k-space of a phase encoded dataset corresponds to one encoding step. Therefore, in case of a 3D phase encoding experiment, each location requires a separate acquisition. The total acquisition time is therefore given

by $N_x \times N_y \times N_z \times$TR with N_i the number of sample points in direction i and TR the repetition time of the experiment.

The efficiency can be increased by applying frequency encoding along one imaging direction, as illustrated in Figure 1.3b. A frequency offset in the frequency encoding direction not only results in a phase offset, but also in distortion of the reconstructed image:

$$\hat{s}(x,y,z) = s(x-\delta x, y, z, TE)e^{-i\delta\omega(x-\delta x,y,z)TE} \tag{1.20}$$

Equation 1.20 shows that signal at location (x,y,z) in an image originates from a location (x+δx,y,z), with δx given by Equation 1.17. A frequency offset due to, e.g., a chemical shift, would result in a discrete shift of the position. A field gradient in the x-direction would result in image scaling. In other words, contrary to the purely phase encoded signal, the image is distorted along the frequency encoding direction. The image acquisition, however, is shortened to $N_y \times N_z \times$TR.

The third sampling scheme, illustrated in Figure 1.3c, applies frequency encoding along all imaging directions, by filling the Fourier space in a spoke-like fashion. Prior to the reconstruction, the radially acquired samples are usually interpolated to a rectangular grid. However, due to the frequency encoding along each direction, each location itself will act as a point source and its signal intensity will be distributed over a ring (2D) or a spherical shell (3D) with its radius given by δx. An advantage of the 3D radial encoding is that the echo time, which is the time between excitation and encoding, can be reduced. The short echo time allows imaging of structures with a very large transverse relaxation rate, such as bone and other solid structures [25].

The signal dephasing and signal pile-up as described by Equation 1.18 also apply in 3D. Signal dephasing in 3D is given by complex multiplication of the signal dephasing in each direction. The acquisition time is similar to the experiment that uses frequency encoding along one dimension. The duration of a 3D frequency encoding experiment is usually somewhat longer due to the increased number of acquisitions needed to image the outer parts of the frequency domain.

1.4 Outline of the thesis

Herein we are concerned with the analysis and manipulation of the effects of macroscopic field inhomogeneities in MR imaging. As shown in the previous sections, field inhomogeneities result in a signal phase and invoke image

distortions. In the first part of the thesis (chapter2-5) the image phase is studied, while the second part of the thesis (chapters 6-8) relates to image distortions.

In the first part of the thesis the phase images are shown to serve as an effective means to generate and manipulate image contrast. In chapter 2 it is shown that the phase derivative can be used to provide positive contrast and allows paramagnetic and diamagnetic field perturbing structures to be discriminated. Phase derivative magnitude images provide positive contrast surrounding field perturbing objects, but are also sensitive to field gradients. In chapter 3, the specificity of the phase derivative is shown to be increased by calculating the Laplacian of the signal phase, since it is zero in regions of constant or linearly varying susceptibility and nonzero at abrupt changes in susceptibility, for instance, at a single point, a ridge, an interface, an edge or a boundary. In chapter 4, the discriminative property of the signal phase is shown to allow detection of micro-calcifications in *ex vivo* breast specimens. In chapter 5, the phase derivative is shown to not only provide contrast, but also to be applicable to reduce signal loss due to signal dephasing induced by macroscopic field inhomogeneities. This macroscopic signal loss induces $R_2^\star$ signal decay, but does not reflect a tissue property. In chapter 5 it is shown that this unwanted effect of a field distortion on the signal can be reduced by dividing the acquired signal by an estimate of the signal dephasing, which is obtained by integrating the phase derivative over a voxel.

The second part of the thesis focuses on image distortions induced by field inhomogeneities. In previous work, image distortions surrounding a field perturbing object, which result of a 3D center-out frequency encoded radial acquisition, were exploited to accurately locate the center of the field perturbing object. This accurate localization is realized with the center-out Radial Sampling in Off-Resonance (co-RASOR) technique, which applies a global frequency offset to center-out radial encoded data. By applying the frequency offset, signal pile-up that surrounds the field perturbing object can be focused onto its geometrical center. The focus of the signal results in high positive contrast at the exact center of such an object. In chapter 6, the required frequency offset is shown to be more efficiently applied during reconstruction than during signal acquisition. Reconstruction co-RASOR is furthermore demonstrated to be more flexible than acquisition co-RASOR and to allow the center of an object to be located automatically. In chapter 7, the acquisition duration of the 3D co-RASOR is addressed. It is shown that - under certain conditions - two 2D co-RASOR acquisitions, instead of one 3D acquisition, allow the acquisition time to be reduced from several minutes

for the 3D acquisition to less than 4 seconds for the dual-plane technique, while maintaining the 3D accuracy. By applying the dual plane co-RASOR acquisition a brachytherapy source could be tracked with 1 mm accuracy with a frame rate of approximately 0.25 Hz. Applications that require a high geometric fidelity are well-known to be hindered by image distortions along the frequency encoding direction(s). In chapter 8, the pros and cons of single point imaging (SPI) as a solution for MR imaging artifacts in the presence of field inhomogeneities are discussed. SPI is attractive in that it applies phase encoding in all three dimensions whereby it becomes insensitive to image distortions induced by field inhomogeneities. In chapter 8 data acquired with SPI is compared to data encoded by applying frequency encoding along one encoding direction. In addition, the potential of SPI data is illustrated by phantom experiments. Furthermore, promising methods to decrease the acquisition duration are outlined.

There are two rules for success:
1) Never tell everything you know

R. H. Lincoln

Part I

Analysis and manipulation of the effects of field inhomogeneities on the signal phase

There is none so blind as
they that won't see

J. Swift

CHAPTER 2

Phase gradient mapping as an aid in the analysis of object induced and system related phase perturbations in MRI

Published as: C.J.G. Bakker, H. de Leeuw, K.L. Vincken, E-J. Vonken, and J. Hendrikse. Phase gradient mapping as an aid in the analysis of object induced and system-related phase perturbations in MRI. *Physics in Medicine and Biology*, 53(18):N349-N358, 2008.

Abstract

In this note we wish to demonstrate the utility of phase gradient mapping (PGM) as an aid in the analysis and characterization of object-induced and system-related macroscopic phase perturbations in MR imaging. To achieve this goal, phase gradient maps and, if applicable, field gradient maps were derived from standard phase images via a forward difference operator that takes phase wraps into account. By means of phantom experiments, PGM was shown to provide reliable phase and field gradient information, even in regions with multiple phase wraps. Furthermore, PGM was shown to enable positive identification of local phase and field perturbing objects and allow for a global discrimination between positive and negative local susceptibility deviations. The suitability of PGM for *in vivo* studies was demonstrated by a 3D brain examination of a healthy volunteer.

2.1 Introduction

Since the early days of MRI, phase mapping has been utilized to study object-induced and system-related disturbances of the MR signal phase. Mapping of the phase has, for instance, been employed to monitor blood flow, to depict blood vessels, and to study pathology-related and drug-induced susceptibility changes in tissues. In addition to diagnostic applications, phase mapping has found application in performance testing and quality assurance and in studies concerned with the analysis, characterization, compensation, and exploitation of artifacts invoked by local deviations (ΔB) of the static magnetic field (B_0). Examples of the latter applications include studies of ΔB-related signal losses in $T_2^\star$-weighted imaging [12, 24, 26–31] and functional MRI [32–37], and studies of ΔB-related systematic errors in diffusion-weighted imaging [38, 39].

With regard to the analysis of macroscopic phase effects, it is readily appreciated from the literature that such an analysis not only requires knowledge of local phase offsets ($\Delta\phi$), but also of local phase gradients ($\nabla\phi$). In chapter 20 of the textbook by Haacke et al. [5], for instance, it is nicely demonstrated how ΔB induced geometric distortions and signal alterations in spin echo and gradient echo acquisitions can conveniently be modelled in terms of the interference between the local field gradients and the imaging gradients. Phase and field gradient mapping may thus be considered natural extensions of conventional phase and field mapping and may be expected to be of benefit when the goal is to analyze, characterize, compensate or exploit local phase and field perturbations.

To date, the seemingly obvious extension of phase mapping to phase gradient mapping seems to have remained largely unexplored. An explanation could be that conventional procedures for estimating gradients, e.g., via a Gaussian kernel in the image domain, produce false contours when directly applied to phase maps containing phase wraps [40]. Differentiation thus seems to require phase unwrapping, a time-consuming pre-processing step that may need user intervention and that is difficult or even impossible when the signal-to-noise ratio is low or when there are phase discontinuities or unconnected regions [41].

In this note we aim to fill up the indicated gap by demonstrating the utility of phase gradient mapping (PGM) for the analysis and characterization of object-induced macroscopic phase perturbations of the MRI signal. To achieve this goal, phase gradient maps and, if applicable, field gradient maps will be derived from the phase images via a forward difference operator that

takes into account phase wraps. By way of phantom experiments, PGM will be shown to provide reliable phase and field gradient information, even in regions with multiple phase wraps. Phase gradient mapping will further be shown to allow positive identification of local phase and field perturbations and global discrimination between positive and negative local susceptibility deviations. The suitability of PGM for *in vivo* studies will be demonstrated by a 3D brain examination of a healthy volunteer.

2.2 Methods

2.2.1 Scan techniques

All imaging was done on a 1.5-T clinical whole body system (Achieva 1.5T, Philips Medical Systems, Best, The Netherlands) with a quadrature head coil for signal reception. Prior to data collection, first-order shimming was applied to the volume of interest. In the phantom experiments, shim settings were first determined for a homogeneous cylinder phantom and maintained during further experimentation.

Three-dimensional images of the phantoms and the volunteer were obtained with a velocity-compensated radiofrequency spoiled gradient echo sequence with a repetition time of 30 ms, an in-phase echo time (TE) of 18.4 ms, and a flip angle of 15°. A coronal orientation of the scan volume was used in the phantom experiments, a sagittal orientation in the volunteer study. Examination parameters further included a field-of-view of 256×256×160 mm^3, a scan matrix of 256×256×80, a readout bandwidth of 435 Hz per pixel with the readout axis oriented along B_0 and one signal average, resulting in a scan duration of 10 min and 30 sec. Prior to reconstruction and postprocessing, raw data was zero filled to a matrix of 256×256×160.

2.2.2 Image processing

Magnitude and phase maps were calculated via M = $|\rho| = \sqrt{R^2 + I^2}$ and P = Arg[ρ] = arctan[I/R], where ρ refers to the acquired complex MR data with real part R, imaginary part I, magnitude M, and phase P. Note that P represents the wrapped phase, i.e., the true phase ϕ wrapped into the interval (-π,π] via the four quadrant arc-tangent operator. To determine the phase gradient $\nabla\phi$, we exploited the fact that the gradient of the true phase must

equal the gradient of the wrapped phase:

$$\vec{\nabla}\phi = \vec{\nabla}P \tag{2.1}$$

This equality is easily verified by using the identity Exp[iP]=Exp[iϕ].

To calculate $\nabla\phi$ via ∇P (Equation 1), partial derivative maps were estimated from the standard phase maps by applying a forward difference operator that corrects for incorrect values of the derivative arising in case of phase wraps. The correction was done by assuming that the phase difference between adjacent points in a phase map has to lie between -π and +π in order to be discernable. The observed phase difference (P_2-P_1), however, will lie between -2π and +2π since both P_1 and P_2 lie between -π and +π. To estimate the true phase difference, therefore, 2π was added to phase differences smaller than -π and 2π was subtracted for phase differences larger than +π. For the x direction, for instance, the resultant phase derivative operator took the form

$$\nabla_x\phi = \nabla_x P \approx \frac{\Delta P}{\Delta x} \tag{2.2}$$

where ΔP denotes corrected forward phase differences in the x direction. Prior to taking derivatives, phase values were set to zero for pixels whose signal intensity in the corresponding magnitude images was below four times the standard deviation of the background noise. Partial derivative and gradient magnitude maps were scaled to radians per mm by taking into account the voxel dimension in each direction. Phase gradient magnitude maps were calculated by taking the square root of the sum of the squares of the vectorial components. In some experiments, including the 3D brain examination, phase gradient maps were converted into field gradient maps using the familiar relation [5]

$$\vec{\nabla}B = -\frac{\nabla\phi}{\gamma \mathrm{TE}} \tag{2.3}$$

where γ represents the gyromagnetic ratio. This expression is valid for a gradient echo acquisition with echo time TE if there are no other sources of spatially dependent phase offsets. Field gradients were expressed in millitesla per meter (mT m^{-1}).

The uncertainty of phase and field derivative maps was estimated from the standard deviation (σ_P) of the noise in the underlying phase images. The σ_P of these phase images was approximated from the corresponding magnitude images via σ_P= σ_M/ (0.655 * M), where M represents the magnitude

of the voxel signal and σ_M the standard deviation of the background noise in the magnitude image [5, p374-376]. The standard deviation of forward phase differences (P_2-P_1) was subsequently calculated as $\sqrt{\sigma_{P_1}^2 + \sigma_{P_2}^2}$. Note that the precision of the phase is determined by the SNR of the magnitude and that a high SNR of the magnitude gives a relatively small error in the phase and phase difference measurements.

All processing was done on a Dell Precision 340 with a Pentium 4 processor using a homebuilt image processing environment. Typical processing times for a 3D data set of 256×256×160 elements were of the order of 5 minutes.

2.2.3 Phantom experiments

To demonstrate the validity of PGM, we used a coaxial cylinder phantom with a known susceptibility difference between the inner cylinder and the surrounding annular region (Figure 2.1c). The phantom consisted of a cylindrical container with a diameter of 10 cm and a height of 10 cm. The container was filled with a 14.7 mM Holmium(III)-doped agarose gel with a volume susceptibility χ of -0.7 ppm (all susceptibility values in SI system), a T_1 of 145 ms, and a T_2 of 85 ms [42]. The container was placed upright on the table top, near the isocentre of the scanner, with its principal axis perpendicular to B_0. After first-order shimming, a coaxial solid glass rod with a length of 12 cm, a diameter of 2 cm, and a volume susceptibility of -11.0 ppm [42] was inserted into the container so as to create a susceptibility transition $\Delta\chi$ of -10.3 ppm between the glass rod and the surrounding gel. When analyzing the data, the phase gradient distribution in the ring-like region outside the rod, in a plane perpendicular to the rod, was assumed to satisfy the expression for an infinite cylinder [3]:

$$\vec{\nabla}\phi = \gamma B_0 \mathrm{TE} \frac{\Delta\chi}{2} R^2 \left(\frac{2x(-x^2+3z^2)}{(x^2+z^2)^3}, 0, \frac{2z(-3x^2+z^2)}{(x^2+z^2)^3} \right), \text{for } x^2+z^2 > R^2 \quad (2.4)$$

with R being the radius of the glass rod, TE the echo time, $\Delta\chi$ the susceptibility difference between the rod and the gel, z the coordinate along B_0, y the coordinate along the cylinder's principal axis, and x the coordinate along the left-right axis. For a rod with a large length-diameter ratio, as employed in our experiments, Equation 2.4 may be expected to give a good approximation of the external phase gradient distribution in planes well away from

both end points of the rod. If this condition is not satisfied, boundary effects may have to be taken into account.

To demonstrate the potential of PGM for highlighting local phase perturbations and discriminating between positive and negative susceptibility deviations, a cylindrical gel phantom with a diameter of 10 cm and a height of 10 cm containing randomly dispersed 3-mm diameter glass spheres and 3-mm diameter aluminium spheres was used. The aluminium spheres consisted of wadded foil with a fractional aluminium volume of 36%. When immersed in the gel, the glass spheres were estimated to represent a negative susceptibility deviation of $\Delta\chi$=-10.3 ppm, the aluminium spheres a positive susceptibility deviation of $\Delta\chi$=+8.2 ppm. Estimations were based on a volume susceptibility of -11.0 ppm for glass [42] and a volume susceptibility of 20.7 ppm for aluminium [2].

2.2.4 Volunteer study

To demonstrate the suitability of PGM for *in vivo* applications, we performed a 3D study of the field gradient distribution in the brain of a 59-year old male volunteer (one of the authors, CJGB).

2.3 Results

2.3.1 Phantom experiments

To validate the PGM algorithm, the cylinder phantom with the solid glass rod was examined with a coronal 3D gradient echo sequence. Well away from the rod, the SNR of the magnitude images was about 22. Figure 2.1 shows the resultant images and phase gradient maps for one of the central slices. The top row shows the acquired real, imaginary, magnitude and phase images, the bottom row the calculated vector components ($\nabla_x\phi, \nabla_y\phi, \nabla_z\phi$) and the magnitude ($|\nabla\phi|$) of the phase gradient. While the original phase map merely indicates the presence of a susceptibility deviation, the $|\nabla\phi|$ map highlights the disturbance and suppresses the background. The $\nabla_x\phi$ and $\nabla_z\phi$ maps (Figures 1e and f) clearly reveal the derivative of the dipolar pattern that is to be expected for a diamagnetic cylinder perpendicular to B_0 (Equation 2.4). The fact that $\nabla_y\phi$ (Figure 2.1g) is at noise level throughout the slice confirms the adequacy of the infinite cylinder model for the central coronal slices of the phantom.

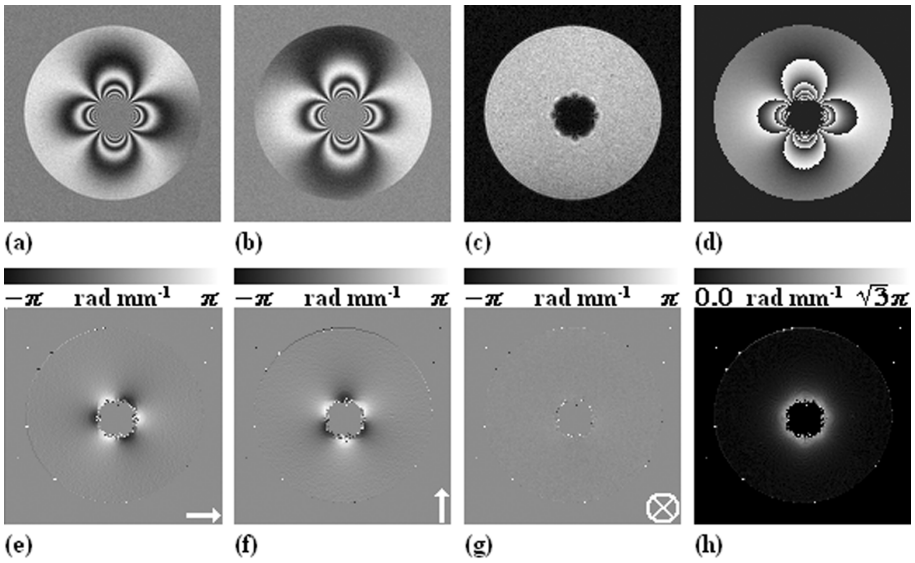

Figure 2.1: Coronal images of a coaxial cylinder phantom with a $\Delta\chi$ of -10.3 ppm between the inner cylinder and the annular region. The top row shows the acquired real (a), imaginary (b), magnitude (c) and phase (d) images, the bottom row the calculated $\nabla_x\phi$ (e), $\nabla_z\phi$ (f), $\nabla_y\phi$ (g), and $|\nabla\phi|$ (h) maps for one of the central slices from a 3D gradient echo examination. Arrows indicate the direction of the positive axis in images 1e and 1f. Phase gradient maps were clipped at the values indicated by the gray scales.

Quantitative analysis of the phase gradient maps displayed in Figure 2.1 revealed an excellent agreement between theory (Equation 2.4) and experiment. This is illustrated by the close correspondence between the predicted and observed profiles for a horizontal profile through the center of the inner cylinder in Figure 2.2. Discrepancies occur near the cylinder wall and are due to a mixture of measurement uncertainty, undersampling, intravoxel dephasing, geometric distortion, and partial voluming (see section 2.4).

To demonstrate the utility of PGM in characterizing local phase disturbances, the homogeneous gel phantom with randomly dispersed glass and aluminium spheres was subjected to a coronal 3D gradient echo acquisition. Overall PGM was found to achieve excellent positive identification of local phase perturbations and to allow discrimination between positive and

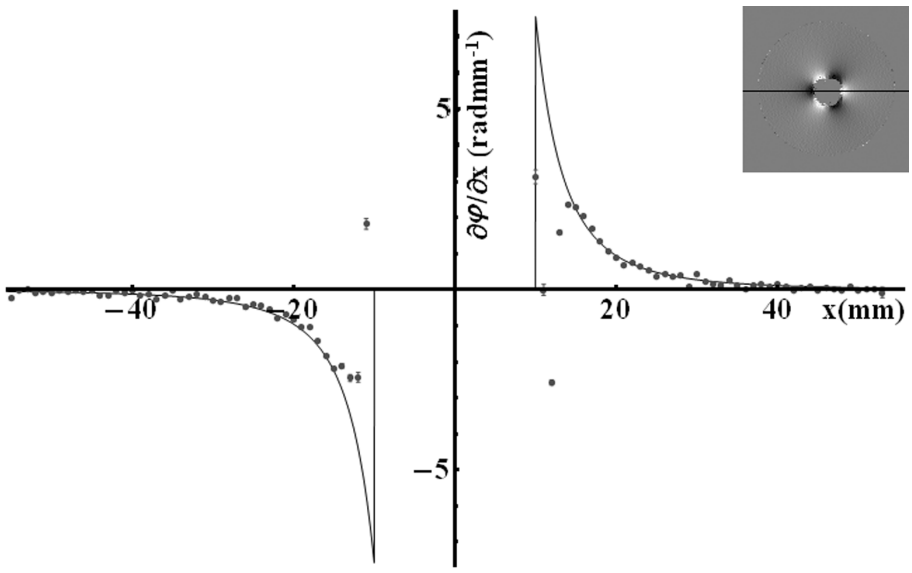

Figure 2.2: Theoretical (line) and observed (dots) profiles of $\nabla_x \phi$ through the centre of the cylinder displayed in Figure 2.1e. The level is indicated by the black line in the insert. Error bars indicate the uncertainty of the experimental data.

negative local susceptibility deviations. Findings are illustrated for a slice containing three glass and two aluminium particles in Figure 2.3. While the original phase and magnitude maps merely indicate the presence of susceptibility deviations, the $|\nabla\phi|$ map (Figure 2.3d) is seen to highlight the disturbances and to suppress the background. The partial derivative maps (only $\nabla_z \phi$ is displayed in Figure 2.3c) clearly indicate whether a phase disturbance relates to a positive (aluminium) or a negative (glass) susceptibility deviation from the background.

2.3.2 Volunteer study

To demonstrate the suitability of phase gradient mapping for human applications, PGM was used to determine the field gradient distribution in the human head. For this purpose, a volunteer was subjected to a whole-brain sagittal 3D gradient echo examination. For brain tissue, the SNR of the re-

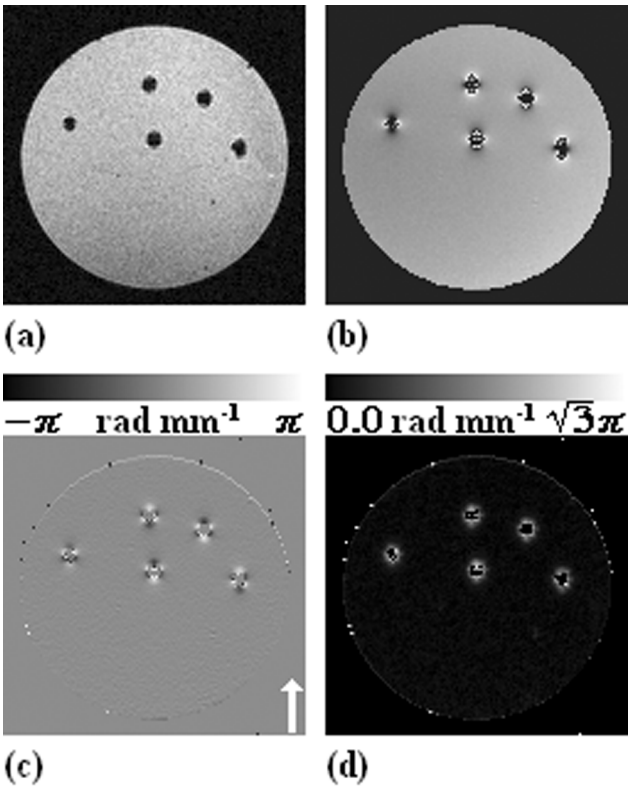

Figure 2.3: Coronal images of a homogeneous gel phantom with randomly dispersed 3 mm diameter glass ($\Delta\chi$ of -10.3 ppm) and aluminium spheres ($\Delta\chi$ of +8.2 ppm). The top row shows the acquired magnitude (a) and phase (b) images, the bottom row the calculated $\nabla_z\phi$ (c) and $|\nabla\phi|$ (d) maps for a slice containing three glass and two aluminium spheres. Phase gradient maps were clipped at the values indicated by the gray scales. The arrow in image c indicates the direction of the positive z axis

sultant magnitude images was about 35. Phase gradient maps were calculated via Equation 2.2 and converted into field gradient maps using Equation 2.3. In accordance with the results for the phantoms, the original phase and magnitude maps were found to indicate the mere presence of field disturbances, whereas the field gradient magnitude maps and the various compo-

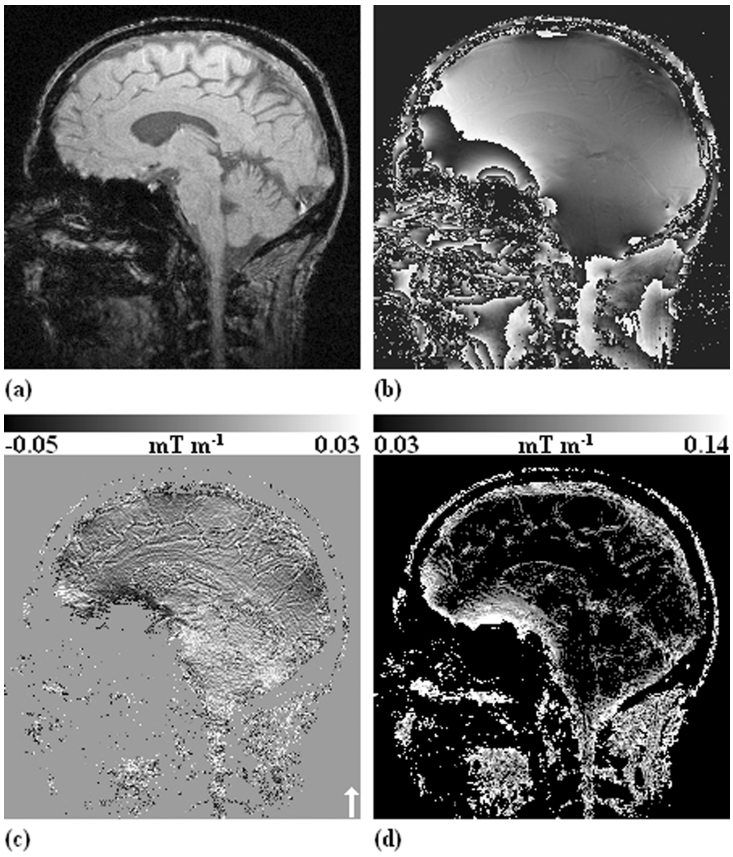

Figure 2.4: Mid-sagittal images of the brain of a volunteer. The top row shows the acquired magnitude (a) and phase (b) images, the bottom row the calculated $\nabla_z B$ (c) and $|\nabla B|$ (d) maps. Field gradient maps were clipped at the values indicated by the gray scales. The arrow in image c indicates the direction of the positive z axis.

nents of the field gradient maps were found to allow a more straightforward characterization and quantification of disturbances. Findings are illustrated for a slice at the level of the nasal cavities in Figure 2.4. The figure shows the acquired magnitude and phase images, the z-component of the field gradient, $\nabla_z B$, and the magnitude of the field gradient, $|\nabla B|$. Near the air

cavities, $\nabla_z B$ clearly shows a pattern characteristic for a positive susceptibility deviation. The magnitude of the field gradient was found to vary between noise level in the background and 0.7 mT m^{-1} near the cavities with an estimated uncertainty of 0.05 mT m^{-1}. The observed maxima are in good agreement with values reported in the literature [24, 29] and of the order of magnitude of the maximum value that is to be anticipated near a spherical air cavity with a radius of about 1.4 cm.

2.4 Discussion

In the previous sections, phase gradient mapping (PGM) was demonstrated to provide reliable phase gradient information, even in regions with strong phase perturbations. PGM was also shown to highlight local phase and field perturbations and to allow discrimination between positive and negative field deviations. The applicability of PGM for *in vivo* studies was demonstrated by a 3D examination of the field gradient distribution in the head of a volunteer. The range of observed field gradients appeared in good agreement with values reported in the literature [24, 29].

The salient features of PGM are simplicity, applicability to image data of any dimension, and avoidance of user intervention. In our view these and the aforementioned features make PGM an attractive alternative to methods that derive information about local gradients from the echo-shifts in k-space [29, 43]. In such methods, the outcome of the procedure is dependent on the shape and width of the user-defined k-space filter.

With regard to the limitations of PGM, it should be appreciated that the quality of phase gradient maps will ultimately be determined by the quality of the input phase images. To obtain valid results, the image data will have to meet certain minimum requirements. First, the contrast to noise ratio of the input phase images should be sufficiently large to produce PGM maps with the desired precision. Since the contrast in phase images is determined by TE, while the noise is inversely proportional to the SNR of the corresponding magnitude images [5, p375], meeting this requirement comes down to an appropriate selection of TE and the parameters that govern the SNR of the experiment. In our experiments, the SNR was 22 in the phantom experiments and 35 in the *in vivo* experiment, but the technique can and has been applied at lower SNR values. Second, images should preferably be acquired with an in-phase echo time so as to avoid phase anomalies in voxels that contain both water and fat protons. Third, images should preferably be ac-

quired with strong imaging gradients, small voxels and short echo times so as to minimize geometric distortion, intravoxel dephasing, and partial volume effects. On the other hand, the SNR should be sufficiently high and the echo time sufficiently long to achieve adequate phase sensitivity [5]. Fourth, the input images - at least the voxels above noise level - should meet the Nyquist criterion, i.e., the true phase jumps between adjacent voxels should be within plus and minus π radians [41]. This criterion may be hard to meet everywhere across the whole field-of-view since, especially, small structures may easily cause very steep gradients. A cylinder perpendicular to B_0 (Equation 2.4), for instance, or a spherical cavity will give a maximum gradient at the wall of $|\nabla\phi|=\gamma B_0 TE\Delta\chi/R$, which goes to infinity for $R\rightarrow 0$. In practice, therefore, the spatial resolution and the echo time may have to be tuned to the geometry and magnetic properties of the structures under investigation to produce useful results. Finally, it should be noted that the forward difference operator that was employed in our study is just one of the operators that can be used for estimating gradients. Another approach could be to start from the definition of the phase, P=arctan[I/R], and to calculate phase gradient maps via the chain rule based gradient operator $\nabla P=(R\nabla I-I\nabla R)/(R^2+I^2)$, where ∇R and ∇I are directly obtained from the raw k-space data by exploitation of the Fourier derivative theorem [40]. This approach avoids the need of phase unwrapping and yields true phase gradient maps in a computationally efficient way. When considering the use of other procedures for estimating gradients, e.g., via a Gaussian kernel in the image domain, it should be realized that such operators may produce false contours when directly applied to phase maps containing phase wraps and may require phase unwrapping as a pre-processing step.

Applications of PGM are to be anticipated in areas where phase effects are pivotal, e.g., field mapping and velocity mapping, and in studies concerned with the analysis, compensation, and exploitation of artifacts invoked by macroscopic field inhomogeneities. Examples of the latter include studies concerned with the compensation of object-induced global field gradients for signal recovery in, e.g., $T_2^\star$-weighted gradient echo imaging [12, 24, 26–31] and functional MRI [32–37], and studies of ΔB-related systematic errors in diffusion-weighted imaging [38, 39]. With regard to potential applications it should further be noted that the magnitude phase gradient images obtained by PGM have much in common with the images that are obtained with so-called positive contrast techniques [3, 43–48]. Unlike some of the latter techniques, PGM does not rely on a specific acquisition method. To what extent PGM can replace or complement such techniques for the selective vi-

sualization of, e.g., paramagnetic structures and magnetically labeled cells, remains to be investigated. Other topics of future research include the use of PGM for studying higher order gradients and the combination of phase gradient and magnitude information as is done in susceptibility weighted imaging [49]. In view of these perspectives and our experience so far, PGM as presented in this paper may be expected to develop into a valuable tool for the analysis and characterization of phase effects in MRI.

Faith is to believe what you do not see; the reward of this faith is to see what you believe

Augustinus

CHAPTER 3

Selective depiction of susceptibility transitions using Laplace-filtered phase maps

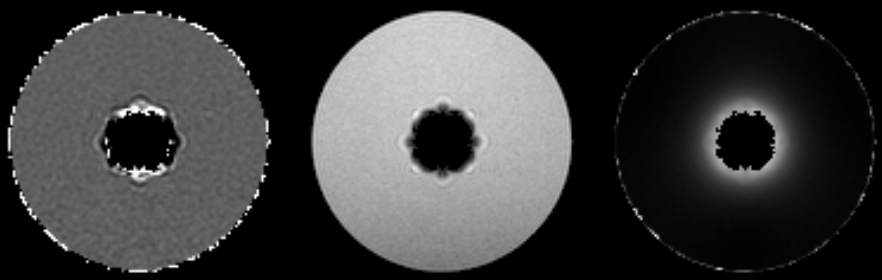

Published as: C.J.G. Bakker, H. de Leeuw, and P.R. Seevinck. Selective depiction of susceptibility transitions using Laplace-filtered phase maps. *Magnetic Resonance Imaging*, 30(5):601-609, 2012

Abstract

In this work, we aim to demonstrate the ability of Laplace-filtered three-dimensional (3D) phase maps to selectively depict susceptibility transitions in an object. To realize this goal, first both the Laplace derivative of the z component of the static magnetic field in an object and the Laplacian of the corresponding phase distribution may be expected to be zero in regions of constant or linearly varying susceptibility and to be non-zero when there is an abrupt change in susceptibility, for instance, at a single point, a ridge, an interface, an edge, or a boundary.

Next, a method is presented to extract the Laplace derivative of a 3D phase map directly from the acquired complex data, so without the need for phase unwrapping or subtraction of a reference image. The validity of this approach, and of the theory behind it, is demonstrated by simulations and phantom experiments with known susceptibility distributions. Finally, the potential of the Laplace derivative analysis is illustrated by simulations with a Shepp-Logan digital brain phantom and experiments with a gel phantom containing positive and negative focal susceptibility deviations.

3.1 Introduction

When placed in the magnetic field of a MR scanner, objects tend to disturb the homogeneity of the preexisting field. Phase mapping is a powerful tool for studying such field disturbances. In the realm of medical imaging, its utility has been demonstrated in studies concerned with field disturbances invoked by, for instance, venous blood, hemorrhagic and calcified lesions, contrast agents, magnetically labeled substances, interventional tools, implants, and internal and external devices.

In spite of its widespread use, the effectiveness of phase mapping for assessing and interpreting field disturbances is often hampered by one or more of the following circumstances: first, phase is not only sensitive to field disturbances but also to other factors, e.g., eddy currents and RF penetration effects [5, 50]; second, phase unwrapping may be required to recover the true phase from its aliased observed values, which is no easy task when the signal-to-noise ratio (SNR) is low or when there are phase discontinuities or unconnected regions [41]; third, phase maps usually reflect a mixture of system-related and object-induced effects which may be hard to disentangle; fourth, and most important in the context of the present study, although phase maps reflect the interaction between the object and the imposed field, they do not allow direct interpretation in terms of the local magnetic properties of the object.

To assist with the interpretation of phase maps, several postprocessing techniques have been developed in the past decade. One approach has been to look at phase gradients rather than at the phase itself [47, 51, 52]. Phase gradient mapping has been shown to circumvent aliasing problems and to act as a kind of positive contrast technique, i.e., to highlight local field disturbances while suppressing background field gradients [53–59]. However, phase gradient mapping did not eliminate the influence of B_0 and B_1 inhomogeneities, external field disturbances, eddy currents, et cetera, and the interpretation of gradient maps was still biased by the nonlocal character of susceptibility-induced phase and field perturbations.

In the work reported here, we aim to show that these issues can be largely resolved by considering the Laplace derivative of the phase rather than the gradient. It will be shown that the Laplace derivative serves as a kind of edge detector in phase maps whose output allows interpretation in terms of some general characteristics of the underlying susceptibility distribution. The idea of using the Laplace derivative for such purposes was inspired by the work of Li and Leigh [60–62] who realized that all of the vector components of the

static magnetic field and the corresponding MR phase distribution are harmonic functions in regions with homogeneous susceptibility and who also recognized that the Laplace derivative in these regions will be largely insensitive to many of the factors that tend to affect the original phase maps, e.g., the inhomogeneity of B_0 and B_1, eddy currents, and spurious phase effects. But other than Li and Leigh, who used the Laplace derivative analysis for improving the precision of MR phase, field and temperature measurements, our goal is to demonstrate that Laplace-filtered phase maps may be used to selectively depict the susceptibility transitions in an object.

To realize this goal, it will first be shown that the Laplacian of the phase in a three-dimensional (3D) gradient echo experiment may be expected to be zero in regions of constant or linearly varying susceptibility and to be nonzero when there is an abrupt change in susceptibility, for instance, at a single point, a ridge, an interface, an edge or a boundary. Next, a method will be presented by which the Laplacian of a phase map can be directly extracted from the complex data, without the need for phase unwrapping or subtraction of a reference image. The validity of this approach and the theory behind it will subsequently be demonstrated by simulations and phantom experiments with exactly known susceptibility distributions. Finally, the potential of Laplace-filtered phase images will be illustrated by simulations with a Shepp-Logan digital brain phantom and by experiments with a gel phantom containing positive and negative focal susceptibility deviations.

3.2 Theory

3.2.1 Magnetic fields in matter

In absence of macroscopic currents, Maxwell's equations for the magnetic field B and the auxiliary field H in matter are given by, respectively:

$$\text{div}\vec{B} = \vec{\nabla} \cdot \vec{B} = 0 \tag{3.1}$$

$$\text{curl}\vec{H} = \vec{\nabla} \times \vec{H} = \vec{0} \tag{3.2}$$

For a linear medium, B and H are related by:

$$\vec{B} = \mu\vec{H} = \mu_0(1+\chi)\vec{H} \tag{3.3}$$

where $\mu = \mu_0(1+\chi)$ represents the permeability of the medium, μ_0 the permeability of vacuum ($\mu_0 = 4\pi \times 10^{-7}$ H/m), and χ the volume susceptibility of

the medium. Equations 3.2-3.3 yield the following relation between B and μ:

$$\vec{\nabla} \times \frac{\vec{B}}{\mu} = \vec{0} \tag{3.4}$$

which can be rewritten into [63, p 21]:

$$\vec{\nabla} \times \frac{\vec{B}}{\mu} = \frac{1}{\mu}\left(\vec{\nabla} \times \vec{B}\right) - \vec{B} \times \vec{\nabla}\frac{1}{\mu} = \frac{1}{\mu}\left(\vec{\nabla} \times \vec{B}\right) + \frac{1}{\mu^2}\vec{B} \times \vec{\nabla}\mu = \vec{0} \tag{3.5}$$

yielding the following expression for the curl of B:

$$\vec{\nabla} \times \vec{B} = -\frac{1}{\mu}\vec{B} \times \vec{\nabla}\mu \tag{3.6}$$

Using the vector identity [63, p 23]

$$\nabla^2\vec{B} \equiv \left(\nabla^2 B_x\right)\hat{x} + \left(\nabla^2 B_y\right)\hat{y} + \left(\nabla^2 B_z\right)\hat{z} = \vec{\nabla}\left(\vec{\nabla} \cdot \vec{B}\right) - \vec{\nabla} \times \left(\vec{\nabla} \times \vec{B}\right) \tag{3.7}$$

where ∇^2 represents the Laplace operator [63, p 23] and using Equations 3.1 and 3.6, we arrive at the following expression for the Laplacian of the vector field B:

$$\nabla^2\vec{B} = \vec{\nabla} \times \left(\frac{1}{\mu}\vec{B} \times \vec{\nabla}\mu\right) \tag{3.8}$$

From Equation 3.8 it immediately follows that $\nabla^2\vec{B} = \vec{0}$ and, hence, $\nabla^2 B_x = \nabla^2 B_y = \nabla^2 B_z = 0$ for regions with constant μ. For regions for which μ is not a constant, the various components and first and second order derivatives of μ and $\vec{B}$ will come into play so as to make $\nabla^2\vec{B} \neq \vec{0}$. Equation 3.8 thus suggests that the Laplacian of B can be employed to selectively depict structures for which μ is not a constant, e.g., interfaces between areas with different susceptibilities.

3.2.2 Phase and field maps in MRI

In MR imaging (MRI), one is usually concerned with susceptibility deviations below 100 ppm. In that case, only a small relative error of order O(χ) will be made by replacing B/μ by B_0/μ_0 in Equation 3.8 [64]. This approximation leads to the following simplified expression for the Laplacian of B:

$$\nabla^2\vec{B} \approx \vec{\nabla} \times \left(\frac{1}{\mu_0}\vec{B_0} \times \mu_0\vec{\nabla}(1+\chi)\right) = \vec{\nabla} \times \left(\vec{B_0} \times \vec{\nabla}\chi\right) \tag{3.9}$$

Applying the vector identity [63, p 23]:

$$\vec{\nabla} \times \left(\vec{A} \times \vec{B}\right) = \left(\vec{B} \cdot \vec{\nabla}\right)\vec{A} - \left(\vec{A} \cdot \vec{\nabla}\right)\vec{B} + \vec{A}\left(\vec{\nabla} \cdot \vec{B}\right) - \vec{B}\left(\vec{\nabla} \cdot \vec{A}\right) \tag{3.10}$$

to Equation 3.9 results in the following expression for the Laplacian of the macroscopic field:

$$\nabla^2 \vec{B} \approx \vec{B_0}\nabla^2\chi - \left(\vec{B_0} \cdot \vec{\nabla}\right)\vec{\nabla}\chi \tag{3.11}$$

Taking the z-components of both sides then yields:

$$\nabla^2 \vec{B} \approx B_0\left(\nabla^2\chi - \frac{\partial^2\chi}{\partial z^2}\right) \tag{3.12}$$

In MRI, the phase of the complex signal in a gradient echo experiment is proportional to the component of the field along B_0 as experienced by the protons. Assuming the main field B_0 of the scanner to be along the z-axis, while ignoring chemical shift effects and phase nonidealities and taking into account the Lorentz correction [5, p 749], the field experienced by the nuclei is given by:

$$B_z^{nuc} = B_z\left(1 - \frac{2}{3}\chi\right) = (B_0 + \delta B_z)\left(1 - \frac{2}{3}\chi\right) \approx B_0\left(1 - \frac{2}{3}\chi\right) + \delta B_z \tag{3.13}$$

with δ B_z=B_z-B_0. Taking the Laplacian of both sides then yields:

$$\nabla^2 B_z^{nuc} \approx -\frac{2}{3}B_0\nabla^2\chi + \nabla^2\delta B_z = -\frac{2}{3}B_0\nabla^2\chi + \nabla^2 B_z \tag{3.14}$$

Combining Equations 3.12 and 3.14 results into:

$$\nabla^2 B_z^{nuc} \approx \left(\frac{1}{3}\nabla^2\chi - \frac{\partial^2\chi}{\partial z^2}\right)B_0 \tag{3.15}$$

Apart from aliasing, the phase of the signal at a certain location is proportional to δB_z^{nuc} and the echo time TE with proportionality constant γ. The Laplacian of the phase is thus given by:

$$\nabla^2\phi = \gamma \mathrm{TE}\nabla^2\delta B_z^{nuc} = \gamma \mathrm{TE}\nabla^2 B_z^{nuc} \approx \gamma \mathrm{TE}B_0\left(\frac{1}{3}\nabla^2\chi - \frac{\partial^2\chi}{\partial z^2}\right) \tag{3.16}$$

From Equation 3.16 it follows that $\nabla^2\phi$ will be zero for regions where μ is constant or varies linearly with position. The Laplacian of the phase may, therefore, be expected to selectively depict the jumps and transitions in the susceptibility distribution of an object.

3.2.3 Laplace analysis of the field of a uniform sphere

For a sphere of radius R and constant susceptibility χ_s surrounded by an infinite medium with susceptibility χ_m, the macroscopic B-fields inside and outside the sphere are given by, respectively [5, p 749]:

$$\vec{B}_{in} = 3B_m \frac{(1+\Delta\chi)}{(3+\Delta\chi)}(0,0,1) \tag{3.17}$$

$$\vec{B}_{out} = B_m \frac{(1+\Delta\chi)}{(3+\Delta\chi)} \frac{R^3}{r^3} \left(\frac{3xz}{r^2}, \frac{3yz}{r^2}, \frac{3z^2-r^2}{r^2} \right) \tag{3.18}$$

where $\Delta\chi = \chi_s - \chi_m$, r^2=x^2+y^2+z^2, and B_m is the field in the medium prior to insertion of the sphere. It is easily verified analytically that all components of the macroscopic B-field satisfy the Laplace equation inside and outside the sphere except at the jump discontinuity at the interface between the inner and outer region. This comes as no surprise, whereas Equation 3.8 reduces to the Laplace equation in regions of constant susceptibility, and it is precisely the Laplace equation that has to be solved to find the B-field for a given susceptibility distribution [64].

Another point that is nicely illustrated by the sphere model is the intrinsic 3D character of the Laplace derivative analysis. From Equations 3.17-3.18, it is easily verified that - in general - it is only the sum of the three second derivatives and not the individual second derivatives or the sum of two second derivatives that will be nulled in a region with constant susceptibility.

3.3 Materials and methods

3.3.1 Simulation techniques

Complex 3D image data was created for user-defined susceptibility distributions, including spheres, cubes, cylinders and combinations thereof, and a 3D Shepp-Logan digital brain phantom [65]. Susceptibility values of the ellipsoids in the Shepp-Logan phantom were taken from reference [66]. The

z-component of the field disturbance invoked by a given susceptibility distribution was calculated by the Fourier method described in [64]. The Lorentz correction was incorporated to obtain the field B_z^{nuc} as experienced by the nuclei [5, p 749]. Objects were specified on a 128×128×128 grid and zero-padded to 256×256×256 to suppress aliasing artifacts in the field calculations [66]. Once a 3D field map was available, all further calculations were done on the initial 128×128×128 grid. True phase maps were derived from the field maps via ϕ=γTEδB_z^{nuc}, where TE denotes the echo time in a gradient echo experiment and γ the gyromagnetic ratio (2.68×10^8 rad/s). Maps of the true phase ϕ were converted to maps of the wrapped phase P using P= Arg[exp[iϕ]]. Subsequently, complex images were simulated via Z=M exp[iϕ], where Z denotes the complex voxel signal and M the signal magnitude. In some simulations, uncorrelated Gaussian noise with zero mean and standard deviation σ was added to the real and imaginary components of Z. Geometric distortion, intravoxel dephasing, chemical shift, and partial volume effects were not incorporated in the simulations.

3.3.2 Scan techniques

All imaging experiments were done on a 1.5T clinical whole body system (Achieva 1.5T, Philips Medical Systems, Best, The Netherlands) with a quadrature head coil for signal reception. In some experiments, shim settings were deliberately spoiled so as to be able to demonstrate the insensitivity of the Laplace derivative of the phase to the inhomogeneity of B_0 and to external perturbations of the field inhomogeneity. Three-dimensional complex image data was acquired with a radiofrequency spoiled multi gradient echo sequence with a repetition time of 20 ms, eight echoes with first echo time (TE_1) 2.3 ms and echo spacing (Δ TE) 2.3 ms, and a flip angle of 15°. Most experiments used a coronal orientation of the scan volume with the readout axis along B_0. Examination parameters further included a field-of-view of 128×128×128 mm^3, a scan matrix of 128×128×128, a reconstruction matrix of 128×128×128, and one signal average, resulting in a scan duration of 5 minutes and 28 seconds. A large readout bandwidth of 435 Hz per pixel was chosen to minimize geometric distortions in the read direction.

3.3.3 Phantoms and preparations

To demonstrate the validity of the Laplace derivative analysis, we used a coaxial cylinder phantom (phantom A) with a diameter of 10 cm and a height

of 10 cm and a known susceptibility difference ($\Delta\chi$=9.4 ppm) between the 2-cm diameter inner cylinder (perspex, χ=-9.05 ppm) and the surrounding annular region (16.6 mM Holmium(III) doped distilled water, χ=+0.36 ppm). The container was placed upright on the table top, near the isocenter of the scanner, with its principal axis perpendicular to B_0. The setup was chosen to satisfy the conditions for an infinite cylinder in and about the midcoronal plane [5, p 755].

To illustrate the potential of the Laplace derivative analysis, we used several phantoms with user-controlled susceptibility deviations. Phantoms included an arrangement of cubic gel phantoms (phantom B) and a cylindrical gel phantom with a diameter of 10 cm and a height of 10 cm containing randomly dispersed 3-mm diameter (diamagnetic) glass spheres and 3-mm diameter (paramagnetic) aluminium spheres (phantom C).

3.3.4 Image processing

Magnitude and phase maps were calculated via $M = |Z| = \sqrt{R^2 + I^2}$ and P = Arg[Z] = arctan[R,I], where $Z = M\ \exp[i\phi]$ refers to the complex MR signal, R to the real part, I to the imaginary part, and ϕ to the phase. P represents the wrapped phase, i.e., the true phase ϕ wrapped into the interval (-π, π] by the four quadrant arc-tangent operator.

To determine the components of the gradient of the phase, $\nabla\phi$, first-order partial derivatives were estimated from the complex data by complex division of adjacent pixel values in each direction:

$$\delta\phi(i) = Arg[Z(i+1)Z^*(i)] = \phi(i+1) - \phi(i) \tag{3.19}$$

In effect, this procedure yields the forward difference of the true phase in each direction, as is easily verified by using the equality Exp[iP]=Exp[iϕ], and bypasses the need of phase unwrapping [52]. To obtain the gradient, differences were converted into discrete derivatives by taking into account the voxel size in each direction. Phase gradient magnitude maps were calculated by taking the square root of the sum of squares of the vectorial components.

To determine the Laplacian of the phase, $\nabla^2\phi$, the constituent second-order partial derivatives were estimated from the complex data by complex division of adjacent pixel values in each direction:

$$\begin{aligned}\delta\phi(i) &= Arg[Z(i+1)Z^*(i)] - Arg[Z(i)Z^*(i-1)] \\ &= \phi(i+1) - 2\phi(i) + \phi(i-1)\end{aligned} \tag{3.20}$$

In effect, this procedure yields the symmetric second difference of the true phase in each direction, and avoids the need of phase unwrapping. The Laplacian of the phase was calculated by adding the constituent second differences divided by the voxel size in each direction. For isotropic voxels of unit size as used in our study, this amounted to evaluation of the following expression [60]:

$$\begin{aligned}\nabla^2\phi(i,j,k) =& \phi(i+1,j,k) + \phi(i-1,j,k) + \phi(i,j+1,k) + \phi(i,j-1,k) + \\ & \phi(i,j,k+1) + \phi(i,j,k-1) - 6\phi(i,j,k)\end{aligned} \tag{3.21}$$

Note that true phase jumps between adjacent pixels have to be within the interval (-π, +π] in order to be uniquely recoverable from the complex data and, hence, to produce valid first- and second-order derivatives. From Equation 3.21 it follows that $\nabla^2\phi$ will be within (-6π, +6π]. For quantitative purposes, phase gradient and Laplace-filtered phase maps were scaled to radians per mm and radians per mm^2, respectively, by taking into account the voxel dimension in each direction.

The uncertainty of phase derivative and Laplace-filtered phase maps was estimated from the standard deviation (σ_P) of the noise in the underlying phase images. The σ_P of these phase images was derived from the corresponding magnitude images via $\sigma_P = \sigma_M$ / (0.655 M), where M represents the magnitude of the voxel signal and σ_M the standard deviation of the background noise in the magnitude image [5, p374-376,p877]. The standard deviation of forward phase differences (Equation 3.19) was subsequently estimated by $\sigma_P\sqrt{1^2+1^2}$=$\sigma_P\sqrt{2}$, and the standard deviation of the Laplace difference (Equation 3.21) by $\sigma_P\sqrt{1^2+1^2+1^2+1^2+1^2+1^2+6^2}$=6.48$\sigma_P$. Note that this estimation ignores any differences in magnitude between the voxels involved in the evaluation of Equation 3.21. Also note that the precision of the phase is proportional to the SNR of the magnitude and that a high SNR of the magnitude gives a relatively small error in the phase and phase difference measurements.

The same general procedure that was used for calculating $\nabla\phi$ and $\nabla^2\phi$, was also employed for calculating the gradient and Laplacian of the static field B_z^{nuc} (Equation 3.15) and the corresponding true and wrapped phases (Equation 3.16) in the simulations (section 3.3.1).

All processing was done on a Dell Precision 340 with a Pentium 4 processor using a homebuilt image processing environment. Typical processing times for a 3D data set of 128×128×128 elements were on the order of a few seconds.

3.4 Results

3.4.1 Simulations

Simulations were done to substantiate the analysis presented in the theory section (Equation 3.16) and to verify the procedure that was developed to determine the Laplace derivative of the phase directly from the complex data (Equation 3.20). Using simple objects with known susceptibility distributions, several theoretical observations could easily be verified including (a) the validity of Equation 3.16, relating the Laplacian of the phase to the susceptibility distribution, (b) the requirement that phase jumps between adjacent voxels be within (-π, π] in order to produce valid numerical results for $\nabla^2\phi$, and (c) the validity of the noise propagation model described in section 3.3.4. A typical simulation result is shown in Figure 3.1. The object is a cube

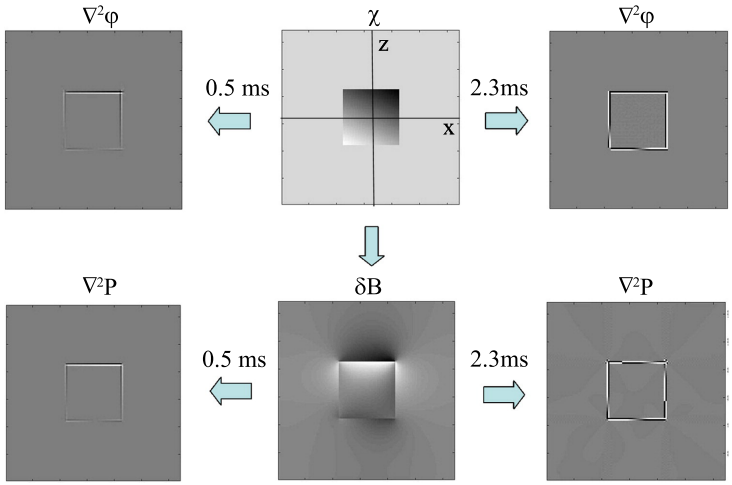

Figure 3.1: Simulated field perturbation (δB), Laplacian of the true phase ($\nabla^2\phi$), and Laplacian of the wrapped phase (∇^2P) for a horizontal plane through the center of a cube with linearly varying susceptibility χ_i = -9(1+x/40+z/20) ppm. The cube is surrounded by a medium with χ_e=0 ppm. B_0 is 1.5T, echo times are 0.5 ms (left) and 2.3 ms (right), respectively.

with edge 40 and internal susceptibility χ_i=-9(1+x/20+z/40) ppm embedded in a signal-bearing medium with χ_e=0 ppm. In agreement with Equation

3.16, the Laplacian of the phase is zero everywhere, despite the presence of linear susceptibility gradients along x and z. Nonzero values only occur at the interfaces between the cube and the medium. For a simple geometry as presented in Figure 3.1, the output of the Laplacian at the interfaces can be easily predicted with Equation 3.21. The predicted values appear to be in perfect agreement with the observed values in Figure 3.1. Aliasing is observed whenever the phase jump between adjacent voxels is larger than plus π or less than minus π, as occurs along the right and upper faces of the cube, and can be distinguished from the situation where the susceptibility difference between the inner and outer compartment vanishes, as happens to be the case for x=-20, z=-10 on the left face and for x=0, z=-20 on the lower face of the cube.

3.4.2 Phantom validation

Experimental validation of the Laplace derivative analysis, as summarized by Equation 3.16 and 3.21, was performed with the coaxial cylinder phantom (phantom A) and the set of cubic elements (phantom B). The phantoms were examined with a coronal 3D gradient echo acquisition. The top row of Figure 3.2 shows the acquired magnitude and phase images and the calculated Laplacian of the phase for one of the central slices through phantom A. The second row shows the first derivative of the phase in each direction, the third row the second derivatives. As expected, the Laplacian is zero everywhere except at interfaces, which is clearly not the case for the first and second derivatives. The derivative maps nicely reveal the nonlocal character of the phase gradient invoked by the susceptibility difference between the inner and outer compartment and provide an illustration of the fact that a phase gradient at a certain location does not imply a susceptibility gradient at the same location. Figure 3.2 also provides an illustration of the fact that zero output in regions with constant susceptibility is a property of the Laplacian and not of the component second derivatives, a fact that was mathematically proven for a uniform sphere in section 3.2.3.

The immunity of the Laplacian of the phase to external field disturbances and bad shimming conditions is demonstrated by Figure 3.3. The figure shows the acquired magnitude and phase images and the calculated gradient magnitude and Laplace derivative of the phase for one of the central slices through phantom B. Both the phase map and the gradient map nicely reflect the interference between the fields of the cubes and reveal the presence of a field disturbing element on the far left. The Laplacian is zero in

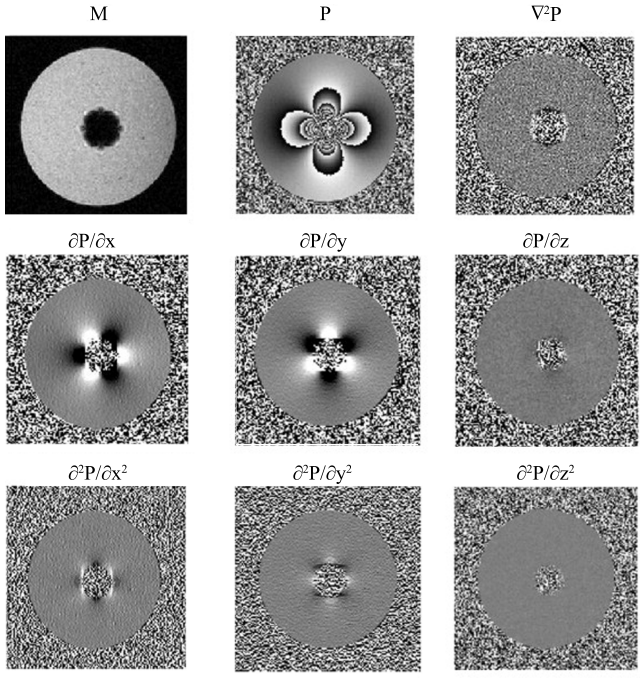

Figure 3.2: Experimental magnitude (M), phase (P), first order phase derivative (∂P/∂x, ∂P/∂y, ∂P/∂z), second order phase derivative (∂^2P/∂x^2, ∂^2P/∂y^2, ∂^2P/∂z^2), and Laplacian phase derivative (∇^2P) maps for a horizontal plane through the center of a coaxial cylinder with its long axis perpendicular to B_0. The χ of the inner compartment is -9.05 ppm, the χ of the outer compartment +0.36 ppm, B_0 is 1.5 T and TE is 2.3 ms.

both cubes, illustrating the fact that the MR phase distribution is a harmonic function in regions with homogeneous magnetic susceptibility and no macroscopic currents [60].

Another aspect of the Laplace derivative analysis that could be checked with phantoms A and B was the propagation of noise from the source images to the Laplacian of the phase. For the outer compartment in phantom A, for instance, the standard deviation σ_P of the phase was 0.99, as estimated from the corresponding magnitudes via $\sigma_P = \sigma_M / (0.655\ M)$. The standard deviation σ_L of the Laplacian of the phase was estimated from the Laplace

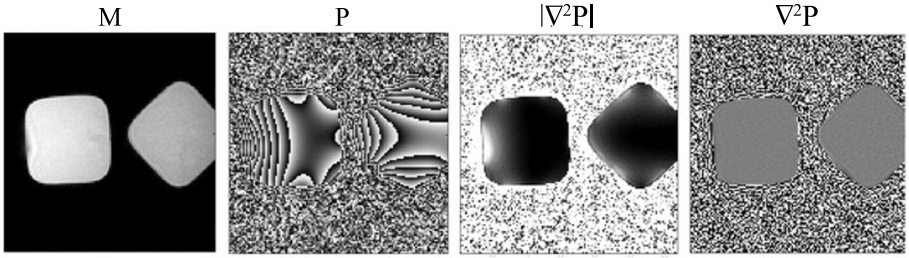

Figure 3.3: Experimental magnitude (M), phase (P), phase gradient magnitude ($|\nabla P|^2$), and Laplacian phase derivative ($\nabla^2 P$) maps for a horizontal plane through the center of two homogeneous cubic gel phantoms with χ= -9.05 ppm, B_0 is 1.5 T and TE is 18.4 ms.

images directly and was 6.47 for the outer compartment. This is in excellent agreement with the relation $\sigma_L \approx 6.48\sigma_P$ predicted for a region of uniform signal magnitude (section 3.3.4).

3.4.3 Illustrative examples

Further simulations and experiments were done to illustrate the ability of Laplace-filtered phase images for selectively depicting interfaces between areas with different susceptibilities and, in the special case of focal susceptibility deviations, for discriminating between positive and negative susceptibility deviations. The former aspect is illustrated by Figure 3.4 which shows some results of simulations with the Shepp-Logan digital brain phantom. The figure shows the field and phase maps for two transversal slices through the phantom. The Laplacian selectively depicts the interfaces between regions with different susceptibility and yields zero output for regions with constant susceptibility, even when the field and phase maps seem to hint at susceptibility variations (bottom row).

The potential to discriminate between positive and negative susceptibility deviations and to generate positive contrast images is illustrated by the results of experiments with a gel phantom with randomly dispersed glass and aluminium spheres (phantom C). Figure 3.5 shows the results for a slice containing three aluminium and two glass particles. Although the original phase and magnitude maps merely suggest the presence of susceptibility deviations, the Laplace-filtered phase map is seen to selectively depict the deviations and to null the background. The Laplacian also seems to allow

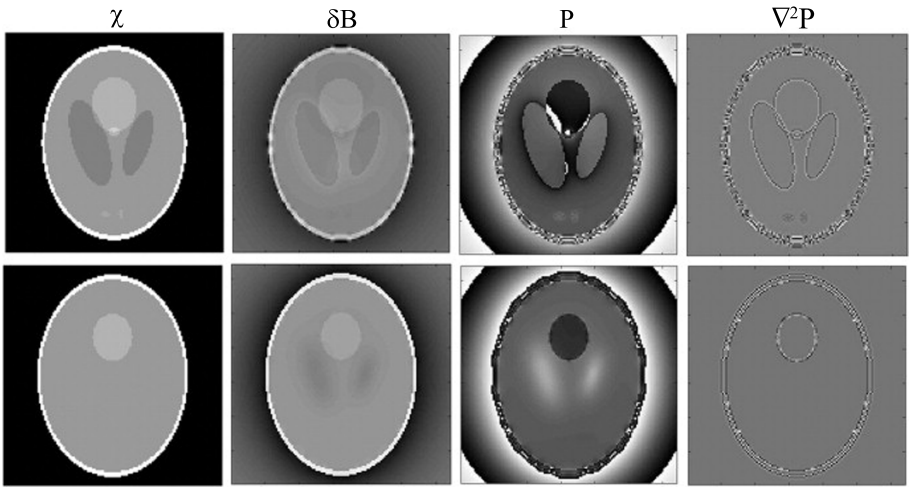

Figure 3.4: Simulated field perturbation (δB), wrapped phase (P), and Laplacian of the wrapped phase ($\nabla^2 P$) for two coronal planes (slice 49 top and slice 65 bottom) through a 3D Shepp-Logan numeric phantom with a user-specified susceptibility distribution in a static field B_0 of 1.5T at an echo time of 10 ms.

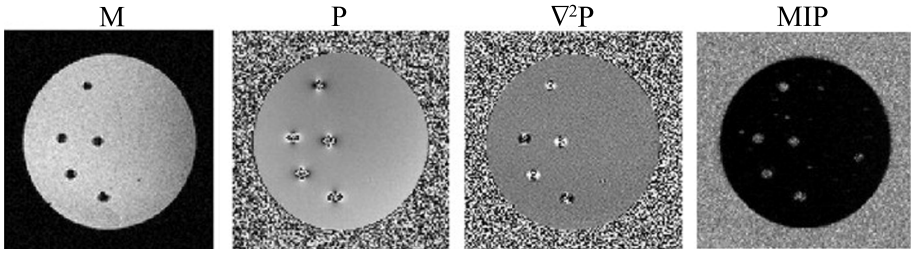

Figure 3.5: Experimental magnitude (M) and phase (P) map and calculated Laplace-filtered phase map ($\nabla^2 P$) for a coronal slice through a cylindrical gel phantom with positive and negative susceptibility deviations. The chosen slice reveals three positive and two negative deviations. Additional deviations show up in the maximum intensity projection (right panel).

discrimination between positive (aluminium) and negative (glass) susceptibility deviations from the background on the basis of the patterns that are predicted by Equation 3.16. Numeric evaluation of Equation 3.16 shows that a single voxel with susceptibility deviation $\Delta\chi$ will produce a pattern (χ/3, 0, χ/3) in the Laplacian of the phase along x and y and a pattern (-2χ/3, 0, -2χ/3) along z. A positive contrast image of the susceptibility deviations (right panel in Figure 3.5) was obtained by making a maximum intensity projection of the magnitude of the Laplace derivative images.

3.5 Discussion

In the previous sections, Laplace-filtered phase images were shown to enable selective depiction of the susceptibility transitions in an object with negligible bias from factors that normally influence phase maps, such as the inhomogeneity of the applied B_0 field. A method was presented by which the Laplace derivative of the phase could be directly obtained from the 3D complex data, without the need of phase unwrapping or subtraction of a reference dataset. The validity of this approach and of the theory behind the Laplace derivative analysis was demonstrated by simulations and phantom experiments with exactly known susceptibility distributions. The capabilities of the Laplace derivative analysis were illustrated by simulations with a Shepp-Logan phantom and experiments with a gel phantom.

Effectively, the Laplace derivative analysis as presented in this manuscript provides a kind of segmentation tool for 3D phase images, where segmentation is based on the susceptibility characteristics of the object. Interpretation in terms of the susceptibility distribution is only allowed, however, if the analysis is applied to 3D data, as was theoretically shown for a spherical susceptibility deviation in section 3.2.3. In this respect, there is a difference with the Laplace operator that is commonly used for segmentation and edge detection purposes in digital picture processing [67, p184]. This operator is usually applied to 2D greyscale images and does not produce results that can easily be interpreted in terms of a physical property. As to the interpretation of the Laplacian of the phase, it should be realized that phase maps in MRI only represent the z-component of magnetic field. With all components available, the Laplacian would have provided a kind of magnetic source map representing the flux density of the magnetic field gradients. But as it is, Equation 3.16 constitutes the point of departure for interpreting results which are only valid if phase jumps between adjacent voxels are wi-

thin plus and minus π radians. In practice, the spatial resolution and the echo time may have to be tuned to the geometry and magnetic properties of the structures of interest to satisfy this criterion. In addition, it should be noted that the procedure for calculating the Laplacian, i.e., via a convolution kernel in the image domain (Equation 3.20), inevitably degrades spatial resolution.

As regards the limitations of the study, it should be emphasized that complicating factors like geometric distortion, intravoxel dephasing, chemical shift, signal voids, and partial volume effects have been largely ignored. Obviously, such effects may cause false positives if experimental conditions are not chosen properly. In general, images should be acquired with strong imaging gradients, small voxels and short in-phase echo times to keep such effects under control. On the other hand, the SNR should be sufficiently high and the echo time sufficiently long to achieve adequate phase sensitivity.

Applications of the Laplace derivative analysis are to be anticipated in the realm of positive contrast techniques, where accurate depiction and localization of small magnetic perturbers are desired. Here, the Laplace analysis may provide a useful addition to the current repertoire as it applies to phase maps rather than the usual magnitude images [68]. Applications are also to be anticipated in areas where susceptibility effects are pivotal, e.g., MR venography, MR-guided needle placement, MR-guided internal radiation therapy, and MR-guided drug delivery. These applications come in addition to applications that have already been reported in the literature and that relate to the harmonic analysis of phase images for improving the precision of MR phase, field and temperature measurements [60–62].

In view of these perspectives and of our experience so far, Laplace derivative analysis as presented in this paper may be expected to develop into a valuable postprocessing tool for the analysis and interpretation of phase and field effects in MRI.

All space is relative. There is no such thing as size

D.H. Keller

CHAPTER 4

Detecting breast micro-calcifications with 7T MRI

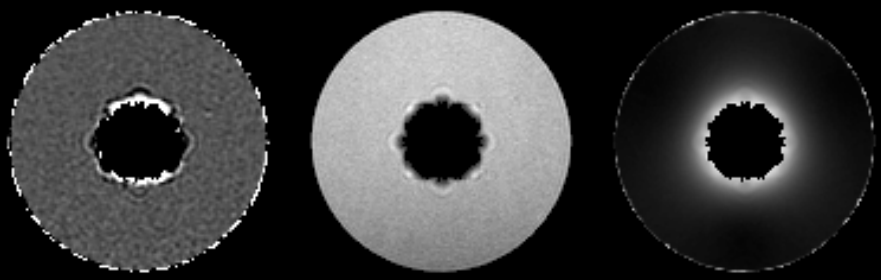

Submitted as: H. de Leeuw, B.L. Stehouwer, C.J.G. Bakker, D.W.J. Klomp, P.J. van Diest, P.R. Luijten, P.R. Seevinck, M.A.A.J. van den Bosch, M.A. Viergever, and W.B. Veldhuis. Detecting breast micro-calcifications with 7T MRI

Abstract

In this work we aim to detect micro-calcifications in *ex vivo* breast tissue using 7 Tesla magnetic resonance imaging (MRI). To achieve the detection, four mastectomy specimens after surgery were obtained with approval of the institutional review board. The specimens were subjected to gradient echo MRI acquisitions on a 7T MR scanner, at a 0.6 mm isotropic resolution. The gradient echo images were used to calculate phase derivative images, which have been found to be susceptible to local susceptibility deviations, such as induced by micro-calcifications. Subsequently, automatic detection of the micro-calcifications based on template matching was tested. To validate the presence of micro-calcifications, mammography images obtained prior to surgery and CT images of the specimen were used.

Phase derivative images displayed characteristic patterns surrounding susceptibility deviations, which enabled the discrimination of diamagnetic structures, such as micro-calcifications, and paramagnetic tissue, e.g. blood. The sensitivity of the phase derivative images was shown to be enlarged by increasing the imaging resolution. Similarly, smaller disturbances could be detected at longer echo times. However, the longer echo times also resulted in shading caused by other field disturbing processes, for example water-fat transitions. The automatic detection tool identified micro-calcifications, but resulted in false positives, which were removed by manual inspection. In conclusion, we have demonstrated that micro-calcifications can be detected on 7T MRI data by calculating the phase derivative of gradient echo datasets of whole breast mastectomy specimens.

4.1 Introduction

Ductal carcinoma *in situ* (DCIS) is generally considered to be a precursor to invasive ductal carcinoma [69, 70]. It is therefore treated as such by performing surgery, followed by radiotherapy. Approximately 62-98% of DCIS presents itself with micro-calcification on mammography [13–15]. However, not all micro-calcifications detected on mammography are associated with *in situ* or invasive malignancy; breast micro-calcifications are often associated with early precursor lesions such as columnar cell lesions [71] or benign lesions [72]. A high probability of malignancy exists in case of fine pleomorphic micro-calcifications, and when a linear or linear-branching distribution - suggestive of a ductal lumen filled with *in situ* cancer - is found [13]. Hence, for characterization of micro-calcifications in the breast, the presence as well as the 3D distribution of micro-calcifications is important.

Currently, mammography is the gold standard for micro-calcification detection and assessment. However, mammography suffers from a number of limitations. First, a mammogram is a 2D projection of the breast. Furthermore, the reported sensitivity and specificity fall within a wide range, of 74%-89% and 85%-99%, respectively [73–79]. Solely based on contrast enhancement, MRI has been shown to improve the detection and staging of DCIS [80–84]. Unfortunately, contrast-enhanced MRI cannot always discriminate enhancing DCIS lesions from a variety of benign causes of signal enhancement. The concurrent MRI detection of micro-calcifications with enhancing breast lesions may improve specificity and may even aid in discriminating likely higher-grade from likely lower-grade DCIS lesions. However, the sensitivity of currently widely applied MRI techniques is too low to detect micro-calcifications in the breast [81, 85].

Micro-calcifications are diamagnetic field perturbing structures whose detection with MRI is challenging, since they possess a relatively small difference in susceptibility when compared to fibrograndular tissue [2, 8]. The small difference in susceptibility results in small magnetic field deviations. Hence, the micro-calcifications result in small perturbations of the signal magnitude and signal phase [2]. Moreover, the breast contains other field perturbing tissue - such as blood and fat - that exhibit much larger susceptibility differences, which interfere with the susceptibility based detection of micro-calcifications [2]. However, these problems may be overcome by imaging at ultra high field strength and by applying dedicated advanced image analysis. The effect of a field offset induced by the difference in susceptibility scales with the main magnetic field strength. Hence, the perturbation

of the signal phase induced by micro-calcifications is larger at higher field strengths [2]. Furthermore, stronger main magnetic field strengths allow smaller voxels to be applied due to the inherently higher SNR. The smaller voxels allow smaller differences in susceptibility to be discriminated [24].

The effects on the signal phase induced by the micro-calcifications are not easily interpreted due to, amongst others, phase wraps and B_1 inhomogeneities. Therefore, the signal phase does not easily allow discrimination of paramagnetic and diamagnetic field perturbing objects and suffers a low specificity. In the present paper we have attempted to increase the specificity by using phase derivative mapping. We have attempted to increase the specificity even further, by applying the phase derivative on high resolution 7T MRI data, to detect micro-calcifications in whole breast mastectomy specimens. The purposes of this study were threefold: first, to illustrate the discriminative property of the technique. Second, to investigate the effect of the imaging resolution and echo time on the detection sensitivity. And third, to demonstrate an approach to automatic detection to aid in the micro-calcification detection.

4.2 Materials and Methods

4.2.1 Mastectomy specimens

In total four mastectomy specimens were included in the study, with approval of the institutional review board. As part of the clinical work flow, mammography images had been obtained prior to surgery. After surgery the specimens were imaged on a 7.0T clinical MR system (Achieva, Philips Health Care, Cleveland, OH, USA). Prior to the MRI acquisitions, the specimens were placed into a plastic container filled with fomblin (perfluoro polyether, Solvay Solexis, Italy). Fomblin is a non-signal bearing medium, which allows a more homogeneous B_1 field for the imaging of small irregularly shaped objects. The MRI acquisition consisted of a radiofrequency (RF) spoiled, velocity compensated multi gradient echo sequence (11 echoes). Scan parameters included field of view (FOV) $220 \times 177 \times 60$ mm^3, 0.6 mm isotropic resolution, repetition time (TR) 55 ms, echo time first echo (TE_1) 2ms, echo spacing (δTE) 1.8 ms, nominal flip angle (θ) 20°, number of signal averages (NEX) 1 and read-out bandwidth 951 Hz, resulting in a scan duration of 21 minutes and 16 seconds. The echo times were chosen such that, for the first echo times the water and the fat peaks are approximately in phase [86]. The

multiple echoes allow the contrast in the phase derivative images to be studied as function of the echo time.

To study the effect of the imaging resolution, a similar scan was performed at a lower imaging resolution. Scan parameters included: FOV $220 \times 177 \times 60$ mm^3, 1 mm isotropic resolution, TR 55 ms, TE_1 2 ms, δTE 1.8 ms, θ 20°, NEX 1 and read-out bandwidth 951 Hz, resulting in a scan duration of 3 minutes and 33 seconds.

Two mastectomy specimens were subjected to CT imaging (Brilliance, Philips Healthcare, Best, The Netherlands). Scan parameters for the first specimen were: voltage 120kV, mAs 400, in-plane reconstructed voxel size 0.2 mm, slice spacing 0.3 mm. Scan parameters for the second specimen were voltage 90kV, mAs 140, in-plane reconstructed voxel size 0.2 mm, slice spacing 0.4 mm.

4.2.2 Data processing

Postprocessing was performed using Matlab (R2010a, The MathWorks, Natick, MA). Phase derivative images were calculated by applying the Fourier derivative theorem on the acquired complex images, as described in previous work [23]. By calculating the phase derivative on the complex data, phase unwrapping and user intervention were obviated [23]. The phase derivative was calculated in each direction, with P_x the derivative along the left-right direction, P_y along the through plane direction and P_z along B_0. The phase derivative at the first echo was subtracted from phase derivatives at subsequent echo times to remove B_1-related phase effects [87]. The phase derivative maps were subsequently blurred (Gaussian kernel width 5 voxels, σ 1 voxel), high-pass filtered [49], and window-leveled (-π,π). Furthermore, the background was suppressed at three times the standard deviation of the noise. The CT images and MR images were registered using Elastix [88].

4.2.3 Interpretation of the phase derivative images

From previous work it is known that a spherical field perturbing structure, such as a micro-calcification, results in a characteristic six-lobe pattern in the phase derivative image [52]. The six-lobed pattern is composed of 3 white dots and 3 black dots, which each constitute the corners of a triangle, pointing in opposing directions, as is shown in Figure 4.1. The direction, in which the 'black triangle' and 'white triangle' are pointing, determines

whether the disturbance originates from either a paramagnetic or a diamagnetic perturbing structure. To verify that the obtained patterns allow differentiation between paramagnetic and diamagnetic deviations, two tests were performed. First, the presence of micro-calcifications was validated by CT images of the specimen and mammography images obtained prior to surgery. Second, the pattern displayed paramagnetic perturbing field structures, such as blood or air, was compared to the pattern displayed by a diamagnetic perturbing field structure, such as a micro-calcification.

4.2.4 Automatic detection

To assist in the detection of the micro-calcifications, an algorithm was developed to detect micro-calcifications automatically. The algorithm is based on a template matching by correlation coefficients. The algorithm was implemented in Matlab (R2010a, The MathWorks, Natick, MA). Implementation was as follows: first, a training set was constructed. The training set consisted of 12 patterns that correspond to the micro-calcifications found in one of the mastectomy specimen. Second, the characteristic 6 lobed pattern surrounding each of these calcification was selected and put into a template map. The derivatives P_x and P_z were selected along the coronal plane, P_y was selected along a transversal slice. Third, the phase derivative images at each echo were matched to patterns in the template images. Fourth, locations that showed a correlation coefficient above 0.85, meaning that locations had a correspondence of approximately 85$\%$ with one or more of the examples in the template map, were selected. After the automatic detection was performed, the micro-calcifications obtained by the algorithm were verified by manual inspection of the phase derivative maps surrounding the locations of micro-calcifications indicated by the algorithm.

4.3 Results

4.3.1 Discrimination of paramagnetic and diamagnetic substances

The discriminative property of the phase derivatives is illustrated for two mastectomy specimens in Figures 4.1 and 4.2. The presence of field perturbing structures was determined on CT. Three different field perturbing structures were found on the CT images: a marker (UltraClip, Bard Biopsy Systems, Tempe, AZ, USA), air and a calcification, as indicated in Figure 4.1.

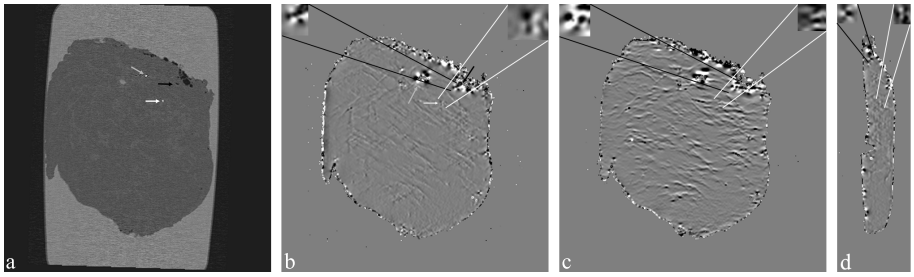

Figure 4.1: CT and MR results of a mastectomy sample. Image a shows the registered CT image, image b-d show P_x, P_z and P_y respectively. The phase derivatives were determined at an echo time of 2ms and are shown along the plane at which the derivative is calculated. The images show a surgical marker (gray arrow), a calcification (white arrow) and air bubbles (black arrow). In images b-d, the inserts show a magnification of the pattern caused by an air bubble (black lines) and the pattern generated by the calcification (white lines). The gray arrow in image b points at a paramagnetic surgical marker.

Registration of the CT image to the MRI image was applied to validate the field perturbers found on the phase derivative images. Figure 4.1 shows that the presence of field perturbing structures is not always evident in all directions of the phase derivative. The calcification could be clearly identified in two images displaying the phase derivative P_x (Figure 4.1b) and P_y (Figure 4.1d). The phase derivative along B_0 (Figure 4.1c) did not show the characteristic pattern for the micro-calcification.

The six-lobed patterns for the micro-calcifications in Figure 4.1b and 4.2b show a white triangle pointing left and a black triangle pointing right. The air bubbles at the edges of the specimen in Figures 4.1b and 4.2b show the opposite pattern, i.e., the white triangle appears to point to the right and the black triangle appears to point to the left. In other words, the air bubbles indicated on CT shows the inverse pattern of the calcification, as expected. Similarly, a surgical marker placed in the breast showed the pattern expected for a paramagnetic disturbance. More closely packed micro-calcifications could also be identified, as illustrated in Figure 4.2. Furthermore, Figure 4.2 shows that overlap of the magnetic field of both micro-calcifications results in a skewed six-lobed pattern for both micro-calcifications.

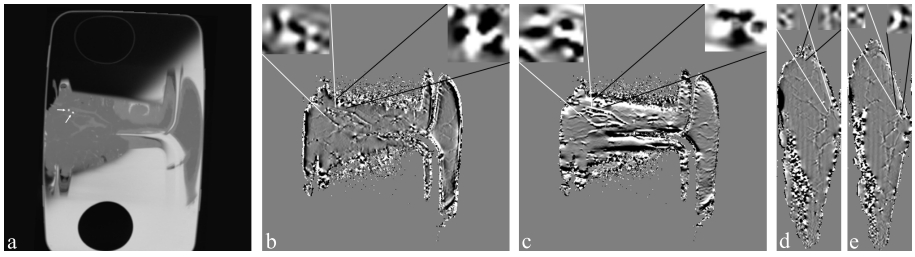

Figure 4.2: CT and MR results of a mastectomy sample. Image a shows the registered CT image, image b-d show P_x, P_z and P_y respectively. The micro-calcifications in image a are indicated by white arrows. The phase derivatives were determined at an echo time of 4.6ms and are shown along the plane at which the derivative is calculated. In the inserts of the images b-d the pattern caused by the air bubble (black lines) and induced by the micro-calcifications (white lines) are shown.

4.3.2 The effects of the spatial resolution and echo time on the phase derivative contrast

The influence of the imaging resolution is shown in Figure 4.3. A calcification is easily visualized at an echo time of 2 ms and using a high spatial resolution (Figure 4.3b). The image displaying a relatively low spatial resolution did not show a perturbation of the magnetic field (Figure 4.3c). However, by increasing the echo time by a factor 2, the decrease of the spatial resolution was compensated and the six-lobed pattern expected for a calcification appeared (Figure 4.3d). Increasing the echo time even further caused the pattern of the water-fat transitions near the glandular tissue to overlap with the pattern of the calcification (Figure 4.3e,f). Since the effect of the water-fat transition is relatively large, the calcification could no longer be discriminated at longer echo times. The influence of the echo time on the contrast in the phase derivative image in a more homogeneous part of the mastectomy specimen is illustrated in Figure 4.4. In this image a micro-calcification is shown for several ascending echo times. At the shortest echo time, the phase derivative at the location of the micro-calcification did not show a perturbation of the magnetic field. However, the six-lobed pattern expected for a diamagnetic disturbance, appeared at longer echo times. At the longest echo time shown (16.4ms), the six lobed pattern could be easily discerned, showing an increase in image contrast for longer echo times.

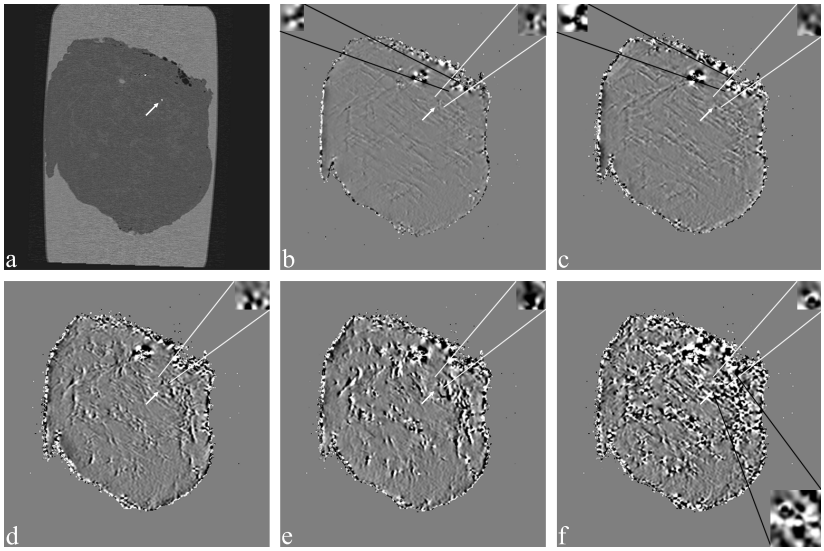

Figure 4.3: CT and MR results of a mastectomy sample. Image a shows the registered CT image, image b shows the phase derivative from left to right at an echo time of 2 ms acquired at 0.6 mm isotropic resolution. Images c-f show the phase derivative acquired at 1 mm isotropic resolution, reconstructed to 0.6 mm isotropic resolution. Images c-f show the same slice at respectively 2 ms, 3.8 ms, 7.4 ms and 11 ms. The inserts show the pattern of an air bubble (black) and the pattern induced by the calcification (white). The insert in the bottom right of image f shows a larger area surrounding the calcification which illustrates the overlap of disturbances seen at longer echo times. The white arrows indicate the location the calcification.

4.3.3 Linear branching calcification

Linear and linear-branching micro-calcifications are of special interest. In Figure 4.5, P_y is shown in the in-plane direction, for five slices spanning 10 mm in total. The six-lobed pattern for a diamagnetic disturbance resulted in a white triangle pointing down and a black triangle pointing upwards. By tracking the pattern along several slices, linear micro-calcifications spreading over 10 mm in length were detected, as illustrated in Figure 4.5. The linear micro-calcification spreading over 10 mm was also reported by the pathologist.

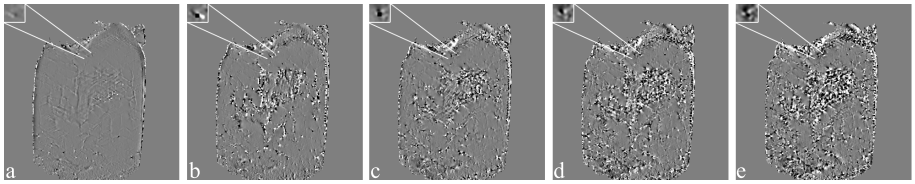

Figure 4.4: MR results of a mastectomy sample. P_x is shown for increasing echo times. The echo times shown are 2 (a), 5.6 (b), 9.2 (c), 12.8 (d) and 16.4 ms (e). The phase derivative is mapped between -π and +π to maintain equal window level for each echo time. The inserts show the pattern caused by a calcification.

4.3.4 Automatic detection

The performance of the algorithm that detected the calcifications automatically was tested on the specimen from which the training set was selected. The algorithm located 35 possible micro-calcifications. After manual inspection, 15 of the 35 possible micro-calcifications were confirmed as true positives. The 15 true positives indicate that three micro-calcifications were found that were originally not included in the training set. Subsequently, the detection algorithm was applied to a second mastectomy specimen, which resulted in 85 possible locations for micro-calcifications. After manual inspection, 17 true positives were confirmed. This data is shown in Figure 4.6. Figure 4.6b shows that the method detects micro-calcifications even in areas with low SNR. The results furthermore illustrate that micro-calcifications are

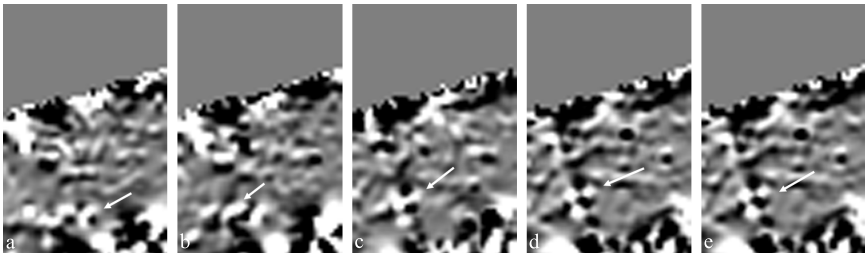

Figure 4.5: MR results of a mastectomy specimen. Shown is the phase derivative in the in-plane direction along five imaged slices spanning in total 10 mm, which contain micro-calcifications. The images are tilted 90° clockwise for display purposes.

dispersed throughout the whole mastectomy specimen. The false negatives were dispersed throughout the whole mastectomy specimen as well.

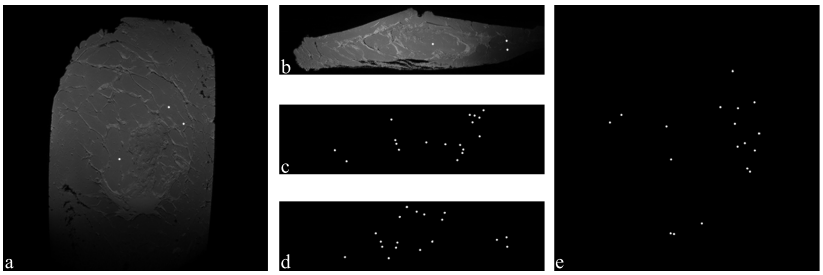

Figure 4.6: Maximum intensity projection over five coronal slices of the magnitude image that contains three micro-calcifications (a, white dots). Image b displays a maximum intensity projection over five sagittal slices that contain three other micro-calcifications (white dots). Images c-e show a maximum intensity projection of the automatic detection map along the transversal, sagittal and coronal plane, showing the three dimensional character of this method.

4.4 Discussion

In this work we present evidence that micro-calcifications can be detected in whole breast specimens using high field 7T MRI. We have demonstrated that by calculating the derivative of the signal phase, paramagnetic susceptibility deviations, such as blood products, and diamagnetic susceptibility deviations, such as micro-calcifications, can be discriminated. The contrast of the phase derivative images is shown to depend on imaging resolution as well as echo time. Longer echo times resulted in increased contrast. However, at longer echo times phase changes caused by small field perturbations, such as a calcification, were obscured by the much larger phase changes induced by stronger field perturbing structures present within the tissue. The results illustrate that micro-calcifications are dispersed throughout the whole mastectomy specimens and that the MR images can provide their distribution in 3D. Furthermore, the phase derivative allowed small spherical structures, as well as linear micro-calcifications that covered over 10 mm in length, to be detected, illustrating the clinical importance of this *ex vivo* study.

Multi-echo data, as exploited in this work, possess an intrinsic limitation. The micro-calcifications perturb the magnetic field only weakly [2, 8]. Therefore, micro-calcifications showed little image contrast. By increasing the echo time, the contrast was increased and thereby smaller calcifications could be imaged. The increase in echo time did not increase the contrast on all locations. Locations at which the image contrast decreased often were located near or at water-fat transitions. The fat consists of multiple resonances e.g. the CH_2 and the CH_3 resonance. At short echo times, the net spin isochromat of the fat can be tuned to be in-phase to the water isochromat. At longer echo times, the water and fat isochromats cannot be tuned to be in-phase and hence the water-fat transitions show up on the signal phase [86]. This effect is clearly illustrated in Figures 4.3 and 4.4. At shorter echo times the phase image is rather homogeneous. Increasing the echo time results in a more heterogeneous phase distribution, especially surrounding the glandular tissue and near water-fat transitions.

The spatial resolution is also a major determinant of the sensitivity of phase derivative mapping. A higher spatial resolution allows smaller perturbations to be detected. Furthermore, a higher resolution is known to reduce in and out of phase effects and signal dephasing [24]. However, a higher resolution results in a longer scan duration. A whole mastectomy specimen could be imaged within 4 minutes when a 1 mm isotropic imaging resolution was used. By decreasing the resolution to 0.6 mm isotropic, the imaging time increased to 21 minutes. The sensitivity, however, also increased by the prolonged scan duration, as is illustrated in Figure 4.3. By applying parallel imaging techniques, for example by using a multi-channel breast coil, the scan duration can be shortened, while obtaining the high image resolution.

The MR imaging sequences were developed to obtain the highest possible image contrast with an acceptable imaging duration. The high resolution images allowed all micro-calcifications detected on the CT image were found on the phase derivative MR images. However, more calcification induced patterns were found on the phase derivative images than on CT. Mammography has an inherent higher sensitivity than CT, but obtaining a mammography of the mastectomy specimens was not feasible. Unfortunately, because of the different shape of the breast *in vivo* and after mastectomy and due to the projection inherent to mammography, 3D registration of MRI to the prior obtained mammogram was not possible. Although most micro-calcifications located by the phase derivative images were not confirmed by a gold standard, we believe it is reasonable to extrapolate the results that were confirmed by CT.

A number of techniques have been presented to allow imaging of micro-calcifications. One of those techniques is susceptibility weighted imaging (SWI) [49, 85, 89]. Detection of micro-calcifications by SWI, has been limited to brain images [89] and phantom acquisitions [85]. SWI imaging uses the image phase to weight the magnitude by the local perturbation of the phase. Window-leveling allows selection of paramagnetic and diamagnetic areas. However, to perform this weighting the phase needs to be unwrapped. Phase unwrapping is difficult, especially in areas with strong field perturbations [90, 91]. Phase unwrapping is furthermore prone to ending up in a local minimum and is difficult in areas with low SNR [90, 91]. Especially at high resolutions, obtained by using surface coils, B_1 receiver inhomogeneities can result in areas of low SNR. These inhomogeneities thereby hamper the SWI because of the inhomogeneities in the signal magnitude. The phase derivative is known to show B_1 inhomogeneities [87]. By subtracting the first echo from the subsequent echoes, the effect of B_1 inhomogeneities was removed and good results were obtained even in areas that suffered from B_1 inhomogeneities (Figure 4.6).

A second method to detect calcification in the breast, based on the signal phase, was presented by Schweser et al. [92]. This method, Quantitative Susceptibility Mapping (QSM), is based on the solution of an ill-defined problem to calculate the local susceptibility from the signal phase. Since the solution to the problem is ill-defined, validation of the obtained results is crucial. Many of the processing steps, however, have not been validated, making the method possibly error prone. Using the image phase itself, as done in this work, is less likely to result in misinterpretations. A third MR based method to detect micro-calcifications uses acoustic radiation force measurements that were applied to a phantom [93]. The acoustic radiation force measurement uses an ultrasound beam to detect changes in the elasticity of the local tissue surrounding the micro-calcifications with MR imaging. The method however requires the presence of an ultrasound source within the MRI scanner, which is not readily available on standard clinical platforms. The technique is furthermore only applicable in homogeneous structures.

There are a number of limitations to the current study. First, the work is limited to *ex vivo* breast specimens. *In vivo* imaging of micro-calcifications is expected to be more difficult. The most important challenges concern motion artifacts and susceptibility artifacts due to, e.g., air in the lungs [94]. Air filling in the lungs creates a large susceptibility induced artifact, which induces heterogeneity in the signal phase. The heterogeneity in the signal phase obscures effects due to local field inhomogeneities, e.g., a calcifica-

tion. The *ex vivo* data was used to ensure that phase derivative mapping can discriminate paramagnetic substances and calcification in the human breast in 3D. To validate that the micro-calcifications were detected at the right locations, CT images were registered to the MR images. The registered CT images confirmed that the phase images displayed the micro-calcifications at the right locations and allowed discrimination of paramagnetic structures, e.g., the clips and air and diamagnetic micro-calcifications. The obtained results can therefore likely be extrapolated to *in vivo* data for which the same image patterns are to be expected.

Second, the algorithm to detect the micro-calcifications showed many false positives, which could be explained by a number of water-fat transitions, e.g., transitions near edges under an angle or blood vessels that form branching structures. By increasing the number of micro-calcifications in the training data set, the threshold at a correlation coefficient of 0.85 can be possibly increased, which can result in less false positives. Moreover, the patterns were matched in 2D only. By including the 3D information of the phase derivative along one direction, the accuracy is also expected to improve. The template matching can furthermore be improved by including information on the pattern in multiple phase derivative directions.

To check the performance of the detection algorithm, it was applied to the dataset from which the examples were extracted. All micro-calcifications in the dataset were located and in addition three true positives were found, showing the potential of the algorithm to detect micro-calcifications. It furthermore shows that the algorithm works correctly, as all of the input micro-calcifications were traced. In the data of another mastectomy specimen 17 true positive micro-calcifications were located along with 68 false positives, emphasizing the need for improvement since the automated detection algorithm is essential for clinical implementation of MRI micro-calcification detection. Furthermore, imaging protocols that are insensitive to motion are needed to be able to extrapolate the results to *in vivo* data. Development of these protocols will include reducing breathing artifacts, reducing B_1 inhomogeneities, while ensuring that sufficient SNR is obtained to enable the signal phase to be studied [94].

In conclusion, we have demonstrated that micro-calcifications can be detected in of whole breast mastectomy specimens by applying phase derivative mapping on 7T MRI data.

To want to understand is an attempt to recapture something we have lost

P. Høeg

CHAPTER 5

Correction of gradient echo images for first and second order macroscopic signal dephasing using phase derivative mapping

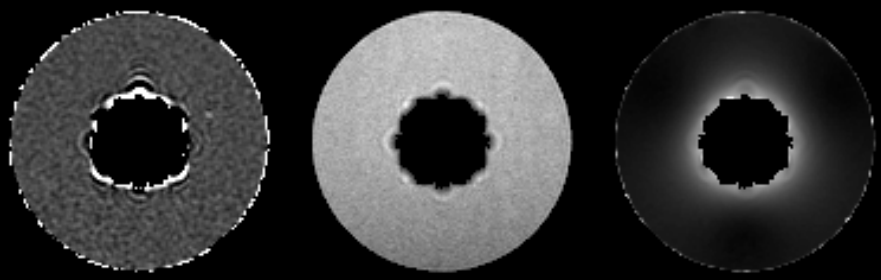

Published as: H. de Leeuw and C.J.G. Bakker. Correction of gradient echo images for first and second order macroscopic signal dephasing using phase derivative mapping. *NeuroImage*, 60(1):818-829, 2012.

Abstract

Gradient echo techniques are often hampered by signal dephasing due to macroscopic phase perturbations because of system imperfections, such as shimming imperfections, or object induced perturbations of the magnetic field as, for example, caused by hemorrhagic lesions, calcified tissue and air-tissue interfaces. Many techniques have been proposed to reduce the effects of the macroscopic phase variations. Among these techniques are tuned pulse sequences, fitting techniques and reconstruction algorithms. These methods, however, suffer from one or more of the following drawbacks: they require longer acquisition times, compensate only locally, require additional acquisitions, can only be applied to multi gradient echo data or may result in inaccurate results.

Herein a generally applicable postprocessing technique is presented to evaluate and compensate signal changes caused by first and second order macroscopic phase incoherences. The technique applies the derivatives of the signal phase, which are determined by applying the Fourier derivative theorem on the complex data. As a result, phase derivatives are obtained without phase unwrapping and without compromising the resolution. The method is validated for single and multi-echo acquisitions by experiments on a co-axial cylinder phantom with known macroscopic field disturbances. The potential of the method for *in vivo* studies is demonstrated with a 3D multi gradient echo brain examination of a healthy volunteer. In general, first order correction is shown to provide the most significant improvements, however a higher order correction is found to be advantageous near sharp transitions of the magnetic field.

5.1 Introduction

Gradient echo MR imaging is routinely used for many purposes, for example, for assessing treatment response [95–97], for imaging and tracking of devices during MR-guided interventions [4, 68, 98], and for depiction of disease, e.g., in Parkinson's disease, cancer, and stroke [30, 49, 99–104]. The choice for gradient echo sequences for such applications is usually motivated by advantages in terms of imaging speed, power deposition, and sensitivity to mesoscopic field inhomogeneities ($R_2^\star$). These advantages result from the absence of a 180° refocusing pulse as is employed in spin echo acquisitions.

The absence of a 180° refocusing pulse can result in desired and in undesired effects. Discrimination between desired and undesirable signal dephasing effects is situation dependent and usually performed by a radiologist or researcher. As regards the undesired effects, the gradient echo signal is degraded by macroscopic phase perturbations. Macroscopic field inhomogeneities, which are characterized by changes of the magnetic field over distances larger than the voxel size [11, 19], include system imperfections, e.g. incorrect shimming, object induced magnetic field disturbances (hemorrhagic lesions, calcified tissue) and field inhomogeneities at extremities of the body (e.g. at the back of the head) [20]. More extreme examples of macroscopic field inhomogeneities are typically observed near air tissue interfaces e.g. near the lungs or at the nasal cavity. With regard to the desired effects, the available contrast (R_2') can be applied to study mesoscopic field inhomogeneities. Mesoscopic field inhomogeneities are variations of the magnetic field on the order smaller than the voxelsize, but larger than the diffusion length. These inhomogeneities are usually caused by susceptibility differences within tissue, for example due to micro-calcifications, by the deoxygenation of blood, due to microbleeds and near $T_2^\star$-contrast agents. Despite the difference in order at which they affect the signal, the effects of mesoscopic field inhomogeneities and macroscopic field inhomogeneities cannot easily be discriminated. Because macroscopic field distortions are generally proportional to the field-strength and considering the tendency to employ increasingly strong main magnetic field strengths for MR imaging, undesirable macroscopic phase effects constitute an increasingly large problem.

During the last two decades many techniques have been proposed to reduce the effects of macroscopic magnetic field inhomogeneities. Among these techniques are tuned pulse sequences, fitting techniques and reconstruction algorithms. Tuned signal acquisition techniques are usually desi-

gned to overcome (a part of) the undesired effects of the macroscopic field inhomogeneities on the signal. Examples are the utilization of extra local gradients [3, 105, 106], adaption of the excitation pulse [11, 48] and tuning of the encoding gradients [107–109]. These techniques usually require precise tuning for effective compensation, lengthen acquisition times, and compensate in a limited number of directions or compensate locally, while introducing signal dephasing in other areas. Fitting techniques on the other hand do not try to compensate, but fit the signal with a model that includes the macroscopic signal dephasing [11, 12, 22, 96]. The fitting techniques can therefore be applied to multi gradient echo data only. Since these methods can only be applied to multi-echo data, they are unsuitable for a number of applications that use the $R_2^\star$ contrast but acquire only one or two gradient echoes [49, 103, 104]. Furthermore, since these fitting algorithms introduce additional fitting parameters on a limited number of data points, the procedure may end up in a local minimum or result in inaccurate results [11, 12]. The third approach consists of reconstruction algorithms which reduce the effects of macroscopic phase perturbations by applying a field and a ($R_2^\star$-) relaxation map during delayed (iterative) reconstruction. Although these reconstruction techniques can be applied to single-echo data, they require additional acquisitions to determine the field-map and relaxation map. Especially field mapping is difficult and increases the acquisition time. Furthermore, the reconstruction methods lengthen the reconstruction time significantly because of the number of reconstructions required during the iterative process of reconstruction [19, 110–112].

In this work a generally applicable postprocessing technique is presented to evaluate and compensate signal alterations invoked by first and second order macroscopic phase incoherences. In this technique, the derivatives of the signal phase are determined by applying the Fourier derivative theorem on the complex data. As a result, the phase derivatives are obtained without phase unwrapping and without compromising the resolution. The method is validated for single and multi-echo acquisitions by experiments on a co-axial cylinder phantom with known macroscopic field disturbances. Furthermore, experiments on gels containing Holmium loaded microspheres are carried out to demonstrate that the technique corrects for macroscopic signal dephasing effects, while leaving the mesoscopic signal dephasing unaffected. The potential of the method is demonstrated on a multi gradient echo acquisition of the head of a human volunteer.

5.2 Theory

5.2.1 The phase derivative

The phase of a complex (MR) signal is defined as:

$$P = \arg[s] = \arctan\left[\frac{I}{R}\right] \tag{5.1}$$

with R, I the real and imaginary signal, respectively. The $\arctan$ function is the four quadrant arctangent function, whose values are restricted to the $(-\pi, \pi]$-interval. Through the arctangent-operation any value of the true phase outside the $(-\pi, \pi]$-interval is wrapped into this interval, creating a black and white stripe (wrapping) pattern around local field distortions. To obtain the true field or field derivatives, which are proportional to the signal phase, unwrapping therefore needs to be performed. Unwrapping, however, is difficult, may end up in a local minimum and should therefore be avoided as much as possible [90, 91, 110, 112, 113]. When taking the derivative of the phase, however, the periodicity of the phase is removed [40]. Along one direction of the image (x) this can be shown for the first and second order phase derivative:

$$\frac{\partial\phi}{\partial x} = \frac{\partial}{\partial x}\left\{\arctan\left[\frac{I}{R}\right]\right\} = \frac{1}{R^2+I^2}\left(R\frac{\partial I}{\partial x} - I\frac{\partial R}{\partial x}\right) \tag{5.2}$$

$$\begin{aligned}\frac{\partial^2\phi}{\partial x^2} &= \frac{\partial^2}{\partial x^2}\left\{\arctan\left[\frac{I}{R}\right]\right\} \\ &= \frac{(R^2+I^2)\left(R\frac{\partial^2 I}{\partial x^2} - I\frac{\partial^2 R}{\partial x^2}\right)}{(R^2+I^2)^2} - \frac{2\left(R\frac{\partial I}{\partial x} - I\frac{\partial R}{\partial x}\right)\left(R\frac{\partial R}{\partial x} + I\frac{\partial I}{\partial x}\right)}{(R^2+I^2)^2}\end{aligned} \tag{5.3}$$

Since $\frac{\partial R}{\partial x} = Re\{\frac{\partial s}{\partial x}\}$, $\frac{\partial I}{\partial x} = Im\{\frac{\partial s}{\partial x}\}$, $\frac{\partial^2 R}{\partial x^2} = Re\{\frac{\partial^2 s}{\partial x^2}\}$ and $\frac{\partial^2 I}{\partial x^2} = Im\{\frac{\partial^2 s}{\partial x^2}\}$, the phase derivatives can be calculated via the derivatives of the complex signal. To determine these derivatives, the Fourier derivative theorem can be used [40, 114]:

$$\frac{\partial^n s[\vec{x}]}{\partial x^n} = F^{-1}\left\{(2\pi i k_x)^n S\left[\vec{k}\right]\right\} \tag{5.4}$$

where F^{-1} denotes the inverse Fourier transform, n the order of the derivative, $S[k_x]$ the Fourier transform of the function $s[x]$, and k_x the direction in which the derivative is taken. Important in Equation 5.4 is that the resolution is maintained, phase wraps are bypassed and user interference avoided.

5.2.2 Macroscopic signal perturbation

A gradient echo experiment yields a complex signal (s), with signal magnitude M (M=abs[s]) and signal phase P (P=arg[s]) for each voxel. Whenever the phase is varying over an imaging voxel, signal coherence within the voxel is partially lost. The consequences of the loss of signal coherence on the magnitude and phase of the signal of the voxel can be assessed by studying the phase and its spread (derivatives) $\frac{\partial^n \phi[x]}{\partial x^n}$, with n$\geq$ 1 the order of the derivative. Assuming the spin density (ρ) within a voxel to be constant, the phase spread across that voxel can be modeled by a Taylor expansion of the phase at the location of the voxel. For example, along the x-direction:

$$\begin{aligned} s[x_0] &= \int_{x_0-\frac{\Delta x}{2}}^{x_0+\frac{\Delta x}{2}} dx \rho[x_0] \ \exp\Big[i * \phi[x]\Big] \\ &= \int_{x_0-\frac{\Delta x}{2}}^{x_0+\frac{\Delta x}{2}} dx \rho[x_0] \ \exp\Big[i\Big(\phi[x_0] + \frac{\partial \phi[x_0]}{\partial x}(x-x_0) + \frac{1}{2}\frac{\partial^2 \phi[x_0]}{\partial x^2}(x-x_0)^2 \\ &\quad + O\Big(\frac{\partial^3 \phi[x_0]}{\partial x^3}\Big)\Big)\Big] \end{aligned} \tag{5.5}$$

with x_0 the location of the voxel of size Δx, $\rho[x_0]$ the effective spin density and $\phi[x_0]$ the signal phase. The effective spin density ($\rho[x_0]$) includes relaxation effects, coil sensitivities and excitation effects. Because of the uniformity within the voxel, a constant signal magnitude is obtained in absence of macroscopic magnetic field gradients. Equation 5.5 can be used to estimate, and correct for, the effect of first, second and higher order phase perturbations on the magnitude and phase of the (native) voxel signal. As an illustration the analytical expression for the effects of the zeroth, first, and second order Taylor expansion of the phase can be determined:

- Zeroth order expansion A constant phase offset in a voxel results in the expression for the signal as given by Equation 5.6:

$$s[x_0] = \rho[x_0] \ \Delta x \ \exp[i\phi[x_0]] = s_0[x_0] \ \exp[i\phi[x_0]] \tag{5.6}$$

  The acquired signal is thus given by signal magnitude $\rho[x_0]\Delta x$ and signal phase $\phi[x_0]$. Hence, for constant phase offsets, the in-phase signal is altered by a (constant) phase factor. The acquired signal magnitude, however, corresponds to the expected signal magnitude in the voxel.

- First order expansion When the phase varies linearly, a more difficult, but familiar, expression is obtained [21]:

$$s[x_0] = s_0[x_0]\exp[i\phi[x_0]]sinc\left[\frac{\partial\phi[x_0]}{\partial x}\frac{\Delta x}{2}\right] \tag{5.7}$$

  Equation 5.7 shows that the signal magnitude is modulated by a sinc function and the signal phase by the same phase offset as the zeroth order expansion. In other words, for linear phase variations the acquired signal is correct up to a signal magnitude factor, given by a sinc function, and a signal phase factor.

- Second order expansion A more complex, analytical, expression is obtained when quadratic phase variations are present:

$$s[x_0] = s_0[x_0]\exp[i\phi[x_0]]\left(\frac{fcs\left[\frac{b\Delta x-2c}{2}\right]}{b\Delta x}+\frac{fcs\left[\frac{b\Delta x+2c}{2}\right]}{b\Delta x}\right)\exp[-id^2], \tag{5.8}$$

$$with\ c = d\cdot\sqrt{\frac{2}{\pi}} = \frac{\partial\phi[x_0]}{\partial x}\Bigg/\sqrt{\pi\frac{\partial^2\phi[x_0]}{\partial x^2}},\ b = \sqrt{\frac{1}{\pi}\frac{\partial^2\phi[x_0]}{\partial x^2}} \tag{5.9}$$

  with fcs the fresnel integral. Since the fresnel integrals are complex, the signal is also phase adjusted because of the complex nature of these integrals. For the derivation of Equation 5.9, the reader is referred to the appendix. Equation 5.9 shows that, as with the linear phase variations, for up to second order phase variations both the signal magnitude and signal phase are modulated.

So far, the analysis of the effects of macroscopic phase perturbations on the magnitude and phase of the true complex signal has been restricted to one direction in the image ($s_0[x_0]$ instead of $s_0[\vec{x}_0]$). To be able to determine the total perturbation of the signal ($s_0[\vec{x}_0]/s[\vec{x}_0)]$, the analysis can be applied to all imaging dimensions. By evaluating Equation 5.5 along each imaging direction and multiplying these results, the total perturbation of the signal is obtained [12]. The unperturbed signal ($s_0[\vec{x}_0]$) is subsequently obtained by complex division of the acquired complex signal by the (complex) signal perturbation. From hereon the assessment of the signal perturbing effect described by the second order expansion will be denoted as the second order phase perturbation. Similarly, the correction of effects described by the second order expansion will described as the second order correction.

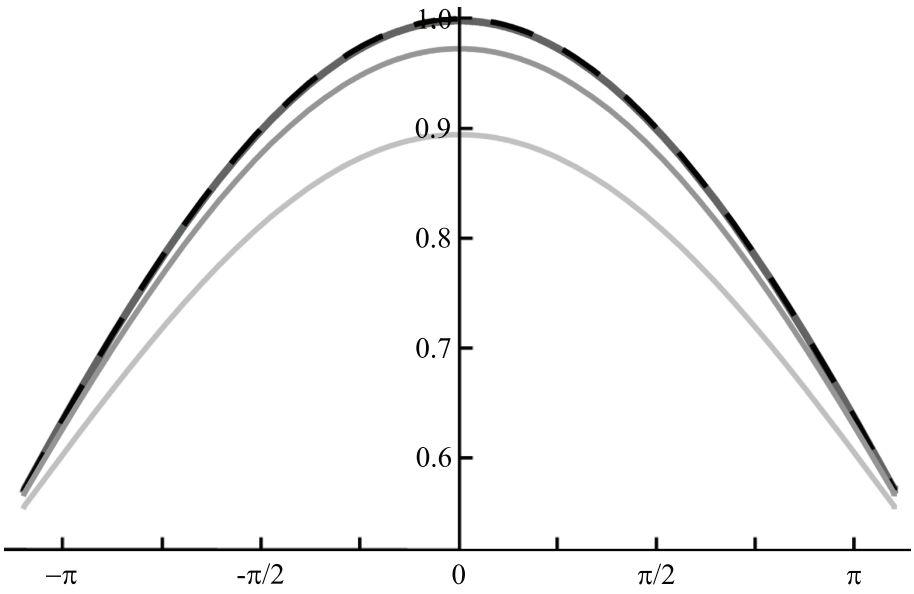

Figure 5.1: Plot of the magnitude of the first order (sinc) perturbation (black, dotted) and the second order (fresnel) perturbation, for three values of the second order gradient; 4π/voxel (b=2, light gray), 2.25π/voxel (b=1.5, gray) and π/voxel(b=1, dark gray), with b as defined in Equation 5.9. Plotted is the magnitude of the perturbations, as a function of the phase derivative within the range of -π to π.

Figure 5.1 shows the magnitude of the sinc dephasing term and the magnitude of the fresnel dephasing term as a function of the value of the first order phase derivative, for three values of the second order phase derivative. Small values of the second order phase derivative result in nearly indistinguishable first and second order perturbations. Larger values of the second order derivative cause the first order perturbation and second order perturbation to deviate. Strong quadratic phase variations cause a reduction of the signal magnitude, even without the presence of a linear phase variation. In Figure 5.1, the first order phase derivative is shown in the $(-\pi, \pi]$ interval. These limits are chosen, since these are imposed by the Nyquist criterion. Usually the Nyquist criterion is formulated in terms of the phase itself (ϕ) [5]. However, when the phase derivatives are calculated, the Nyquist crite-

rion needs to be reformulated in terms of the Taylor expansion of the phase:

$$\left|\phi_0 + \frac{\partial\phi}{\partial x}\Delta x + \frac{1}{2}\frac{\partial^2\phi}{\partial x^2}(\Delta x)^2\right| \leq \pi \tag{5.10}$$

Equation 5.10 shows a number of features. The observed phase itself is limited to the (-π, π]-interval. Since the phase is written in terms of its Taylor expansion also all of the individual terms are limited to (-π, π]-interval. In absence of second order phase derivatives, the observed first order phase derivative in each voxel is thereby restricted to the $(-\pi, \pi]$ interval. Furthermore, without first order phase derivatives, the observed second order phase derivative in each voxel is bounded to the $(-2\pi, 2\pi]$ interval and so on. Obviously, in the presence of multiple or even higher orders of the phase derivatives, such as for a cylinder or a sphere in a medium with differing susceptibility [3], such a simple criterion is not easily formulated. Each of the derivatives is in such a case limited by its contribution in the Taylor expansion to the total observed phase and values of the phase derivatives outside this interval are wrapped into this interval.

5.3 Materials and Methods

5.3.1 Infinite cylinder phantom

Qualitative and quantitative validation of the correction method was done using a coaxial cylinder phantom. The phantom had a known susceptibility difference between the inner cylinder and outer annular region. The phantom consisted of a plastic container with a diameter and height of 10 cm. The container was filled with a 17.4 mM Holmium(III)-doped agarose gel, with a volume susceptibility of 0.3ppm [42]. The container was placed upright near the scanner isocenter with its principal axis perpendicular to B_0.

Measurements were performed with a glass cylinder as the inner cylinder in the center of the gel. The glass cylinder had a length of 12cm, diameter of 2cm and volume susceptibility -11.0ppm, creating a susceptibility difference of 11.3ppm between the glass rod and the surrounding gel. To enable quantitative comparison the true phase derivatives of the cylinder were assumed

to be given by the infinite cylinder model [3]:

$$\phi[x,y,z] = -c\left(\frac{x^2-z^2}{\left(x^2+z^2\right)^2}\right) \tag{5.11}$$

$$\left(\frac{\partial\phi}{\partial x},\frac{\partial\phi}{\partial y},\frac{\partial\phi}{\partial z}\right) = -c\left(\frac{2x(3z^2-x^2)}{(x^2+z^2)^3},0,\frac{2z(z^2-3x^2)}{(x^2+z^2)^3}\right) \tag{5.12}$$

$$\left(\frac{\partial^2\phi}{\partial x^2},\frac{\partial^2\phi}{\partial y^2},\frac{\partial^2\phi}{\partial z^2}\right) = -c\left(\frac{6(x^4+z^4-6x^2z^2)}{(x^2+z^2)^4},0,\frac{6(6z^2x^2-z^4-x^4)}{(x^2+z^2)^4}\right) \tag{5.13}$$

$$\text{with } c = \gamma B_0 \text{ TE } \Delta\chi\frac{R^2}{2}$$

with R the radius of the inner cylinder, B_0 the main magnetic field strength, $\Delta\chi$ the susceptibility difference between the glass cylinder and the gel, TE the echo time, z the coordinate along B_0, y the coordinate along the cylinder principal axis and x the coordinate perpendicular to both y and z.

Imaging was done on a 1.5T clinical whole body MR system (Achieva 1.5T, Philips Medical Systems, Best, The Netherlands). The phantom was subjected to a velocity compensated, radiofrequency (RF) spoiled multi gradient echo sequence (16 echoes). Scan parameters included field of view (FOV) $128 \times 128 \times 128$ mm^3, scan matrix $128 \times 128 \times 128$, repetition time (TR) 100ms, first echo time (TE_1) 2.3ms, echo spacing (δTE) 4.6ms, flip angle (θ) 20°, number of signal averages (NEX) 1 and read-out bandwidth 859 Hz, resulting in a scan duration of 27 minutes and 27 seconds.

5.3.2 Macroscopic versus mesoscopic signal dephasing phantom

To illustrate the applicability of the technique to discriminate macroscopic signal dephasing from mesoscopic signal dephasing and microscopic signal dephasing and to show the potential of the correction for second order dephasing effects, a phantom consisting of two cylinders was used. One cylinder contained a 2% Agar gel containing 30mg/L $MnCl_2 \cdot 4H_2O$ to adapt the T_1 relaxation time. The second cylinder contained the same gel, but in it 4mg/ml of Holmium loaded microspheres were dispersed [95]. The mean diameter of the Holmium loaded microspheres was 30μm and the Holmium content 18.7% by weight, resulting in a volume susceptibility of 880ppm. Because of their paramagnetic properties, the Holmium loaded microspheres result in a mesoscopic effect on the signal magnitude [97].

Both cylinders were placed perpendicular to the main magnetic field to result in a macroscopic field inhomogeneity. When placed in close vicinity of each other, the magnetic field of the plain gel perturbs the magnetic field inside the with Holmium microspheres doped gel and vice versa. Furthermore, the Holmium microsphere create local field inhomogeneities on the mesoscopic scale. Hence, the setup shows macroscopic as well as mesoscopic magnetic field variations, which both vary in amplitude.

Imaging was done on a 1.5T clinical whole body MR system (Achieva 1.5T, Philips Medical Systems, Best, The Netherlands). The phantom was subjected to a velocity compensated, RF spoiled multi gradient echo sequence (16 echoes). Scan parameters included FOV $64 \times 64 \times 64$ mm^3, scan matrix $64 \times 64 \times 32$, TR 39ms, TE$_1$ 2.3ms, δTE 2.3ms, θ 15°, NEX 1 and read-out bandwidth 856 Hz, resulting in a scan duration of 1 minutes and 4 seconds.

5.3.3 Volunteer study

To demonstrate the suitability of the correction algorithms for *in vivo* applications, we performed a 3D multi gradient echo of the brain of a 27-year old female volunteer.

Imaging was done on a 1.5T clinical whole body MR system (Achieva 1.5T, Philips Medical Systems, Best, The Netherlands). A velocity compensated, RF spoiled multi gradient echo (16 echoes) sequence was used. Scan parameters included FOV $256 \times 256 \times 164$ mm^3, scan matrix $128 \times 128 \times 82$, TR 55ms, TE$_1$ 2.6ms, δTE 4.6ms, θ 25°, NEX 1 and read-out bandwidth 1.17 kHz resulting in a scan duration of 9 minutes and 35 seconds.

5.3.4 Postprocessing

Data was processed using in-house developed software written in Matlab (Mathworks, Natick, MA). The first and second order derivative were calculated by applying Equation 5.4 along each direction in the image. To remove spurious influences of noise, the derivatives were smoothed slightly, using a Gaussian kernel with a kernel-size of 5 voxels and a σ of 0.5 voxels.

The values for the derivative were subsequently used to calculate the signal dephasing (Equation 5.7 and Equation 5.9). The maximum values for the phase derivative were set at π/voxel and 2π/voxel for the first and second order derivative, respectively. At locations where the first and second order phase derivative were discarded, i.e. voxels at which values for the phase

derivatives were higher than the defined maxima, e.g., due to noise, no correction was applied.

To calculate the total signal perturbation, the signal perturbations along each direction in the image were multiplied (complex multiplication). After obtaining the total signal perturbation for each voxel, the data was corrected via a complex division of the acquired data by the calculated signal perturbation (complex division). In case of multi-echo acquisitions, individual images were corrected prior to fitting the $R_2^\star$, without using the the phase evolution over time. The $R_2^\star$ was calculated by fitting the linearized exponential signal decay using a least squares algorithm, only using data with a signal magnitude larger than three times the standard deviation of the noise [115]. To compare our method to state of the art methods, the first order correction and the second order correction were incorporated in a non-linear least-square fitting routine using a Levenberg-Marquardt algorithm [12, 22]. Hence, data was fitted to a model that included the first order correction, a model that included the second order correction and a mono-exponential model. The mono-exponential fit was also applied before and after first order and second order correction of the data.

All processing was done on a Dell Precision 340 with a pentium 4 processor using a homebuilt image processing environment. Processing times for the correction model on a 3D dataset of $64 \times 64 \times 32 \times 16$ elements required 5 minutes, fitting of the corrected data using the linearized model 15 seconds. Typical processing times for the first order, second order and uncorrected fitting model using the Levenberg-Marquardt algorithm was 60 min.

5.4 Results

Since the phase derivatives form the basis of the correction algorithm (Equation 5.7, Equation 5.9), the phase derivatives were validated first, using the infinite cylinder phantom. Typical results for the signal magnitude and the signal phase and the first and second order phase derivative (both in the three orthogonal directions), for a coronal slice through the cylinder, are shown in Figure 5.2. The signal magnitude shown in Figure 5.2a displays a ring of reduced signal intensity near the inner cylinder. The signal phase (Figure 5.2e) shows the expected wrapping of the phase. The first (Figure 5.2b-d) and second order (Figure 5.2f-h) phase derivatives show the characteristic patterns for a cylinder perpendicular to the main magnetic field. In-plane (Figure 5.2b,c and f,g), the derivatives show a six and eight lobed pattern for

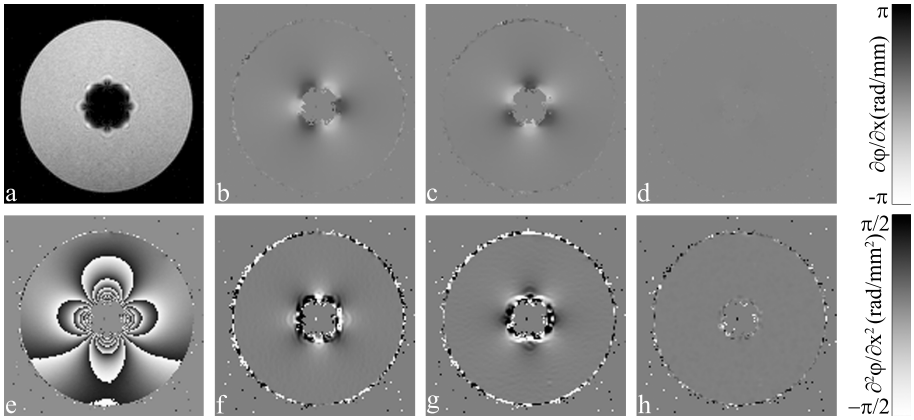

Figure 5.2: Data at 25.3ms: Magnitude (a), phase derivative perpendicular to B_0 in-plane (b), along B_0 (c), perpendicular to B_0 through-plane (d), phase (e) and 2nd order phase derivative perpendicular to B_0 in-plane (f), along B_0 (g) and perpendicular to B_0 in the through-plane direction (h). The first and second order phase derivatives are presented on the scale depicted at the right edge of each row.

the first and second order derivative respectively, while through-plane (Figure 5.2d,h) both derivatives are at noise level. As expected, the amplitude of the first and second order phase derivative decreases with distance to the cylinder center. Since the first and second phase derivative along the principal axis of the cylinder are at noise level (Figure 5.2d,h), the infinite cylinder model appears to be a valid approximation. To demonstrate the accuracy of the acquired phase derivatives, profiles of the acquired phase derivatives and the theoretical phase derivatives for an infinite cylinder are shown in Figure 5.3, for three different echo times. Figure 5.3 demonstrates, for both the first (top panel) and second order phase derivatives (bottom panel), at all echo times a close correspondence between the true phase derivatives and acquired phase derivatives. Far from the cylinder a close correspondence between the theoretical and the acquired first order phase derivatives is observed (top panel), but this correspondence is lost near the cylinder.

Like the phase, the derivatives of the phase scale with the echo time. For example, when tracking the first order phase derivative (top panel) from the left to the right, at one location the profiles instead of increasing in phase derivative, start to decrease. This location is determined by the Nyquist cri-

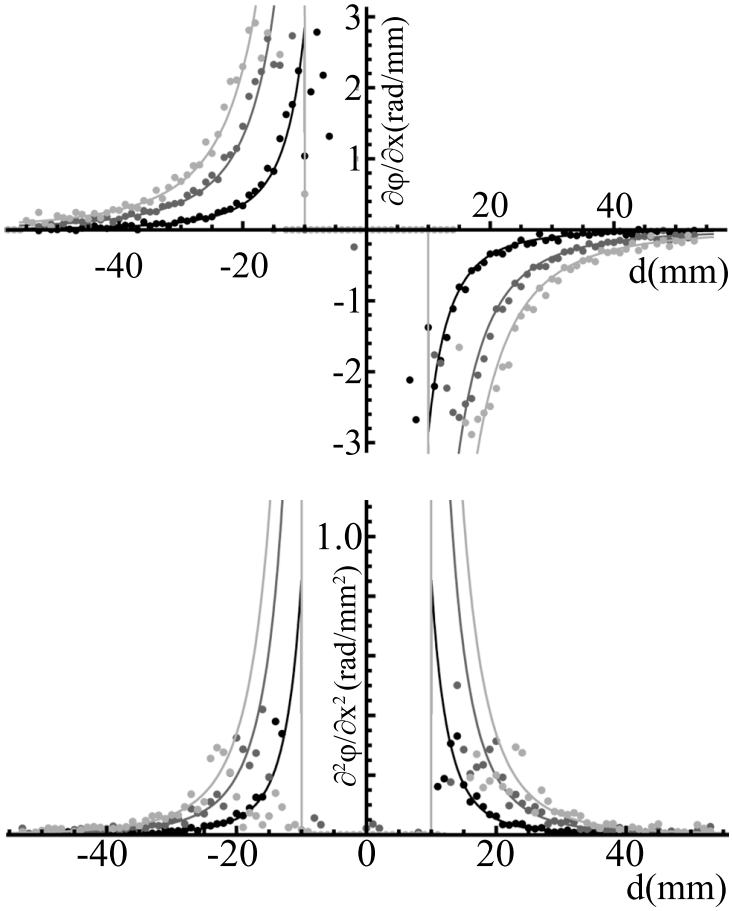

Figure 5.3: Profiles of the first (top) and second order phase derivative (bottom). Profiles of the acquired data (dotted) and of the theoretical value of the phase derivative for an infinite cylinder (lines), at an echo time of 6.9ms (black), 25.3ms (dark gray) and 43.7ms (gray), are shown.

terion (Equation 5.10) and increases in distance from the cylinder center for longer echo times. The location, at which this transition occurs, experiences the same theoretical value of the total phase determined by the sum of the first and second order derivative (Equation 5.11). For the second order derivative (bottom panel) also a close correspondence is observed. The magni-

tude of the second order phase derivative, however, is smaller and the close correspondence is lost at larger distances from the cylinder center compared to the first order derivative. This is again expected from the Nyquist criterion as given by Equation 5.10. Other deviations near or in the inner cylinder, besides the ones imposed by the Nyquist criterion, are due to noise, partial volume effects and geometric distortion. Especially the low SNR in the signal magnitude results in a large spread in the values the phase derivative can show, some of which are within the by Nyquist determined range. The

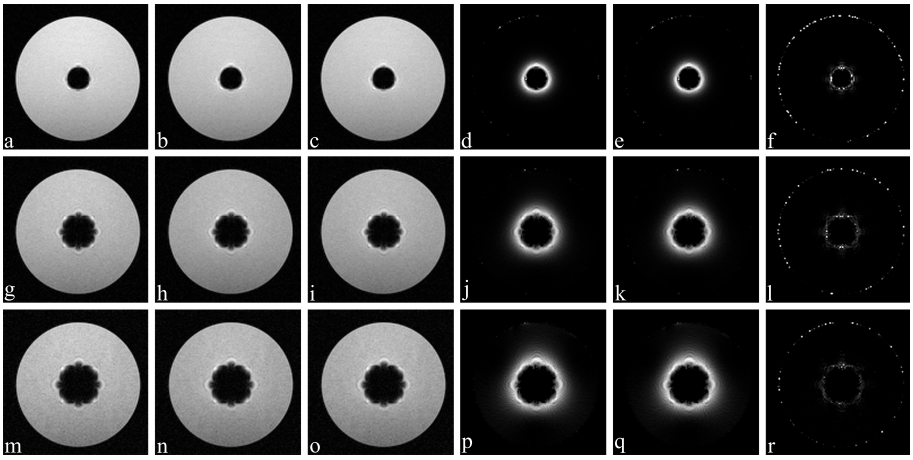

Figure 5.4: Correction of images acquired at an echo time of 6.9ms, 25.3ms and 43.7ms. The top row shows images at 6.9ms (a-f), the middle row at 25.3ms (g-l) and the bottom row images at 43.7ms (m-r). The first column shows the acquired signal magnitude, the second column the first order corrected signal magnitude, the third column the second order corrected signal magnitude images, the fourth column the difference between first order correction and the acquired signal magnitude, the fifth the difference between second order corrected and the acquired signal magnitude, and the sixth column the difference between the second and first order corrected signal magnitude. The magnitude images are displayed with the same scale. The differences between the acquired and corrected images (d,e,j,k,p,q) are windowed between 0 and 10% of the acquired signal intensity maximum, while the difference between the corrected images (f,l,r) is windowed between 0-1% of that same maximum.

effect of the compensation algorithms (first and second order), using these phase derivatives, and images that display the change imposed by the corrections are shown in Figure 5.4 at three echo times. For all echo times, the corrections result in a smaller area of signal dephasing near the inner cylinder. The largest influence of the second order correction is found near the inner cylinder, at those locations the signal dephasing is underestimated by the first order correction (second order correction minus first order correction $>$0). The magnitude of the correction reduces for increasing echo times. The volume which the correction effectively affects is increased. Similarly, the difference between second and first order correction reduces for increasing echo times, but the addition of the second order in the correction affects a larger part of the phantom. Although dephasing is (partially) removed, the correction is hampered by geometric distortion, as can be observed by the spear shape of the correction around the cylinder, which is again more clearly observable at longer echo times.

The effects on the $R_2^\star$ of the correction of the data at each echo time are shown in Figure 5.5. In Figure 5.5g, the distribution of the $R_2^\star$ is shown. Two effects of the corrections on the $R_2^\star$-distribution can be observed. First, the full width half maximum (FWHM) of the distributions increases by applying the corrections, the FWHM is approximately 1.2s^{-1} before correction and 1.3s^{-1} after correction. Second, the average of the $R_2^\star$-distribution shifts towards lower values. The shift of the average of the $R_2^\star$-distribution towards a lower value indicates a reduction of signal dephasing effects in the data. The width of the $R_2^\star$ distribution is, amongst others, caused by shimming imperfections, noise, and diffusion effects. The difference in the values of the $R_2^\star$ between the two corrections is small ($\approx 0.5s^{-1}$ for values in the order of 15 s^{-1} and higher) and mainly present near the cylinder. Since the differences between the two corrections are very small, the differences between the two corrections on the $R_2^\star$ distribution can not be discerned. The corrections, however, reduce the $R_2^\star$ considerably with respect to the uncorrected data. Some effects of signal displacement in the read-out direction can be discerned in the difference maps (spear shape in Figure 5.5d, e).

The differences, between fitting the $R_2^\star$ with a corrected model as done in literature [12, 22] or fit the $R_2^\star$ to corrected data (this work), is shown in Figure 5.6. In Figure 5.6 results for first as well as the second order correction are shown. The fitting algorithms, which include the signal dephasing in the model to which the data is fitted (Figure 5.6, left column), show some artifacts in the $R_2^\star$. The model which includes the second order expansion of the signal phase (Figure 5.6 bottom, left) corrects the data more accurately

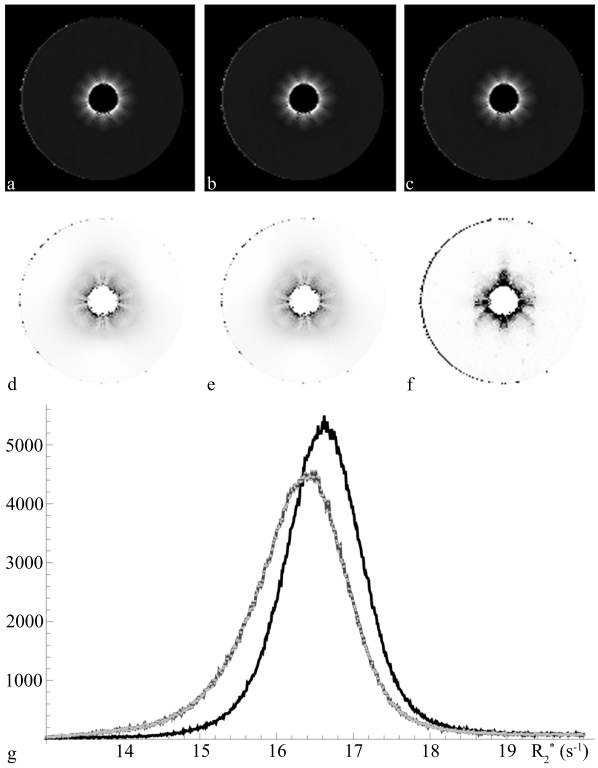

Figure 5.5: $R_2^\star$-image of a single slice of the cylinder phantom before correction (a), after first order correction (b) and after second order correction (c). The second row displays the difference images: first order minus uncorrected (d), second order minus uncorrected (e) and second order correction minus first order correction (f). The R_2 are windowed in the 0-60 s^{-1} interval, the difference between the R_2 before and after correction (d, e) are scaled between -10 and 0 s^{-1}, while image f is scaled between -0.5 and 0 s^{-1}. In image g the histogram of the $R_2^\star$ values of the whole volume of the acquired image (black), of the image after first order correction (gray) and of the second order corrected image (light gray, dotted) are displayed.

than the model that includes the sinc term only (Figure 5.6 middle, left). The results after correction (Figure 5.6, right column) show less artifacts and the $R_2^\star$ is more homogeneous throughout the phantom than the $R_2^\star$ obtained by

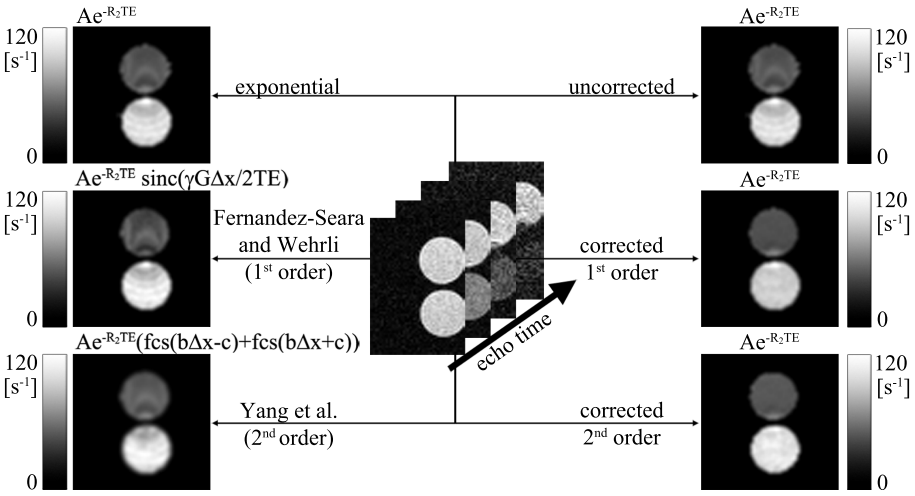

Figure 5.6: Values of the $R_2^\star$ at a sagittal slice of two cylinders placed perpendicular to B_0. The top cylinder is filled with a plain gel, while the bottom cylinder contains a gel containing 4mg/ml of Holmium microspheres as a source of mesoscopic signal dephasing. The data at several echo time points is shown at the center of the figure. The left column shows the results of the fitting procedures with the different signal dephasing models. The right column shows the result of the exponential fitting after correction for signal dephasing. The top row shows the results obtained with the exponential model, the middle row the results with the first order correction and the bottom row the results of the second order correction model. The scale of the $R_2^\star$-values is depicted by the colorbar.

the fitting methods that include the signal dephasing in their fitting model (Figure 5.6, left column). The result of the fitting show that, by applying the corrections, the increased dephasing near the edge of both cylinders is reduced, while the average $R_2^\star$ is nearly unaffected or somewhat reduced. This reduction is to be ascribed to the presence of macroscopic field gradients throughout the whole cylinder. The most prominent change in the $R_2^\star$ for both cylinders can be observed at the edge near the other cylinder. The effect of the second order correction at those locations is larger than the effects of the first order signal correction.

The exact shape of the signal intensity and the $R_2^\star$ of the phantom for the three situations (no correction, first order correction, second order correc-

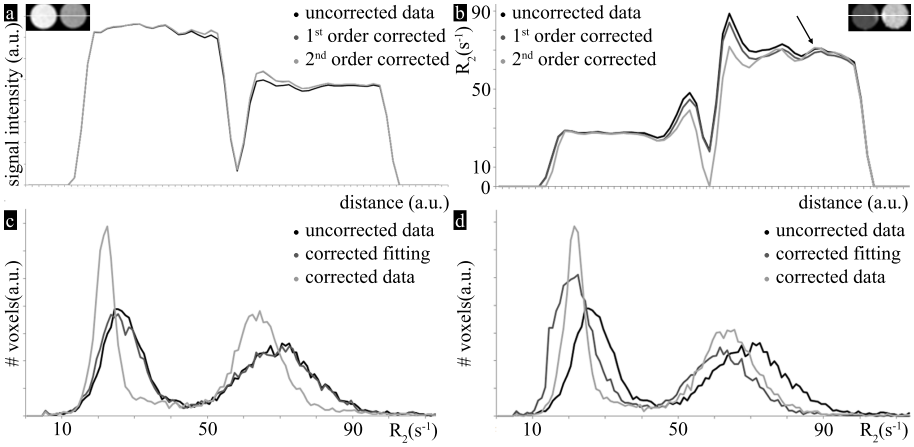

Figure 5.7: Profiles of the signal intensity at TE 11.5ms (a) and the $R_2^\star$ (b) are shown at the top row. The profiles were taken through the center of both cylinders, as illustrated in the insert. The curves show the signal intensity and $R_2^\star$ before correction (black), after correcting the data for first order signal dephasing (gray) and after correcting for second order signal dephasing (light gray). The bottom row shows the histograms of the $R_2^\star$ of the cylinders for the model that incorporates first order signal dephasing (c) and second order signal dephasing (d) respectively. Shown are the histograms before correction (black), after fitting with the extended model (gray) and after fitting of the corrected data (light gray). The arrow in image b indicates the location with an increase of $R_2^\star$ after correction with respect to $R_2^\star$ before correction.

tion) is shown by profiles through both cylinders at their center in Figures 5.7a and b, respectively. The signal intensity is increased by applying the correction. At the edge of the holmium loaded cylinder (lowest signal intensity) some effects of image distortion can be observed, resulting in an intensity higher than the average. The $R_2^\star$ is also shown to be affected by the image distortion. The value of the $R_2^\star$ is changed less by the distortion and the $R_2^\star$ becomes more homogeneous after correction. Unlike the signal intensity, the $R_2^\star$ of the phantom can locally increase as well as decrease after correction of the signal for first or second order signal dephasing. A decrease of the $R_2^\star$ is most commonly observed. The locations at which an increase in the $R_2^\star$ is obtained, show an small increase of the $R_2^\star$ compared to the decreases of the $R_2^\star$ found after correction at other locations. The arrow in Figure 5.7b

indicates a location at which such an increase of the $R_2^\star$ is obtained.

The histograms of the $R_2^\star$ throughout the whole phantom after the different fitting procedures are shown on the bottom row in Figure 5.7. The histograms show that the method which corrects the data and fits the corrected data yields a more coherent $R_2^\star$ throughout the phantom. The $R_2^\star$ after fitting the first and second order corrected data (light gray) shows larger agreement than the $R_2^\star$ fitted including the correction (gray). Furthermore, the corrected data shows a histogram which is reduced in width, showing that the $R_2^\star$ in the phantom is more homogeneous after correction. The method which fits the data with a first order correction term appears to have little effect. Both the fitting models and the correction models show that the second order correction applies a significant improvement on the data.

The applicability of the corrections *in vivo* is shown in Figure 5.8. As already observed in the phantom experiments, the correction of the signal for signal dephasing results in more homogeneous signal throughout the image. Especially near the nasal cavity and the mouth the corrections improve the data, as illustrated at the white arrows. As known from literature, the strongest field gradients and thereby the strongest signal dephasing are located near these structures [12, 22]. Also near the skull base (gray arrow) some corrections are observed due to local field gradients. Some effects of water-fat transitions can also be observed e.g. at the top of the skull.

The influence of the correction algorithm on the $R_2^\star$ *in vivo* is presented in Figure 5.9. The corrections for the signal dephasing affect the $R_2^\star$ throughout the whole brain. Especially the axial images (Figure 5.9 g-l) display the substantial correction applied by the correction near the sinuses. The corrections of the $R_2^\star$ generally are relatively small ($\approx$ -0.2s^{-1}), except near the air tissue interfaces, where corrections of the order of 1-3 s^{-1} are observed. Multiple slices are affected by the correction and hence were affected by signal loss. The correction of 2s^{-1} is of the same order of magnitude as found by others [12]. As with the phantom experiments the changes on the $R_2^\star$ imposed by the second order corrections are minor ($\geq$ 0.2s^{-1}) and are primarily located near interfaces.

5.5 Discussion

Herein a generally applicable postprocessing technique has been presented to evaluate and compensate for signal perturbations invoked by first and second order macroscopic phase incoherence. The derivatives of the signal

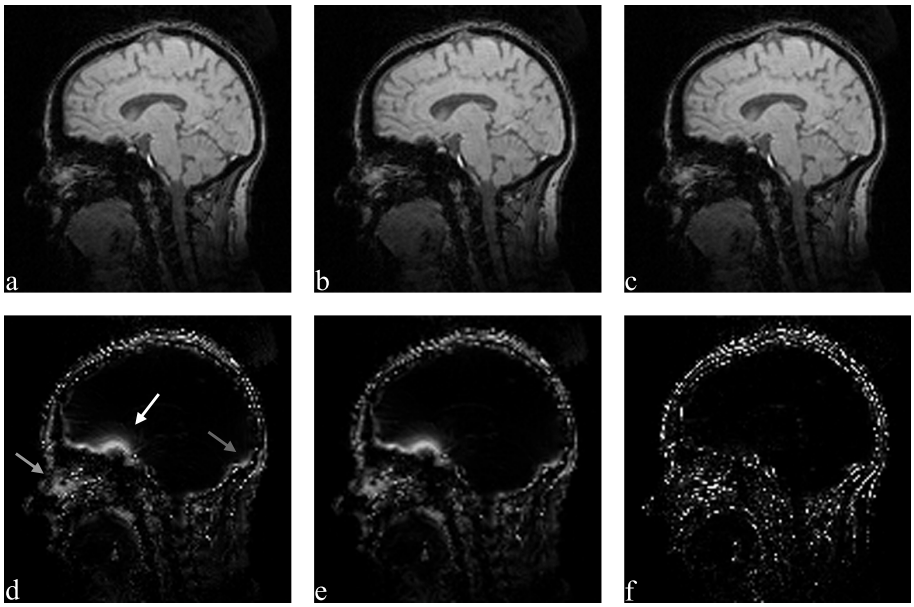

Figure 5.8: Sagittal slices of a human volunteer at an echo time of 21.6 ms. On the top row the signal magnitude after acquisition (a), after first order correction (b) and after second order correction (c) are displayed. The bottom row shows the difference in signal magnitude between first order correction and the acquired data (d), the difference between second order correction and the acquired data (e) and the difference between second and first order correction (f). The threshold of images d,e on the bottom row was placed at 1% of the acquired signal intensity maximum, while the threshold for image f is placed at .01% of the same maximum.

phase are determined by applying the Fourier derivative theorem on the complex data. As a result, the phase derivatives are obtained without phase unwrapping and without compromising the resolution. The correction can be applied on single-echo as well as on multi-echo gradient echo acquisitions. Both the first and second order correction show effects in the signal magnitude and signal phase. Although corrections of the $R_2^\star$ of the order 10 s^{-1} are obtained near sharp transitions of the magnetic field, the additional effect of the correction for the second order variations is relatively small.

The signal phase after correction should ideally be zero, indicating that

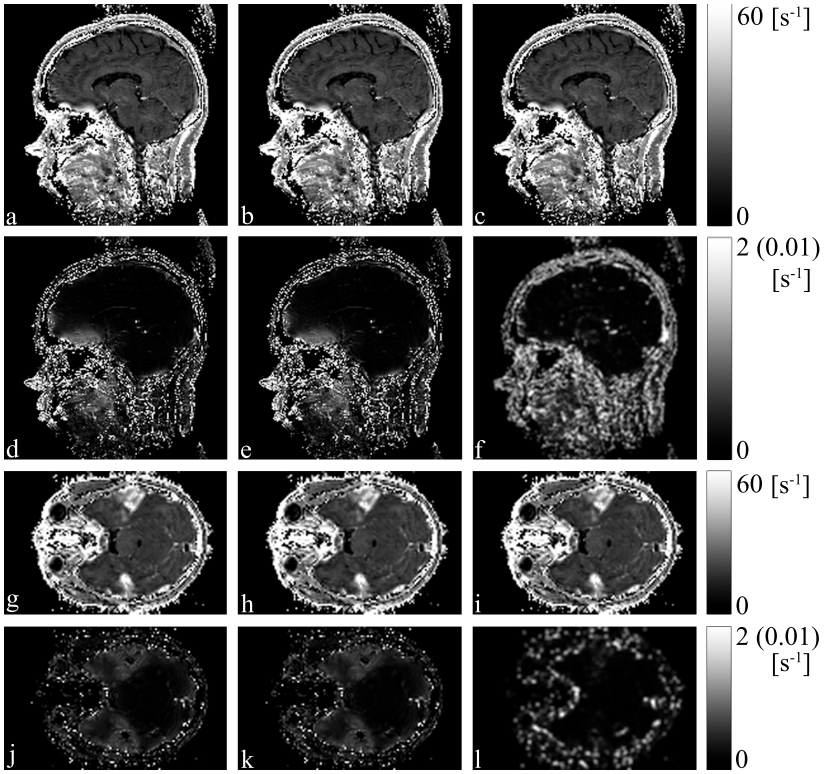

Figure 5.9: Saggital slice (top two rows, a-f) and axial slice near the sinus (bottom two rows, g-l) of a human volunteer displaying the $R_2^\star$. The first and third rows display the uncorrected $R_2^\star$ (a, g), the first order corrected $R_2^\star$ (b, h) and the second order corrected $R_2^\star$ (c, i). The second and fourth row shows the difference images displaying the difference in the $R_2^\star$ between first order corrected minus uncorrected $R_2^\star$ (d,j), the difference between second order corrected and uncorrected $R_2^\star$ (e,k) and the difference between the second order corrected and the first order corrected $R_2^\star$ (f,l). The right column displays the range of $R_2^\star$-values displayed in the images. Since image f,l are scaled between 0-0.01s^{-1}, these values are indicated between brackets.

each location of the image is on-resonance. However, the compensation is for up to second order effects only and therefore might be insufficient to remove all spurious phase effects. Although the SNR is not affected by the

multiplication with the correction factor, the contrast to noise might be increased [19].

The method can discriminate between macroscopic and mesoscopic signal dephasing and corrects only for macroscopic dephasing, as illustrated by Figure 5.6. This figure shows that the $R_2^\star$ is more homogeneous in both cylinders after correction for the macroscopic effects, while the mesoscopic effects are left unperturbed.

The SNR in the phase (derivative) images is inversely proportional to the SNR in the magnitude image [5]. The variation of the observed phase (derivative) is therefore largest at locations with the lowest signal magnitudes. Locations experiencing strong magnetic field gradients consequently show the most severe signal dephasing and are most difficult to correct for macroscopic signal dephasing. For example, in Figure 5.3 near the inner cylinder the signal is lost faster than in a region distant from the cylinder, because of the steeper change of the magnetic field near the inner cylinder. The lower SNR results in a large spread in the values the phase derivative can show, which still can be within the Nyquist-interval [5]. Since no threshold was applied on SNR, such values may arise at locations with low SNR. By applying Gaussian smoothing, the influence of such spurious values of the phase derivative were reduced. The effect on the resolution was minor because of the small width of the Gaussian used for the blurring. Obviously, when signal is completely lost, the phase derivatives can not be determined and hence the signal can not be recovered.

The local magnetic field and the echo time determine the amplitude of the phase and thereby also the size, shape and location of the dephased volume. Similarly, the phase derivatives and the corrections are governed by the product of the echo time and the shape of the magnetic field. For example, distant from the cylinder center in Figure 5.3 the first order derivative of the observed phase is nearly identical to the true value of the phase derivative, while close to the cylinder center this correspondence is reduced. At the locations, at which the measured and theoretical first order phase derivative start to deviate, first terms of the Taylor expansion results in a signal phase of approximately π or -π. At distances closer to the inner cylinder, the phase values are wrapped into the (-π, π]-interval. The location at which the theoretical and observed phase derivatives start to deviate is determined by both the echo time and the local magnetic field. Similarly, the area of total signal dephasing increases with the echo time. This is illustrated by the cylinder phantom in Figure 5.2. At shorter echo times, the phase derivative close to the cylinder can still be observed. Only in areas close to the cylinder,

the field is steep (Equation 5.11) and hence a large correction is applied to a relatively small volume. At longer echo times, the signal near the cylinder is dephased and the field gradients that can be assessed are more distant to the cylinder and more gradual. The corrections at longer echo times thereby affect a larger part of the phantom, but the correction is smaller in amplitude.

Although the correction can only result in an increase of the magnitude of the signal, the $R_2^\star$ can increase and decrease. An increase in the $R_2^\star$ is counter-intuitive, since the method should compensate for signal dephasing. The increases of the $R_2^\star$ after correction with respect to the $R_2^\star$ before correction are often relatively small and are to be ascribed to fitting to a wrong model. After correction, the data can be fitted more accurately, hence the errors in the fitting decrease and thereby an error in the original fitting can be corrected. Figure 5.5 and Figure 5.7 show that, by including the correction, the $R_2^\star$ shifts to lower values on average. In general, larger corrections of the signal amplitude result in larger corrections of the $R_2^\star$, as demonstrated near the inner cylinder in Figure 5.5 and near the nasal cavity in Figure 5.9. An example of an increase in $R_2^\star$ is illustrated by the arrow in Figure 5.7b. The correction of the infinite cylinder model affects a relatively small part of the total volume. Although the correction of the $R_2^\star$ for the infinite cylinder model visually appears to be small, the histograms shows a clear effect.

The methods that include the signal dephasing effect in the fitting model [12, 22], use the echo spacing instead of the echo times themselves. If the echo spacing is shorter than the shortest echo time itself, it allows stronger field gradients to be resolved. Thereby the fitting methods have the advantage of being able to compensate for field gradients stronger than can be determined at each echo [21]. The method presented in this work is limited to phase derivatives within the Nyquist interval, therefore only phase derivatives up to π/voxel can be observed and compensated for. This could possibly be bypassed by applying the evolution of the phase over time (fieldmap) and determining the spatial derivative thereof. Signals acquired with phase offsets higher than π/voxel can basically only be obtained for gradients that are well described by a few terms in the Taylor expansion. In realistic situations, for example Equation 5.11, magnetic fields are highly non-linear and when signal is dephased at a certain echo time, it will not return at a later time point. This implies that the fitting methods that include the signal dephasing effects in the fitting model correct the $R_2^\star$ as much or less than the model that corrects the data and fits the data to a mono-exponential model after applying the correction. This observation is illustrated in Figures 5.6 and 5.7.

Methods that include the signal dephasing effect in the fitting model suffer from a number of disadvantages. First, the need for multi-echo data for their correction lengthens the scan duration, which may be undesired for some applications. Second, applications that use the signal magnitude rather than $R_2^\star$, such as SWI [49], can not use the methods that compensate for the signal dephasing through their $R_2^\star$ fitting model. Signal dephasing, however, can negatively affect the results of these techniques. Third, often when a phase gradient is calculated resolution is lost [19]. Fourth, lack of validation of the obtained field gradients can make these methods error-prone [19, 22]. Fifth, whenever additional fitting parameters are used, the risk of ending up in a local minimum is increased [12, 22]. Figures 5.6 and 5.7 illustrate that, after correction, the fitting shows less artifacts than the $R_2^\star$ fitted including the correction in the model. Note that the expressions used in the present work are similar to those presented in [22]

The presented method corrects for signal dephasing in all three orthogonal directions. Since the data can be fitted to a mono-exponential decay after correction, the fitting can be linearized so as to make the fitting procedure faster, more stable and less likely to end up in a local minimum [115]. Fitting methods that include signal dephasing in more directions than the through-plane direction, require an increase in their number of fitting parameters. The method of Fernandez and Wehrli [12], for example, would require a multi-parameter fit with at least five parameters ($R_2^\star$, amplitude, G_x,G_y and G_z). Similarly, the method by Yang et al. [22] would lead to a fitting algorithm with at least eight fitting parameters ($R_2^\star$, amplitude, G_x,G_y and G_z, Laplacian$_x$, Laplacian$_y$ and Laplacian$_z$). Increasing the number of the fitting parameters in these models would reduce the stability and computational efficacy of both methods even further. Hence, the presented method is shown to be superior to fitting methods, which correct for macroscopic signal dephasing by an adapted fitting model, in terms of comprehensiveness, stability, and computational efficiency and speed.

The agreement between theory and experiment, as demonstrated by the infinite cylinder model, is excellent and values of the phase gradient obtained in the brain (up to 0.6 mT m^{-1}) closely correspond to values found by others [11, 22, 52, 105]. Furthermore, the correction of the $R_2^\star$ as achieved by our algorithm is in the order of magnitude as found with a fit model that included first order signal dephasing [12]. The improvements of the second order are best observed near the interfaces, at which the strongest transitions and hence second order phase derivatives are to be found e.g. near the air-tissue interface in Figure 5.8 and near the interface between the two

cylinders in Figure 5.6. Since non-linearities in a magnetic field usually depend on the strength of the magnetic field (or relative strengths of applied encoding/shimming gradients), the method is expected to yield a larger correction to data acquired at higher main magnetic fields strengths.

In the literature many processing techniques have been presented that, usually for radially acquired data, remove the influence of macroscopic field inhomogeneities. Although these postprocessing techniques have shown good results for removing signal dephasing as well as signal displacement, they can not perform without any costs. First, a field-map and a relaxation-map are necessary to correct for, amongst others, the translation and reduction of the signal intensity [110, 111]. In other words, the methods need additional acquisitions (often multi-echo) to be able to perform their correction, which can be time consuming. Furthermore, the maps might not correspond to the situation in which the corrected acquisition is performed. For example, in case of movement or differing shim settings, the acquired maps may give different values during acquisition of the images used for correction and images used to correct. Second, the corrected images are not always validated and the methods might end up in a local minimum. By contrast, the technique presented here compensates for macroscopic signal dephasing which is truly present within the object at the moment of acquisition. The method as presented in this work correct for a gradients in all directions. The fitting methods that include the signal dephasing effect in the fitting model correct for gradients in only one direction. As shown, for example in Figure 5.2, field gradients are usually not limited to a single direction. Correcting in one dimension only is therefore bound to result in residual errors.

In a recent paper by Testud et al [116] a method was proposed to allow calculation of the field-map on a single echo basis. In this paper the equivalence of phase [52, 58] and k-space [96, 116] based methods was proved. However, the need for filtering in k-space based methods makes them more error-prone and more susceptible to loss of resolution. The expressions, for the signal incoherence as shown in this work, show that phase-offsets are detrimental in case of signal loss and do not cause signal perturbations (phase factor in Equation 5.6, 5.7 and 5.9). These offsets are therefore often not taken into account in most correction algorithms. Hence field-mapping is often unnecessary to reduce signal dephasing artifacts. Because of the simplicity of our method, which does not require user intervention and preserves the resolution, we believe our method is superior to other, filter based, methods [68, 116].

An inhomogeneous magnetic field becomes more harmful when using larger voxelsizes and at higher magnetic field strengths [24]. Strong field variations not only result in signal dephasing, but in image distortion as well. The correction therefore suffers from image distortion (see e.g. Figure 5.5), especially at stronger magnetic field strengths. Note that the areas of signal pile-up correspond to areas with much signal dephasing, since both effects are linearly proportional to the local variation of the magnetic field [24, 117]. Since compensation algorithms apply changes before encoding, these are equally hampered by image distortions [3, 11, 48, 105, 106, 108, 109, 117]. Especially EPI based methods are known to be affected by signal distortions [5, 106, 107]. For all methods, the exact shape of the signal distortion depends on the strength of the encoding gradients, slice orientation and magnetic field distortion in the object [24, 117]. In practice the geometric distortion can often be kept within acceptable limits by carefully choosing experimental conditions, for example by applying a frequency encoding gradient with a large bandwidth. In the experiments using the infinite cylinder model, for instance, the intensity shift was limited to 0.9voxel at most at the edge of the inner cylinder, by using a frequency encoding bandwidth of 859Hz/voxel. The increased frequency encoding bandwidth, however, results in a loss in SNR. Future work will include modeling and reducing image distortions due to field (and phase) gradients, for example by using the method presented by Chen et al. [118]. Moreover, the effect of the corrections in other gradient echo acquisitions (blood flow, study of contrast/therapeutic agent) will be studied.

In conclusion we have shown a postprocessing method that corrects for macroscopic signal dephasing by using the complex data of a single or multiple gradient echo acquisition. The method may prove useful in studies that use R_2^*-weighted images, in particular if the spatial resolution is low, such as in fMRI.

Appendix 5.A Derivation signal dephasing

A gradient echo experiment results in the following expression for the signal S at location x_0, with voxel size Δx, constant spin density ρ and phase $\phi[x]$:

$$S[x_0] = \rho[x_0]\exp\left[i\phi[x_0]\right]\int_{-\frac{\Delta x}{2}}^{\frac{\Delta x}{2}} dx \exp\left[i\left(\frac{\partial\phi[x_0]}{\partial x}x + \frac{1}{2}\frac{\partial^2\phi[x_0]}{\partial x^2}x^2\right)\right] \tag{5.14}$$

$$= \rho[x_0]\ \exp\left[i\phi[x_0]\right]\int_{-\frac{\Delta x}{2}}^{\frac{\Delta x}{2}} dx\ \exp\left[i(ax+d)^2\right]\exp\left[-id^2\right] \tag{5.15}$$

$$= \rho[x_0]\ \exp\left[i\big(\phi[x_0]-d^2\big)\right]\int_{-\frac{\Delta x}{2}}^{\frac{\Delta x}{2}} dx \exp\left[i(ax+d)^2\right] \tag{5.16}$$

$$= \rho[x_0]\ \exp\left[i\big(\phi[x_0]-d^2\big)\right]\int_{-\frac{\Delta x}{2}}^{\frac{\Delta x}{2}} dx\ \exp\left[i\frac{\pi}{2}\left(\sqrt{\frac{2}{\pi}}(ax+d)\right)^2\right] \tag{5.17}$$

$$= \rho(x_0)\exp\left[i\big(\phi[x_0]-d^2\big)\right]\int_{-\frac{\Delta x}{2}}^{\frac{\Delta x}{2}} dx\ \exp\left[i\frac{\pi}{2}\Big(bx+c\Big)^2\right] \tag{5.18}$$

$$= \rho[x_0]\exp\left[i\big(\phi[x_0]-d^2\big)\right]\int_{-\frac{b\Delta x-2c}{2}}^{\frac{b\Delta x+2c}{2}} \frac{dy}{b}\ \exp\left[i\frac{\pi y^2}{2}\right] \tag{5.19}$$

$$= \frac{\rho(x_0)}{b}\ \exp\left[i\big(\phi[x_0]-d^2\big)\right]\left(\int_0^{\frac{b\Delta x+2c}{2}} dy\exp\left[i\frac{\pi y^2}{2}\right] + \int_{-\frac{b\Delta x-2c}{2}}^{0} dy\exp\left[i\frac{\pi y^2}{2}\right]\right) \tag{5.20}$$

$$= \frac{\rho[x_0]}{b}\exp\left[i\big(\phi[x_0]-d^2\big)\right]\left(\int_0^{\frac{b\Delta x+2c}{2}} dy\exp\left[i\frac{\pi y^2}{2}\right] + \int_0^{\frac{b\Delta x-2c}{2}} dy\exp\left[i\frac{\pi y^2}{2}\right]\right) \tag{5.21}$$

$$= \frac{\rho[x_0]}{b}\ \exp\left[i\big(\phi[x_0]-d^2\big)\right]\left(fcs\left[\frac{b\Delta x-2c}{2}\right] + fcs\left[\frac{b\Delta x+2c}{2}\right]\right) \tag{5.22}$$

$$\text{with } c = d\cdot\sqrt{\frac{2}{\pi}} = \frac{\partial\phi[x_0]}{\partial x}\Bigg/\sqrt{\pi\frac{\partial^2\phi[x_0]}{\partial x^2}},\ b = a\cdot\sqrt{\frac{2}{\pi}} = \sqrt{\frac{1}{\pi}\frac{\partial^2\phi[x_0]}{\partial x^2}} \tag{5.23}$$

The integral boundaries in Equation5.21 are deduced by applying that the integral in Equation 5.20 is even.

A man with one watch always knows the time. A man with two watches is never sure

---

L. Segal

Part II

Manipulation of image distortions induced by field inhomogeneities

Die Caricatur gibt oft ein wahreres Bild als die Photographie

A. Pichler

CHAPTER 6

Center-out radial sampling with off-resonant reconstruction for efficient and accurate localization of punctate and elongated paramagnetic structures

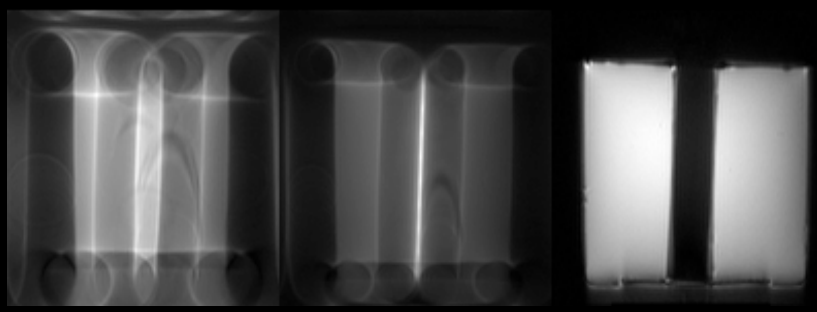

Published as: H. de Leeuw, P.R. Seevinck, and C.J.G. Bakker. Center-out radial sampling with off-resonant reconstruction for efficient and accurate localization of punctate and elongated paramagnetic structures. *Magnetic Resonance in Medicine*, DOI: 10.1002/mrm.24416, 2012

Abstract

Accurate localization of interventional devices, for example, brachytherapy seeds and needles, is desired for interventional procedures. MRI is usually considered unsuitable for this purpose, as the induced signal voids and the signal pile-ups do not necessarily represent the exact location of the devices. Center-out RAdial Sampling with Off-Resonance reception (co-RASOR) has been shown to solve this problem by repositioning the signal pile-up onto the geometrical center of the interventional devices. However, the multiple acquisitions that are required for co-RASOR resulted in a low efficiency and unsuitability for near real-time interventional purposes.

In this work we aim to increase the efficiency of co-RASOR by relying on multiple off-resonance reconstructions of a single acquisition rather than on multiple acquisitions. The soundness of this approach is demonstrated by showing the equivalence of acquisition co-RASOR and reconstruction co-RASOR, both theoretically and experimentally. An algorithm is proposed and evaluated to obtain the geometric centers of the devices, while suppressing the background. This procedure is shown to be effective, *in vitro* as well as *ex vivo*, and to yield signal intensity increases in the order of 150-400% of the average signal, in the geometric center of a brachytherapy seed and a needle. The geometric accuracy of the resultant images is confirmed by computed tomography.

6.1 Introduction

Accurate localization of interventional devices and appliances is a desirable feature for the planning and evaluation of interventional procedures. This is, e.g. the case in needle-directed drug delivery or when performing a needle biopsy [119–121], in locating fiducial markers applied to guide external beam radiation therapy [20, 122–124], when evaluating the position of electrodes in neurosurgery [125], or to enable assessment of the radiation-absorbed dose in brachytherapy [126, 127]. Unfortunately, accurate localization of interventional devices by MRI is a difficult task for a number of reasons. First, these devices typically do not generate signal themselves. Second, the paramagnetic materials, which are often used to construct the devices, disturb the homogeneity of the local magnetic field in the surrounding tissue, causing signal loss, signal pile-ups and geometric distortion [123, 128–131]. As a result, the signal voids and signal pile-ups, by which the field disturbing objects reveal their presence, do not necessarily reflect their exact position.

In the past decade, many techniques have been presented to improve the accuracy and specificity of MRI in depicting interventional devices [3, 45, 48, 51, 52]. These methods usually exploit the frequency perturbation induced by the devices to generate high signal intensity in their vicinity, while suppressing the background. In some methods, the effects of the frequency perturbations during signal excitation are exploited [45, 48], while other methods utilize the off-resonance effects during signal formation [3, 51, 52]. To date these MRI methods do not yield the desired accuracy and efficiency as, for instance, achieved by the gold standard, X-ray computed tomography (CT). The accuracy is often limited by device-induced geometrical distortions, as a consequence of which high signal intensity is generated in the vicinity of the perturbing object, which does not match with the true location of the perturbing object. On the other hand, the efficiency is often suboptimal since multiple acquisitions are necessary to obtain the desired positive contrast image as well as an anatomical reference image [3, 45, 48, 51, 52].

Recently, however, center-out RAdial Sampling with Off-Resonance reception (co-RASOR) was presented which, in principle, solves the localization problem by forcing signal to pile-up in the geometrical center of punctuate and elongated paramagnetic structures, such as brachytherapy seeds and biopsy needles [4]. In the co-RASOR technique, a frequency offset is applied during signal reception in a center-out radial acquisition. By applying this frequency offset, a high signal pile-up can be generated in the geometrical center of a field perturbing object on the condition that the appropriate

frequency offset is chosen [4]. In its current implementation, the co-RASOR acquisition method suffers from a number of practical limitations. First, the frequency offset needs to be chosen prior to scanning. As the required frequency offset depends on the size and orientation of the perturbing object, it cannot always be determined with sufficient accuracy prior to acquisition. Second, when multiple perturbing objects are present, one frequency offset is usually not effective for all field perturbing objects. Often, therefore, a number of acquisitions with different frequency offsets need to be performed to achieve optimal visualization of each object. Third, by applying the global frequency offset during acquisition, the entire image will be degraded by blurring and streaking artifacts due to widening of the point-spread function [132, 133], resulting in a sub-optimal anatomical image. As a result, the technique in its current state is inefficient and hence unsuitable for the type of MR guided procedures mentioned above.

In the work presented here, we aim to show that the low temporal efficiency of co-RASOR can be overcome by relying on multiple off-resonance reconstructions of a single acquisition rather than on multiple acquisitions. To achieve this goal, we start with a summary of the principles of co-RASOR. Next, the soundness of the reconstruction approach is shown by, theoretically and experimentally, demonstrating the equivalence of acquisition co-RASOR and reconstruction co-RASOR. Having established this equivalence, a semi-automatic algorithm is proposed and evaluated by which the multiple off-resonance reconstructions can be exploited to extract the geometric centers of the devices semi-automatically, while suppressing the background. The potential of reconstruction co-RASOR for interventional applications is subsequently demonstrated with experiments involving brachytherapy seeds and an MR compatible biopsy needle at different orientations with respect to the main magnetic field. The geometric accuracy of the resultant images is confirmed by CT.

6.2 Theory

6.2.1 Geometric distortions in 1D

To explain the principles behind co-RASOR, a simple one-dimensional (1D) case is considered. When placed in a magnetic field (B_0) a punctuate or elongated object, with a magnetic susceptibility that deviates from the surrounding medium, induces a local magnetic field disturbance. The resultant magnetic field distortion induces a resonance frequency offset, which interferes

with the spatial encoding of the signal along the frequency encoding direction. By introducing a frequency offset (δf_0) after signal excitation, the effect of the local magnetic field offset on the spatially encoded signal can be manipulated [4, 133]. This can readily be appreciated by considering the 1D frequency encoded signal in the Fourier domain.

$$\begin{aligned} s(k) &= \int_V dx'\ s_0(x') e^{-i2\pi(\gamma\Delta B(x')+\delta f_0)TE} e^{-R_2^\star TE} e^{-i2\pi\gamma G\cdot x' t} e^{-i2\pi(\gamma\Delta B(x')+\delta f_0)t} \\ &= s(\gamma Gt) = \int_V dx'\ s(x', TE) e^{-i2\pi\gamma G\cdot x' t} e^{-i2\pi(\gamma\Delta B(x')+\delta f_0)t} \end{aligned} \tag{6.1}$$

In Equation 6.1, an infinite slew rate of the gradient ramp-up is assumed and integration extends over the total excited volume. Further, x' denotes the coordinate in the excited object, γ the gyromagnetic ratio divided by 2π, $\Delta B(x')$ the local magnetic field offset, δf_0 the applied global frequency offset, TE the echo time, $R_2^\star$ the transverse relaxation rate, G the frequency encoding gradient, t the time of encoding with respect to the center of k-space determined by the TE, and s(x',TE) the signal amplitude. The latter includes signal relaxation effects ($R_2^\star$) and effects on the signal phase e.g. $2\pi\delta f_0 TE$. Intravoxel signal dephasing ($R_2^\star$) during acquisition, which results in an additional filter on the data, see e.g., [5, p286-287], is neglected. In the image domain, introduction of a global frequency offset results into a displacement of the signal. This can readily be appreciated by considering the reconstructed 1D signal.

$$\begin{aligned} s(\hat{x}) &= \int_{kspace} dk\ \ s(k)\, e^{i2\pi kx} \\ &= \int_{t_{min}}^{t_{max}} \gamma G\, dt \int_V dx'\ s(x', TE) e^{-i2\pi\gamma G\cdot x' t} e^{-i2\pi(\gamma\Delta B(x')+\delta f_0)t} e^{i2\pi\gamma G\cdot xt} \\ &= \int_{t_{min}}^{t_{max}} \gamma G dt \int_V dx'\ s(x', \mathrm{TE}) e^{-i2\pi\gamma\left(G\cdot\left(x'-x+\frac{\Delta B(x')}{G}+\frac{\delta f_0}{\gamma G}\right)\right)t} \\ &= \int_V dx'\ s(x', \mathrm{TE})\delta(x'-x+\delta x) \\ &= s(x+\delta x, \mathrm{TE}) \end{aligned} \tag{6.2}$$

with $k = \gamma Gt$, t_{min} and t_{max} the start point and end point of the signal encoding, respectively, and $s(\hat{x})$ the signal in the reconstructed image. The right hand side of Equation 6.2 displays an integral over the excited volume.

Signal intensity in the reconstructed image corresponds to the summation of signal from locations with the same value for $\hat{x}$.

$$\hat{x} = x + \delta x = x + \frac{\gamma \Delta B(x) + \delta f_0}{\gamma G} \tag{6.3}$$

In other words, the signal at location $\hat{x}$ in the image consists of the signal originating from multiple locations within the excited object with the same value for $x + \delta x$. Since the amplitude of the magnetic field of the perturbing object is inversely proportional to the distance from its center, signal will be shifted nonlinearly in the frequency encoding direction. This shift will result in signal pile-up when the field disturbance opposes the readout gradient and results in signal smear when the field perturbation adds to the readout gradient [24, 133]. Equation 6.3 illustrates that, by applying a frequency offset, the signal displacement can be manipulated. Obviously, a global frequency offset will result in a reduction of image distortion at some locations, while increasing the image distortion, such as blurring and streaking, at other locations [133].

6.2.2 Principles of co-RASOR

In this section, we examine the effect of a frequency offset to a center-out radial acquisition. This is most easily done for a 1D case. The effect of a frequency offset during center-out encoding is illustrated in 1D in Figure 6.1.

Figure 6.1 illustrates the main steps involved in co-RASOR. An additional local field gradient due to a field perturbing object (Figure 6.1b) results in an effective precession frequency that differs from the intended linearly varying frequency during frequency encoding (Figure 6.1c). Local field gradients steeper than the intended frequency encoding gradient result in signal smear, while more gradual local field gradients lead to signal pile-up (Figure 6.1d). The position of the signal pile-up and signal smear, with respect to the field perturbing object, is determined by the sign of the frequency encoding gradient. Application of a global frequency offset results in a shift of the object parallel to the encoding gradient (Figures 6.1f, g). A single frequency offset, present during two frequency encoding gradients with the same amplitude but opposite sign, results in a shift of the pixels involved in two opposing directions (Figures 6.1f, g). Hence, in case of center-out sampling, signal pile-up from both sides of the perturbing object will be pushed back to the exact center of the perturbing object at one specific frequency

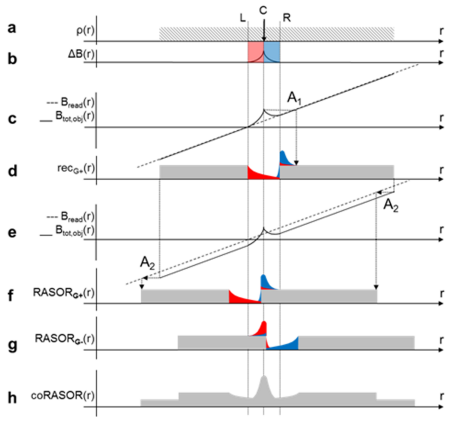

Figure 6.1: Principles of reconstruction co-RASOR in 1D. An object with constant spin density ρ(r) (gray hatched area, a), containing a small paramagnetic object at location C. When placed in a magnetic field, the object induces a nonlinear magnetic field distortion (ΔB), as schematically depicted in (b). On the left side of the field perturbing object, a positive field gradient is induced between the edges L and C (red). At the right side of the object a negative field gradient is induced between the edges C and R (blue). In (c), the dotted line represents the linear magnetic field gradient (B_{read}) related to a positive read gradient (G+). The black line represents the total magnetic field in the object ($B_{tot,obj}$=B_{read}(r)+ ΔB(r)). At locations at which the intended and true field gradient do not coincide, the spatial encoding is disturbed, leading to signal smear (steep $B_{tot,obj}$, red area) and signal pile-up (flat $B_{tot,obj}$, blue area), as depicted in (d). Arrow A_1 demonstrates the erroneous spatial encoding of signal in the direct vicinity of the field perturbing object. In (e), a frequency offset is applied during reconstruction (dotted line). The constant frequency offset causes the entire object to shift to the left, as shown in (f) and pointed out by arrows A_2. The frequency offset is taken such that the blue signal pile-up (d) is repositioned at the exact center of the field perturbing object (location C in a). Similarly, when using a negative read gradient (G-) the red area will pile-up. Also the red piled-up signal can be repositioned at the exact center of the field perturbing object, resulting in the intensity profile as depicted in (g). By averaging the positive and negative read gradients (co-RASOR, h), high positive contrast at the exact center of the field perturbing object is obtained.

offset (Figure 6.1h). The focusing of the signal pile-up from both sides simultaneously leads to an artificial, well localized, high signal intensity in the center of the object. The on-resonance acquired signal, however, will also be displaced by the applied global frequency offset. This can be recognized at both edges of the object, presenting signal of half the original signal amplitude, at locations at which originally no signal was present (Figure 6.1h).

During a center-out radial acquisition, the frequency encoding gradient traverses each direction of encoding. In 1D, the encoding traverses two directions (Figure 6.1 and Equations 6.1-6.3), while in two-dimensional (2D) imaging and three-dimensional (3D) imaging the number of encoding directions scales with the applied matrix size. In 2D and 3D the signal of each location in the image will be radially displaced (radius δx) and divided over a ring, or spherical shell, respectively.

As the frequency encoding is applied along all directions of encoding, the image distortion is determined by the amplitude of the field disturbance ($|\Delta B|$) and not by its sign, as indicated by the fraction $\frac{\gamma\Delta B(x)}{\gamma G}$ in Equation 6.3. Since punctuate and elongated field perturbing objects experience symmetry of the field surrounding their center, a radially symmetric signal pile-up is obtained surrounding a perturbing object. co-RASOR redirects the radially symmetric signal pile-up towards the center of the object by applying a global frequency offset during the radial spatial frequency encoding. The focusing of the signal results in an artificial signal pile-up in the geometric center of the object.

6.2.3 Reconstruction co-RASOR

As a global frequency offset is constant over space, it can be applied either during acquisition, as in the original acquisition co-RASOR, or retrospectively, during reconstruction, here referred to as reconstruction co-RASOR [110].

$$\begin{aligned} s(k) &= \int_V dx'\ s(x', TE) e^{-i2\pi\gamma G\cdot x' t} e^{-i2\pi(\gamma\Delta B(x') + \delta f_0)t} \\ &= e^{-i2\pi\delta f_0 t} \int_V dx'\ s(x', TE) e^{-i2\pi\gamma G\cdot x' t} e^{-i\gamma\Delta B(x')t} \end{aligned} \tag{6.4}$$

As shown by Equation 6.4, the same results are to be anticipated when the frequency offset is applied during acquisition, as in acquisition co-RASOR, as when the frequency offset is applied during reconstruction. The major

advantage of applying the frequency offset during reconstruction is a gain in efficiency: for each field perturbing object an adequate frequency offset can be determined and applied retrospectively on the basis of a single acquisition. All required information is, therefore, obtained with a single acquisition, whereas acquisition co-RASOR requires at least multiple acquisitions, especially when multiple perturbing object are involved.

6.3 Methods

6.3.1 Phantom setup

Phantom A was designed to illustrate some salient features of the co-RASOR technique. In particular, it was used to show the equivalence of acquisition co-RASOR and reconstruction co-RASOR, to demonstrate the accurate localization of the center of field perturbing objects and to illustrate the different steps involved in reconstruction co-RASOR. The phantom consisted of a 17.4 mM Holmium(III)-doped agarose gel (2%), with a volume susceptibility of 0.3 ppm to closely match the susceptibility of air [42]. In the gel, two glass spheres were inserted with a diameter of 14 mm and 8 mm, respectively.

Phantom B consisted of a 7-cm-thick highly inhomogeneous piece of porcine tissue containing fat, connective tissue and bone, submersed in an agarose gel doped with 32 mg $MnCl_2.4H_2O$ per liter distilled water. The porcine tissue contained four brachytherapy seeds (Isotron Isotopentechnik GmbH, Solingen, Germany), positioned two by two at an angle of 90°. The brachytherapy seeds had a diameter of 0.8 mm and a length of 4.5 mm and consisted of a silver core in a titanium tube with hemispherical ends, as shown in Figure 6.7a. The phantom was positioned in such a way that two seeds were aligned with B_0 and two were oriented perpendicular to B_0 [134].

Phantom C consisted of a similar piece of porcine tissue in which a biopsy needle (18G Coax Needle, Invivo, Schwerin, Germany) was inserted. The biopsy needle was a full-core titanium biopsy needle with an outer cannula featuring a modified Menghini bevel cut, with an insertion length of 100 mm. Phantom C was oriented at 0°, 45° and 90° with respect to B_0, to cover the full range of artifacts that may arise during needle interventions.

6.3.2 Imaging parameters

MR imaging was performed on a 1.5T whole body MRI (Achieva; Philips Healthcare, Best, The Netherlands). Phantom A and B were scanned using

a birdcage head coil. Phantom C was scanned utilizing a surface coil with two elliptical elements, with short axis 14 cm and long axis 17 cm. A 3D free induction decay (FID) was acquired using a center-out radial read-out. Two acquisitions were performed on phantom A to validate reconstruction co-RASOR and to study the effect of the imaging resolution. The imaging parameters for phantom A included: First scan: nonselective excitation by a radiofrequency (RF) block pulse with a bandwidth of 26 kHz, field of view (FOV) 128^3 mm^3, scan matrix 128^3, TE 0.15 ms, repetition time (TR) 4.7 ms, flip angle (θ) 15°, read-out bandwidth 868 Hz/pixel and one signal average, resulting in a scan duration of 2 min and 34 s. Second scan: non-selective excitation by a RF block pulse with a bandwidth of 26 kHz, FOV 128^3 mm^3, scan matrix 64^3, reconstructed to 128^3, TE 0.18 ms, TR 6.1 ms, θ 15°, read-out bandwidth 1750 Hz/pixel and one signal average, resulting in a scan duration of 50.7s. The scan parameters for phantom B and phantom C included the same excitation pulse as for phantom A, FOV 176^3 mm^3, scan matrix 176^3, TE 0.15 ms, TR 5.5 ms, θ 15°, read-out bandwidth 887 Hz/voxel and one signal average, resulting in a total scan duration of 5 min and 39 s. Phantom A was scanned three times: one scan in on-resonance, one scan with a frequency offset of 2 kHz and one scan with a frequency offset of 4 kHz.

To validate the geometric accuracy of co-RASOR, CT images were acquired in addition to the MR acquisitions. CT images were acquired on a 64-slice CT scanner (64-slice Brilliance, Philips Healthcare, Best, The Netherlands) with the following parameters: Phantom A, B: voltage 80 kV, mAs 250, in-plane resolution 0.34 mm, increment 0.33 mm. Phantom C: voltage 120 kV, mAs 263, in-plane resolution 0.45 mm, increment 1 mm. No correction for beam hardening was applied. Reconstruction was performed using a filtered back projection reconstruction method, with a filter type B (Philips Healthcare, Best, The Netherlands).

6.3.3 Reconstruction and postprocessing

Postprocessing was performed using Matlab (The MathWorks, Natick, MA). The radially acquired k-space data, interpolated to a rectangular grid, was exported from the scanner database (Achieva; Philips Healthcare, Best, The Netherlands). For each frequency offset applied during reconstruction co-RASOR, a phase ramp was applied in k-space. The phase ramp consisted of a multiplication of the complex data by $e^{-i2\pi\delta f_0 t'}$, which corresponds to the first exponential in Equation 6.4. In total 160 image reconstructions were performed, with frequency offsets between -8 kHz and 8 kHz with a step size

of 100 Hz. Off-resonance reconstruction of a 128^3 dataset required 2 seconds per reconstruction, as performed on a Dell Optiplex 760 with a 2.5 GHz quad core processor.

The geometric accuracy of the two co-RASOR methods was evaluated by registering the co-RASOR images to CT image via rigid registration, which applies translation and rotation only, using elastix [88]. Maximum intensity projections (MIPs) were constructed, for both the CT images and co-RASOR images. For anatomical reference, the co-RASOR MIP was overlaid on a minimum intensity projection of the corresponding slices of the original on-resonance MR images.

6.3.4 Automatic extraction of the magnetic center of the field perturbing objects

A two-step semi-automatic algorithm was developed to determine the optimal frequency offset i.e. the frequency offset at which the signal intensity is focused in the geometric center of the object, and to suppress the background signal. In the first step of the algorithm, the frequency offset is determined at which the signal is highest for the object under consideration. In the second step, the signal in the surrounding structures is suppressed by setting a threshold at three standard deviations above the average signal intensity in the surrounding tissue [5, 19].

In Figure 6.2, the steps involved are illustrated for a single sphere. First, the image is reconstructed at a range of frequency offsets. Second, the average and standard deviation of the noise are determined from the histogram of the on-resonance image. Third, the maximum of the signal intensity as a function of the frequency offset is determined for each voxel (Figure 6.2, index A), providing the highest possible signal intensity for each voxel and the frequency offset at which this maximum occurs, which we call the optimum frequency offset. Fourth, in this maximum intensity image, the voxel with the maximum signal intensity is selected. The corresponding frequency offset is the optimal frequency offset. The image reconstructed at this optimal frequency offset is selected (Figure 6.2, index B). Fifth, to selectively depict the perturbing object, the on-resonance acquired image (Figure 6.2, index O) is subtracted from the image at the optimal frequency (Figure 6.2, index C). Finally, the background is suppressed by setting all signal below the threshold to zero (Figure 6.2, index D). In this final step, signal intensity not associated with the magnetic center of the perturbing object is suppressed.

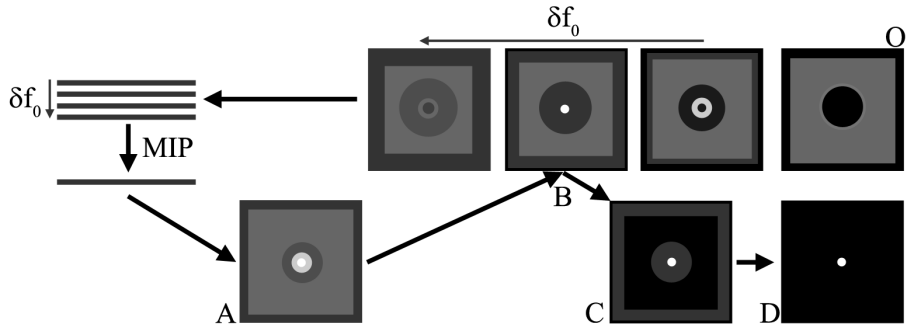

Figure 6.2: Schematic depiction of the algorithm to automatically select the optimal frequency offset for a field perturbing object. After acquisition of an image (top right, O), first images at multiple frequency offsets are reconstructed. Of these images, for each specific voxel the maximum signal intensity as function of the frequency is determined (bottom left, A). Hereafter the optimal frequency offset of the entire image is determined, which corresponds to the highest signal intensity in the image. Subsequently, the image reconstructed at the optimal frequency offset is selected (B). In the image at the optimal frequency offset, the background signal is suppressed by subtracting the on-resonance image (C) and by applying the threshold (D).

In the case of multiple field perturbing objects, multiple frequency offsets may be necessary, since each object may have its own optimal frequency offset. In such cases, the algorithm was applied iteratively. Referring to Figure 6.2, the algorithm is continued as follows: The positive contrast image (Figure 6.2, index D) is subtracted from the optimal frequency offset image (Figure 6.2, index A). In the resulting image, the signal intensity corresponding to the first object is removed. The algorithm is subsequently continued at step four, at which the highest signal intensity is determined, to select the second object and so on. The iterations are stopped whenever the highest signal intensity at the fourth step is below the threshold. The final positive contrast image, which depicts the geometric center of the field perturbing objects, is formed by a summation of all individual positive contrast images.

6.4 Results

6.4.1 Comparison of acquisition co-RASOR and reconstruction co-RASOR

In a series of experiments performed on phantom A, acquisition co-RASOR and reconstruction co-RASOR showed strong similarity, as demonstrated for a transversal slice through both spheres in Figure 6.3. The off-resonance images (Figures 6.3b, c, e and f) display a ring with reduced signal intensity at the edge of the phantom, in accordance with the 1D theoretical profiles in Figure 6.1. Furthermore, acquisition co-RASOR and reconstruction co-RASOR present similarly shaped hyperintensities at both frequency offsets. Acquisition co-RASOR and reconstruction co-RASOR also show the same signal-to-noise level, 20.7 and 20.5 for acquisition and reconstruction co-RASOR, respectively.

Some subtle differences between acquisition co-RASOR and reconstruction co-RASOR can be discerned in Figure 6.3. One of these differences is the black ring surrounding the phantom in acquisition co-RASOR, which is absent in reconstruction co-RASOR. This artifact is likely caused by ringing [132]. Another difference between acquisition co-RASOR and reconstruction co-RASOR is the signal pile-up, which is higher in intensity and less blurred for acquisition co-RASOR than for reconstruction co-RASOR. This difference can probably be attributed to regridding artifacts, partial volume effects and noise. Figure 6.3 further reveals that reconstruction co-RASOR can be used to remove a global frequency offset that has been applied during signal acquisition, as illustrated by the strong correspondence of Figures 6.3a, 6.3d. However, also in this case imaging artifacts, such as ringing artifacts and regridding artifacts, remain in the data and result in small differences between acquisition co-RASOR and reconstruction co-RASOR.

6.4.2 Characterization and optimization of reconstruction co-RASOR

After having established the equivalence of acquisition co-RASOR and reconstruction co-RASOR, the latter was employed to study the effect of the frequency offset on the spheres in phantom A in greater detail. Figure 6.4 illustrates that a single frequency offset is not sufficient to generate optimal positive contrast for both spheres simultaneously. The optimal frequency offset appears to be approximately +4 kHz for the small sphere and +7 kHz

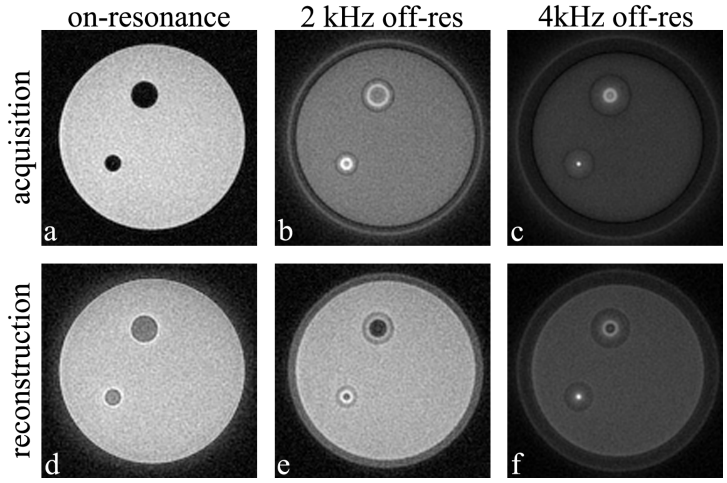

Figure 6.3: Transversal slice through the center of one of the glass spheres in phantom A. The left column shows on-resonance images, while the second and third column show the images with a frequency offset of 2kHz and 4kHz, respectively. The top row shows the acquired co-RASOR images, while the bottom row shows the reconstructed co-RASOR images. Image d shows the image acquired with a frequency offset of 2kHz, reconstructed on-resonance.

for the large sphere. Furthermore, Figure 6.4 shows that positive and negative frequency offsets of equal magnitude yield nearly identical results.

The algorithm to automatically extract the optimal frequency offset for each sphere is illustrated by Figure 6.5. As the phantom contained multiple perturbing objects, the algorithm that extract the optimal frequency automatically, which is illustrated in Figure 6.2, is performed iteratively. The automatically determined optimal frequency offsets were 7 kHz and 4.25 kHz for the large and small sphere respectively. These offsets agree well with the optimal frequency offsets indicated in Figure 6.4. The maximum signal intensity at the optimal frequency offset for the small sphere is approximately four times higher than the average signal in the surrounding medium. The large sphere shows a signal intensity maximum at the optimal frequency offset approximately six times higher than the average signal in the surrounding medium.

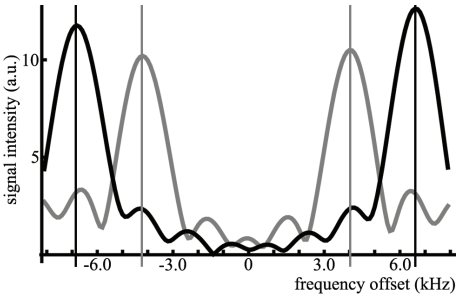

Figure 6.4: Signal intensity at the center of the large sphere (black) and the small sphere (gray), as a function of the resonance frequency offset for 160 reconstructions between -8 kHz and 8 kHz, with step size δf_0 100 Hz. The vertical lines indicate the position of the signal maxima.

A close correspondence is observed between the co-RASOR images that were acquired and reconstructed at different imaging resolutions (Figure 6.6 top row, bottom row). The low resolution image required frequency offsets 12.5 kHz and 7 kHz for the optimal depiction of the center of the large and small sphere, respectively. The bottom row shows that co-RASOR is also effective when a larger percentage of the data -68% with respect to 6% for the high resolution image- is sampled on the slope of the gradient. Both images displayed the same location for the signal pile-up. The high signal intensity in the low resolution images was more blurred and its amplitude was lower. The amplitude of the signal pile-up was two times and three times higher than the average signal in the background for the small and large sphere, respectively. To determine the accuracy by which the centers of the spheres were located in the co-RASOR image, the co-RASOR images were rigidly registered to X-ray CT images, as shown in Figure 6.6. A close correspondence was observed between the locations of the sphere centers on the co-RASOR images and the corresponding locations of the centers on the CT images. Before registration, the Euclidean distance between the two centers on co-RASOR and CT was 44.4 mm and 44.3 mm in the coronal plane, 14.1 mm and 14.0 mm in the transversal plan, and 42.4 mm and 42.0 mm in the sagittal plane. After registration, the location of the center of the spheres was the same for both image modalities. This agreement points to an accuracy within 1 mm, which is the size of the voxel.

6.4.3 *In vitro* demonstration of reconstruction co-RASOR

The applicability of the reconstruction co-RASOR method to locate punctuate and elongated perturbing objects in inhomogeneous tissue was demonstrated on phantom B and phantom C. A typical result on a piece of porcine tissue with four brachytherapy seeds is shown in Figure 6.7. Although

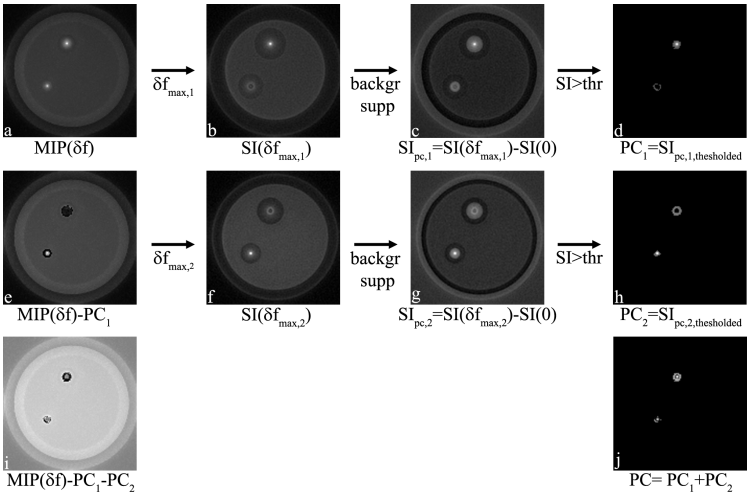

Figure 6.5: Illustrations of the co-RASOR algorithm for phantom A. First, the optimal frequency offset is determined for each voxel by applying a MIP as function of the reconstructed frequency offset (**a**). Second, the maximum signal intensity (SI) in the optimal frequency offset image is determined and the image at the optimal frequency offset selected (SI(7kHz), **b**). After suppressing the background by subtracting the on-resonance image (SI(7kHz)-SI(0), **c**), the threshold was applied to suppress the background and obtain a positive contrast image (PC_1, **d**). The positive contrast image was subsequently subtracted from the optimal frequency offset image (MIP(δf)-PC_1, **e**). The second highest intensity corresponded to the signal intensity in the center of the small sphere, at a frequency offset of 4250Hz (SI(4.25kHz), **f**). After suppression of the background by subtraction of the on-resonance image from the image at the second optimal frequency (SI(4.25kHz)-SI(0), **g**), the threshold was applied to suppress the background and obtain the second positive contrast image (PC_2, **h**). Subsequently, the high signal intensity in the optimal frequency offset image, corresponding to the second optimal frequency offset, was suppressed by subtracting the second positive contrast image from the image at optimal frequency offset (MIP(δf)-PC_1-PC_2, **i**). The third highest signal intensity in the optimal frequency image was below the threshold. The total positive contrast image was formed by merging the two positive contrast images (PC_1+PC_2, **j**).

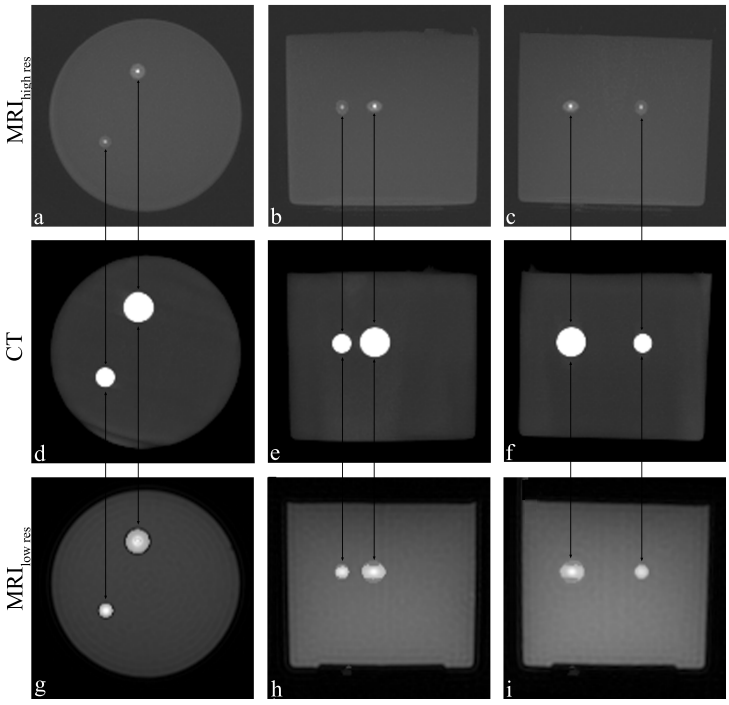

Figure 6.6: Top and bottom row: sum of minimum intensity projection of the on-resonance acquired image and a maximum intensity projection of the co-RASOR MRI images for a number of relevant slices containing the spheres. Middle row: maximum intensity projections of the same slices of the CT images, after image registration with MRI. The top row shows the MRI images acquired with a high image resolution, the bottom row the MRI images acquired with a low resolution. Shown are projections along the three orthogonal imaging directions to demonstrate the 3D character of the technique. The arrows indicate the close correspondence between the locations of the centers found on co-RASOR images and on CT images.

the brachytherapy seeds are positioned in two orientations, one frequency offset (1.5 kHz) was found to be sufficient for the optimal positive contrast image for all seeds. Since the shape of the titanium ends is nearly spherical, as shown in Figure 6.7a, this was to be expected. The centers of the seeds are easily identified, as shown in Figure 6.7b. The overlay shows the

anatomy as well as the location of the seeds as obtained from a single acquisition. A high degree of correspondence was observed between the position of the seeds as determined from the co-RASOR images (Figure 6.7b) and the CT images (Figure 6.7c). The same close correspondence was observed for the distances between the paramagnetic ends of the seeds. The dimensions extracted from the distances between the two maxima for each seed in co-RASOR were 4.0 mm, 4.0 mm, 4.1 mm and 3.2 mm, which is in good agreement with the actual distance of 4.1 mm as shown in Figure 6.7a. The distance of 3.2 mm is still within one voxel from the true distance and is to be attributed to partial volume effects. The maximum intensity in the co-RASOR positive contrast image showed a signal increase of approximately 150% with respect to the surrounding tissue.

Figure 6.8 shows the result of the experiments on a needle in porcine tissue for three orientations with respect to the main magnetic field. These three experiments reflect conditions that may be encountered while performing, e.g., a biopsy. Other than for the brachytherapy seeds, optimal results for the three needle orientations in Figure 6.8 required three different frequency offsets: 1.0 kHz for the needle nearly parallel to B_0, 2.5 kHz for the needle at 45° with respect to B_0 and 2.75 kHz for the needle perpendicular to B_0. Signal increases ranged between 250 and 400% of the average signal intensity for the needle nearly parallel to B_0 and the needle perpendicular to B_0, respectively. The signal intensity was highest at the tip for all orientations of the needle. The relatively short repetition time used in these experiments (5.5 ms) and the chemical shift of fat resulted in high signal intensities from fatty tissue in Figure 6.8.

6.5 Discussion

In previous work [134] we have shown that high positive contrast can be obtained in the geometrical center of punctuate and elongated paramagnetic structures using acquisition co-RASOR. In the work presented here, it was demonstrated that the high positive contrast can be obtained by relying on off-resonance reconstructions instead of applying off-resonance acquisitions. This change from acquisitions to reconstructions was shown to yield a dramatic gain in efficiency and flexibility, as it enabled to perform reconstructions at arbitrary off-resonances on the basis of a single acquisition. The gain in efficiency was most pronounced when dealing with multiple perturbing objects requiring different optimal frequency offsets. Re-

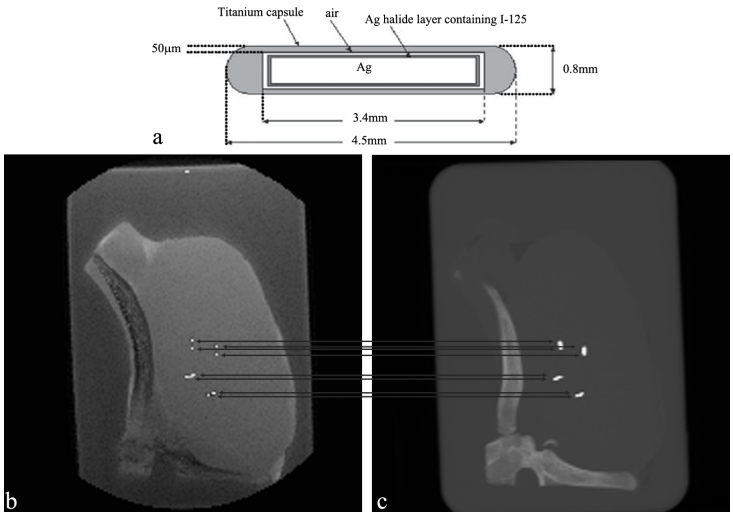

Figure 6.7: a: schematic depiction of a brachytherapy seed. The most prominent characteristics are the Ag-core and the titanium ends. Minimum intensity projections of the magnitude image merged with the maximum intensity projection of the positive contrast co-RASOR images, over all slices containing the seeds in phantom B, are shown in image b. The right image (image c) shows the maximum intensity projection of the CT image over the same slices as used for image b. The arrows indicate the location of the highest signal intensity of the positive contrast in the co-RASOR image and the corresponding location on CT.

construction co-RASOR was shown to accurately locate the geometric centers of punctuate and elongated field perturbing objects in homogeneous as well as heterogeneous environments. The proposed threshold allowed suppression of nearly all background signal, while the relevant signal increases are maintained. The location of the center of the field perturbing objects on the co-RASOR images agreed to within one voxel with the locations of the centers on CT. Also the object dimensions determined from co-RASOR images corresponded to the known object dimensions to within one voxel. Dedicated postprocessing of reconstructed co-RASOR images was further shown to allow optimal localization of the center of a perturbing obect semi-automatically and with good reproducibility. The only manual inputs nee-

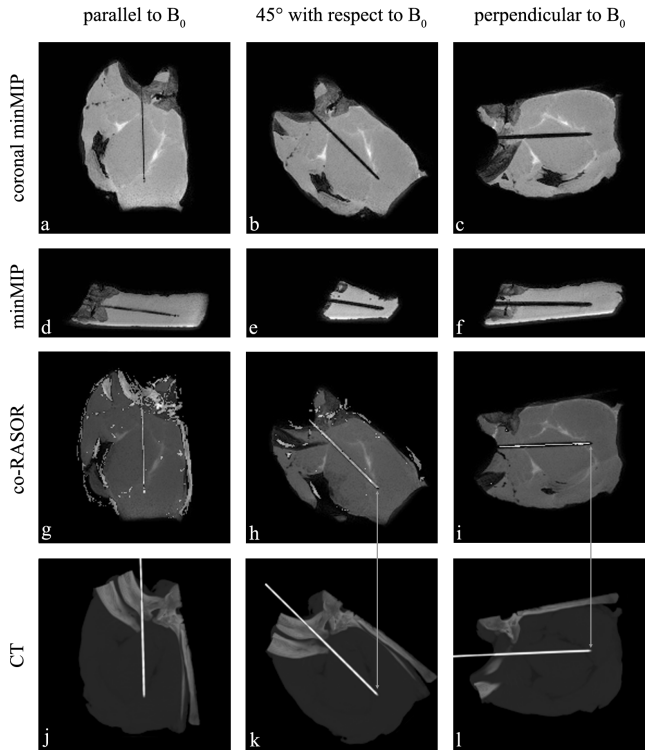

Figure 6.8: Results of the needle experiments for three orientations with respect to B_0. The first column shows results for the needle nearly parallel to B_0 (approximately 6° with respect to B_0). The second column displays the results for the needle 45° with respect to B_0, the third column for the needle perpendicular to B_0. The first two rows show two perpendicular minimum intensity projections of magnitude image over slices containing the needle. The third row shows the maximum intensity projections of the positive contrast co-RASOR MRI images added to minimum intensity projections of the on-resonance acquired image. The fourth row shows the maximum intensity projections of the CT images of the needle in porcine tissue.

ded were the value for the threshold to suppress background signal and the number and size of the frequency steps applied during reconstruction.

When viewing our results against literature findings, the following obser-

vations can be made. In the last decade many postprocessing techniques have been proposed to remove blurring due to field inhomogeneities [110, 111, 133, 135–137]. These methods either apply additional magnetic field maps [135, 137], extract field offsets from the data [111] or apply additional reconstructions [133] to reduce image distortion during reconstruction. Like these techniques, we relied on the equivalence of applying a frequency offset during acquisition and reconstruction. Unlike these techniques, however, our goal was not to reduce the effects of field inhomogeneities, but to exploit these effects to extract the geometrical center of a field perturbing object. Effectively, the distortion was even increased by applying a strong frequency offset to the whole image, instead of reducing the field distortion locally, as is aimed for when applying the distortion correction techniques [110, 111, 133, 135–137]. In the context of our study, the distortion correction techniques could be useful to reduce distortion in the on-resonance acquired image. In that case, the locations of the perturbing objects, e.g., shown in Figures 6.6-6.8, could be mapped onto an undistorted image. The correction, however, should obviously be applied after performing reconstruction co-RASOR, to ensure that sufficient signal pile-up remains available for focusing in the center of the perturbing object(s).

With regard to the limitations of the study, the following observations should be made. For simplicity of the theoretical description, data was assumed to be frequency encoded by a constant gradient. In reality, data acquisition was performed partially during gradient ramp-up. The encoding should, therefore, be described by a time-dependent gradient [110, 133, 135]. When the time dependence of the gradient is taken into account, the equations that describe the principles (Equations 6.1-6.3) become more complex [110, 133, 135]. However, it should be appreciated that the purpose of the theory section is not to exactly model off-resonance effects for various, more or less realistic, acquisition schemes, but to explain the mechanism behind co-RASOR for a simple 1D case. The important message from the theory section -illustrated by Figure 1- is that co-RASOR is able to shift signal pile-up, which is present surrounding a perturbing object, towards the center of a perturbing object by applying a frequency offset during acquisition or reconstruction. For a practical situation, with slope sampling, $T_2^\star$ decay, etc., co-RASOR may be expected to remain effective as long as the perturbing objects of interest cause signal pile-up. In other words, the amplitude and spread of the focused signal may vary, but its location will remain unaffected by the imaging imperfections. This was illustrated in Figure 6.6. The low resolution image sampled approximately 68% of the data during gradient

ramp-up, while the high resolution image sampled approximately 6% during gradient ramp-up. As the sampling of the slope is equivalent along every direction of encoding, signal pile-up was obtained surrounding the spheres in both images. Therefore, the location of the center of the spheres was the same for both acquisitions (Figure 6.6). The amplitude of the signal pile-up was approximately a factor two lower for the low resolution image. Hence, the differences for negligible and significant sampling during ramp-up appear to be minor. Note that the frequency offset also remains constant during sampling along the gradient ramp-up and that in those cases a global frequency offset can also be applied during reconstruction. The global frequency offset during reconstruction, therefore, remains effective with slope sampling.

Although acquisition co-RASOR and reconstruction co-RASOR generally showed a good agreement, some minor differences could be observed. One of those differences is a black ring surrounding the phantom for acquisition co-RASOR, which was absent for the reconstruction co-RASOR (Figure 6.3). This ring is likely caused by ringing. To appreciate this, it should be realized that by increasing the frequency offset, the object appears to increase in size due to the blurring of the signal of the voxels at the edge, as illustrated in Figure 6.1h. For a given scan matrix, the size of the object has been reported to determine the extent of polar sampling artifacts and polar reconstruction artifacts, e.g., ringing [132, 138]. As the size of the encoded object differs between acquisition co-RASOR and reconstruction co-RASOR, the ringing artifact differs too. Other small deviations can probably be ascribed to regridding artifacts, partial volume effects and noise. These may differ between acquisition co-RASOR and reconstruction co-RASOR, since acquisition co-RASOR represents different acquisitions, while the reconstructions were based on a single acquisition. Furthermore, acquisitions were reconstructed onto a rectangular grid after acquisition with a frequency offset, whereas reconstruction co-RASOR applies the frequency offset to a single acquisition that was already reconstructed onto a rectangular grid.

According to our study, reconstruction co-RASOR can be applied to homogeneous as well as heterogeneous environments, as long as the signal intensity variations in the structures surrounding the perturbing objects are smaller than the signal increase caused by the focus of their signal pile-up. Whenever the signal pile-up is smaller than the signal intensity variations already present in the on-resonance acquired image, the highest signal intensity will not correspond to the center of the field perturbing object. Furthermore, in the presence of high signal variations, the background may not

be suppressed completely, as illustrated in Figures 6.8g-i displaying spurious high signal intensities due to the fat in porcine tissue. Often, discrimination between relevant and irrelevant high signal intensities can be done visually in such situations or by increasing the signal threshold manually.

To obtain sufficient signal in the focus/center of a field perturbing object, it should show symmetry. As a consequence, co-RASOR works best for elongated and punctuate structures. The symmetry of these perturbing object determines the size, shape and intensity of the focused signal intensity. A needle shaft, for instance, shows line symmetry and, therefore, the focused signal originates mainly from a cylinder surrounding the shaft. A needle tip, on the other hand, displays point symmetry and hence the focused signal originates from approximately half a sphere surrounding the tip. Therefore, the focused signal is highest at the needle tip for each needle orientation with respect to B_0, as illustrated in Figures 6.8g-h. Fortunately, many devices used for interventional purposes are punctuate or elongated and thereby exhibit symmetry along one axis (needle, (guide)wires) or show point symmetry (brachytherapy seeds, markers). The radially symmetric signal evolution as a function of the frequency offset as, e.g., shown in Figure 6.4, reflects the symmetry of both the object and its magnetic field perturbation. Asymmetry in the amplitude and shape of the positive and negative lobes of a magnetic field offset of a dipolar magnetic field offset that is induced by a sphere [5, p.755] results in some small differences between the optimal positive frequency offset and the optimal negative frequency offset, as shown in Figure 6.4. The described differences include the value for the optimal frequency offset as well as the intensity at the optimal frequency, as is most clearly illustrated for the largest sphere in Figure 6.4.

Several scanning parameters determine the accuracy and amplitude with which the center of the field perturbing objects are denoted. The amplitude of the focused signal is determined by the optimal frequency offset. The optimal frequency offset is determined by the frequency offset and the size of the signal void induced by the field perturbing object. By applying broadbanded radiofrequency-pulses, short TEs and small voxels, under-excitation and signal dephasing were minimized. A short TE and large bandwidth result in high signal pile-up in the direct vicinity of the object. The high signal pile-up will result in high positive contrast in the center of the perturbing object after applying the optimal frequency offset. Longer TEs causes off-resonant spins that are excited by a broad bandwidth pulse to dephase before the acquisition starts. As a consequence of the short TE and broadband radiofrequency pulse applied in our experiments, the size of small ob-

jects, such as the brachytherapy seeds and the needle corresponded closely to their true size. However, as illustrated by phantom A, the technique aims at depicting the exact object center at the right location. The presented post-processing algorithm is not aimed at the correct depiction of the object size. The object size can often be easily included in the image, as it is known beforehand. The signal dephasing can also be minimized by increasing the resolution [24]. The resolution thereby determines directly (discriminative character) and indirectly (amount of signal dephasing) the accuracy of co-RASOR. Evidently, when the signal pile-up is more accurately sampled by applying a higher imaging resolution, the location of the center of the field perturbing object is more accurately defined. This was illustrated in Figure 6.6, which shows a more blurred signal pile-up for the image acquired at a lower resolution.

In our opinion, the power of co-RASOR -accurate localization of punctuate and elongated paramagnetic structures- will be most valuable in the context of interventional applications. However, 3D center-out radial acquisitions, as applied in this work, are time consuming. An acquisition of a 128^3 matrix can be performed within 2 minutes and 34 seconds. Increasing the matrix to 176^3, increased the acquisition time to 5 minutes and 39 seconds. Larger FOVs, which might be necessary for some applications, will require even longer scan durations. Furthermore, the radial acquisitions have limitations with regards to the FOV that can be used to prevent backfolding artifacts. Hence, applications that pose modest requirements with regard to temporal resolution, such as position verification of needles, robotic devices, implants, etc., will be the first that will come into reach.

The accurate localization might also be of assistance in real-time MR guided interventions. Future work will, therefore, focus on reducing acquisition times, for example by applying undersampling, stack of stars acquisitions and 2D ultrashort TE sequences [25, 134]. Using such features, acquisitions within a minute have been demonstrated to become feasible [134]. By decreasing the acquisition time even further, we expect co-RASOR acquisitions to speed up considerably, allowing accurate real-time tracking of field perturbing objects. Therefore, we believe the accurate localization of objects by co-RASOR is a valuable clinical and research tool. We furthermore expect that, by improving on some of the drawback of the current implementation, co-RASOR will become a practical tool for an increasing number of applications.

There is more to life than simply increasing its speed

M. Gandhi

CHAPTER 7

A dual plane co-RASOR technique for accurate and rapid tracking and position verification of an Ir-192 source for single fraction HDR brachytherapy

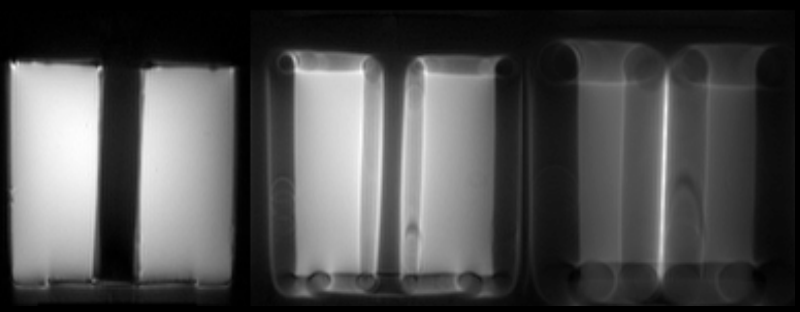

Submitted as: H. de Leeuw, M.A. Moerland, M. van Vulpen, P.R. Seevinck, and C.J.G. Bakker. A dual plane co-RASOR technique for accurate and rapid tracking and position verification of an Ir-192 source for single fraction HDR brachytherapy.

Abstract

Effective HDR brachytherapy treatment requires accurate and independent treatment verification to ensure that the treatment proceeds as prescribed, in particular if a high dose is given, as in single fraction therapy. Contrary to CT imaging and fluoroscopy, MR imaging provides high soft tissue contrast. Conventional MR techniques, however, do not offer the temporal resolution in combination with the 3D spatial resolution that is required for accurate brachytherapy source localization.

We have developed an MR imaging method (co-RASOR) that generates high positive contrast in the geometrical center of field perturbing objects, such as HDR brachytherapy sources. The co-RASOR method generates high positive contrast in the geometric center of an Ir-192 source by applying a frequency offset to center-out encoded data. To maintain the high spatial accuracy in 3D, but with adequate temporal resolution, two orthogonally placed center-out encoded 2D images are applied rather than the full 3D acquisition. Its accuracy in 3D is demonstrated by 3D MR and CT.

The 2D images show high positive contrast in the geometric center of non-radioactive Ir-192 sources, with focused signal intensities up to 160% of the average signal intensity in the surrounding medium. The accuracy by which the center of the Ir-192 source is located by the dual plane MRI acquisition corresponds closely to the accuracy obtained by 3D MRI and CT imaging. The positive contrast is shown to be obtained in homogeneous and in heterogeneous tissue.

In conclusion, the dual-plane co-RASOR method allows a brachytherapy source to be tracked in 3D, with millimeter accuracy and a temporal imaging resolution of approximately 4 seconds.

7.1 Introduction

During the past decade low-dose-rate (LDR) permanent prostate implant brachytherapy has become an accepted, effective and safe therapy for localized prostate cancer [139]. Recently, however, treatment of prostate cancer by High-Dose-Rate (HDR) brachytherapy in a single fraction is gaining interest [140–142]. As compared to the permanent implant, single fraction HDR requires just one treatment session with anesthesia, is offered on an outpatient basis, and may have advantages in terms of radiobiology and control of source positions [140, 141, 143, 144]. Currently, treatment planning is based on visualization of the needles on US, fluoroscopy, CT or MRI [140, 141]. If the treatment itself is performed under image guidance, fluoroscopy is the method of choice for position verification [145, 146]. As the prostate and tumor cannot be discriminated by fluoroscopy, the soft tissue contrast is obtained by registering previously acquired MR images to the fluoroscopy data. This method suffers from difficulties associated with the registration and inter and intra treatment changes in anatomy due to e.g. bowel movement or bladder filling [147]. In our view, a much more reliable approach to guided HDR brachytherapy would include MR imaging and MRI based intra-procedural feedback on the exact location of the source with respect to tumor and critical organs, to allow dose distribution optimization [148]. However, the difficulties associated with MR-guided brachytherapy source location verification have, to our knowledge, not been dealt with so far.

Accurate localization of a brachytherapy source requires sufficient temporal resolution and adequate spatial resolution. Unfortunately, these requirements are not easily satisfied by conventional MR imaging for several reasons. First, these devices do not generate signal themselves. Second, the devices induce magnetic field inhomogeneities, which result in signal loss and image distortion [24, 123]. Third, 3D MR imaging requires several minutes, while 3D imaging on CT and other modalities is routinely performed within seconds. To counteract these problems, many MR imaging techniques have been developed, aiming at improving the depiction of interventional devices [4, 68]. Although these methods can generate high positive contrast in the vicinity of the perturbers, they do not yet yield the desired geometric accuracy as, for instance, achieved by CT. Furthermore, their efficiency is suboptimal, as multiple acquisitions are needed to obtain the desired positive contrast image as well as anatomical information [4, 68].

Recently, center-out RAdial Sampling with Off-Resonance reconstruction (co-RASOR) has been presented, which largely solves the mis-positioning

artifact and provides high signal intensity in the magnetic center of punctuate and elongated objects [4, 149]. In the co-RASOR technique, multiple frequency offsets are applied during signal reconstruction in a center-out radial acquisition. When the frequency offset is optimally attuned to the disturbance induced by a punctuate or elongated field perturbing structure, high positive contrast is generated in the geometrical center of the structure [4, 149]. However, the 3D images, as applied in the original work, require several minutes and limit the temporal resolution of the technique.

In this *in vitro* study, we present a dual plane version of the co-RASOR technique that significantly reduces the acquisition time, while maintaining the localization accuracy. To achieve these aims two orthogonal 2D center-out radially encoded acquisitions, instead of a full 3D acquisition, are applied to track an Ir-192 source, used for single fraction HDR brachytherapy, in 3D. Experiments with homogeneous and heterogeneous tissues are performed to show the robustness and the adequate spatial and temporal resolution for clinical purposes obtained by the dual-plane method. Its geometric accuracy will be verified by CT and 3D co-RASOR.

7.2 Materials and methods

7.2.1 Rationale

Signal pile-up induced by a field perturber, such as an Ir-192 brachytherapy source, is symmetrically distributed surrounding the center of the perturber when applying a center-out readout [4, 149]. Reconstruction at the optimal frequency offset can focus the symmetric signal pile-up in the center of the perturber [149]. A 3D center-out acquisition allows the center of a perturber to be located accurately in 3D. Another option is to apply two, orthogonal, center-out encoded slabs containing the source. Each of the two slabs allows the location to be determined accurately in-plane, while the through-plane coordinate is covered by one of the in-plane coordinates of the perpendicular slab.

7.2.2 Phantom setup

An Ir-192 source used for brachytherapy consists of a core of Ir-192 encapsulated by steel, which is attached to a steel cable [150]. Two phantom setups were applied to validate the geometric accuracy of the 3D tracking of an Ir-192 source by a dual-plane co-RASOR technique.

Phantom A was developed to characterize the signal pile-up induced by the Ir-192 source attached to the steel cable and the source detached from the steel cable and to verify that the center obtained by the dual-plane technique is independent of the presence of the steel cable. The setup consisted of a container filled with distilled water doped with 26mg $MnCl_2.4H_2O$ per liter to adapt the T_1 relaxation time. In the container a small plastic platform was positioned on which two hollow plastic 6F Proguide needles (Elekta/Nucletron, Veenendaal, The Netherlands) were placed parallel to the main magnetic field. The first needle contained source 1, which consisted of a non-active Ir-192 source (Elekta/Nucletron, Veenendaal, The Netherlands) [150]. The second needle contained source 2, which was a similar non-active Ir-192 source (Elekta/Nucletron, Veenendaal, The Netherlands), but with the source itself disconnected from the cable. Initially, the steel cable of the second source was placed adjacent to the Ir-192 source. Thereafter, the steel cable was retracted in steps of approximately 10mm.

Phantom B was used to show that dual-plane co-RASOR tracking also works in heterogeneous tissue. The phantom consisted of a 4-cm-thick inhomogeneous piece of porcine tissue containing fat, connective tissue and bone. In the porcine tissue a plastic 6F Proguide needle (Elekta/Nucletron, Veenendaal, The Netherlands), containing source 1, was inserted parallel to B_0. Another needle was inserted at 57 with respect to the first needle. The source was manually retracted in 20 steps of approximately 5mm.

7.2.3 Scan techniques

MR imaging was performed on a 1.5T whole body MRI (Philips Healthcare, Best, The Netherlands), using a surface coil with two elliptical elements, with short axis 14 cm and long axis 17 cm.

The phantoms were subjected to a full 3D co-RASOR acquisition and a dual-plane co-RASOR acquisition:

1. A 3D free induction decay (FID) was acquired with a center-out radial readout. Scan parameters included: an excitation with a non-selective radiofrequency (RF) block pulse with a bandwidth of 22kHz, field of view (FOV) $224^3 mm^3$, 1mm isotropic resolution, echo time (TE) 0.34ms, repetition time (TR) 6.5ms, flip angle θ 15°, read-out bandwidth 794Hz/pixel and one signal average, resulting in a scan duration of 10min and 50s.

2. A dynamic, dual-plane interleaved center-out 2D acquisition, consisting of a coronal and a sagittal slice. The coronal scan was planned to contain both needles. The sagittal slice was planned through the needle containing the Ir-192 source that was manipulated. Scan parameters included excitation by a sinc-gauss RF pulse with a bandwidth of 4.1kHz, FOV 224^2mm^2, slice thickness 5mm, 1mm isotropic resolution, TE 1.04ms, TR 9.7ms, θ 15°, read-out bandwidth 891Hz/pixel and one signal average, resulting in a scan duration of 4.7s per dynamic.

The 3D scan performed on Phantom B applied the same parameters, except for the FOV (176^3mm^3) and TR (5.0ms), resulting in a scan duration of 5min and 12s. Similarly, the dual-plane scan employed a different FOV (176^2mm^2), TE (0.82ms) and TR (8.3ms), resulting in a scan duration of 3.2 s per dynamic.

To demonstrate that co-RASOR accurately depicts the location of the center of the Ir-192 source, CT images were acquired in addition to the MR acquisitions. CT images were acquired on a 64-slice CT scanner (64-slice Brilliance, Philips Healthcare, Best, The Netherlands) with the following parameters: voltage 120kV, mAs 263, in-plane resolution 0.45 m, increment 1mm.

7.2.4 Postprocessing

Postprocessing was performed using Matlab (The MathWorks, Natick, MA). 3D and 2D dual plane images were processed as described elsewhere [149]. Thirty reconstructions with off-resonance frequencies from 0 to 7.5kHz, with a frequency stepsize of 250Hz were applied to the 3D and 2D data. The optimal frequency offset for the 3D data was determined automatically [149]. The optimal frequency offset for the 2D images was selected manually to correspond to the highest signal intensity in an area in the image broadly covering the position of the Ir-192 source. The positive contrast was created by subtracting the on-resonance image from the image reconstructed with the optimal frequency offset and thresholding [149]. 2D reconstructions and postprocessing were completed within one second.

To evaluate the geometric accuracy, co-RASOR images were registered to CT by rigid registration using elastix [88]. Maximum intensity projections (MIPs) of the 3D data were constructed for visualization purposes, for both the CT images and co-RASOR images. An image displaying the positive contrast, anatomical reference and the signal void caused by the sources,

was obtained by overlaying the co-RASOR MIP on a minimum intensity projection of the corresponding slices of the original, on-resonance, MR image.

7.3 Results

7.3.1 Localization of the Ir-192 source with CT and MRI

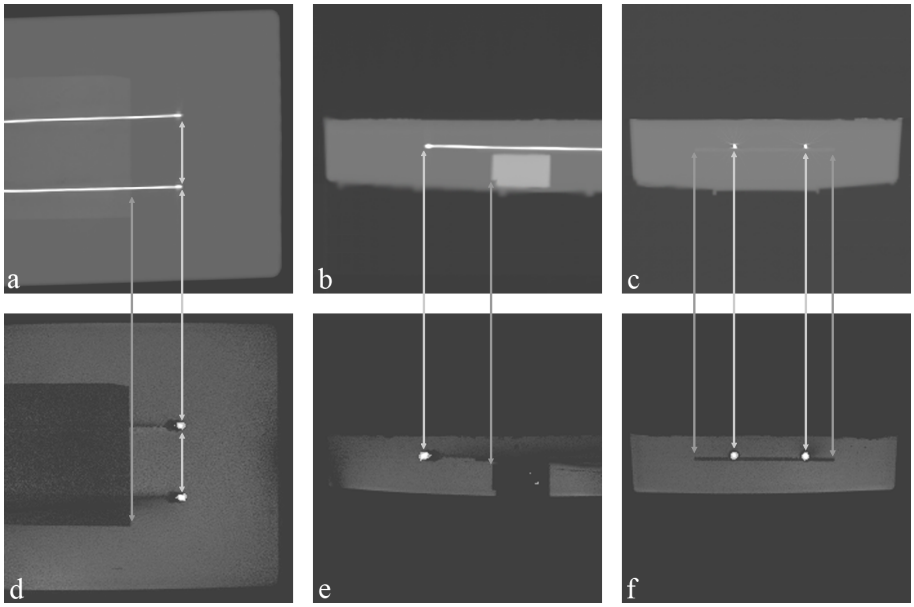

Figure 7.1: The top row shows the MIPs of the CT images of slices containing the Ir-192 sources. MIPs of the 3D positive contrast co-RASOR images added to minimum intensity projections of the magnitude images of phantom A are shown on the bottom row. The dark gray line indicates the location of the plastic platform on the CT and co-RASOR images. The light gray arrows point at the location of the tip of the Ir-192 source on the co-RASOR MRI image and the CT image.

The 3D images showed focused signal intensity at the tip of the sources of approximately 500% of the average signal intensity in the medium. To verify that the focused signal intensity in the 3D co-RASOR image depicted

the location of the sources, the CT images were registered to the MR images, as shown in Figure 7.1. The dark gray lines in Figure 7.1 indicate that the location of the platform is the same in both images. After registration, the CT image and co-RASOR image depicted the same location for both tips. The optimal frequency offset used for the positive contrast co-RASOR image was 5kHz.

To validate the initial source locations found on the dual plane co-RASOR images, the source locations were determined on the 3D images with respect to the scanner isocenter and used as reference. The location in millimeters with respect to the scanner isocenter, with x from right to left, y the location along the anterior-posterior direction and z along the feet-head direction, of source 1 was (-37,70,44), while source 2 was located at (20,70,44).

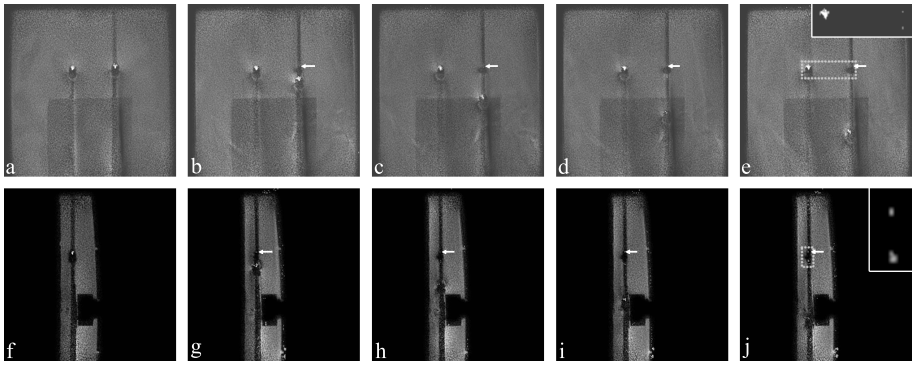

Figure 7.2: Two 2D slices through the second Ir-192 source in phantom A. Shown are a number of dynamic acquisitions, while the steel cable is retracted (step size 20mm). The top row (a-f) shows coronal slices and the bottom row (g-l) sagittal slices. When the steel cable is adjacent to the Ir-192 source, the tip is characterized by a signal pile-up at an optimal frequency offset of 5kHz. This frequency offset remains the optimal frequency offset for locating the tip of the cable after it is retracted from the source. The source itself gives a much smaller artifact (white arrows) at an optimal frequency offset of 2.25kHz (coronal) and 3.5 kHz (sagittal). This signal pile-up is low and best observed in the positive contrast image, which are shown for the area indicated by the white dotted lines in the inserts. The positive contrast image at 2.25/3.5kHz results in a widening of the signal pile-up at the tip of the cable and at the tip of source 2.

During the experiment, the optimal frequency needed for the depiction of the center of source 2 changed, after retracting the steel cable. The optimal frequency shifted from 5kHz to 2.25 and 3.5kHz, for the coronal and sagittal slice respectively. The tip of source 1 and the steel cable, however, remained optimally depicted at the frequency offset of 5kHz. The two optimal frequency offsets resulted in blurring surrounding the sources in the positive contrast images. The location extracted from the dual-plane images for source 1 was (-37,-,43) in the coronal plane, source 2 was located at (19,−,44)x(−,70,44), for the coronal and sagittal slice, respectively. This implies that the locations agreed to within 1mm with the location on the 3D and the CT image, which is within the error margin [149].

After retraction of the steel cable, the tip of the source showed the highest signal intensity at (19,−,45) and (−,70,45). This position was the same on a 3D co-RASOR image acquired after the retraction of the cable. The signal maximum was approximately 140% of the average signal intensity. The change of position of the hyperintensities in between dynamics was on average 21mm, per 2 dynamics.

7.3.2 Ex vivo tracking of Ir-192 source

To test the applicability of the dual plane co-RASOR technique in heterogeneous tissue samples, similar experiments were performed on phantom B. Again, the CT images and co-RASOR images depicted the same location for the Ir-192 source, after registration. To verify that the correct position is extracted from the dual-plane co-RASOR image, the location of the tip of the non-radioactive Ir-192 source was determined with respect to the scanner isocenter: (−58;19;49). The results of the dynamic acquisitions are shown in Figure 7.3.

Initially, the position of the Ir-192 source agreed to 1 mm with the position on the CT image: (-;19;51) and (−59;-;50) for the coronal and sagittal image, respectively. Differences are caused by different off-centers used for the scans and the uncertainty associated with the co-RASOR method [149]. Distances, in steps of four subsequent dynamic acquisitions, are on average 20.5mm, with the minimum distance 18mm and the maximum distance 23mm. The coordinate along z in both 2D images agreed to within 1mm.

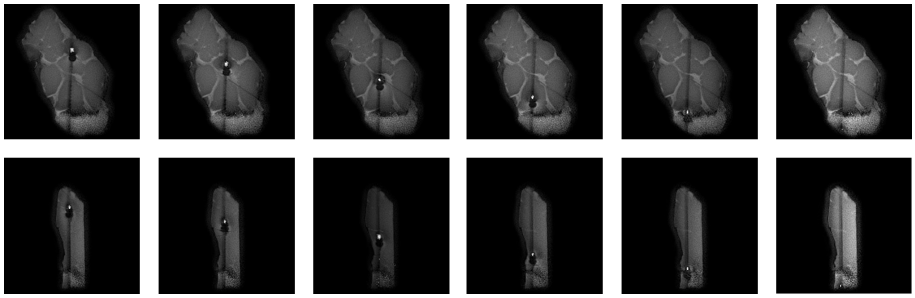

Figure 7.3: Coronal and sagittal slice displaying a sum of the positive contrast co-RASOR image and the on-resonance acquired image. Shown are the results after retracting the source approximately 0, 2, 4, 6, 8 and 10cm.

7.4 Discussion

7.4.1 Summary

In this work we have shown fast and accurate 3D tracking of an HDR brachytherapy source by applying a dual plane co-RASOR scanning technique. The two orthogonal 2D slices allowed the Ir-192 source to be tracked in 3D, maintaining localization accuracy, while reducing scan time. The method was shown to provide an accuracy comparable to CT and to be capable of tracking the device in approximately 4s, which is considered appropriate for the intended application. The technique was shown to be effective in homogeneous tissue as well as in heterogeneous tissue. Furthermore, multiple sources could be located accurately from a single acquisition.

7.4.2 Characteristics of the dual plane technique

Accuracy

We have shown the ability to locate the centers of Ir-192 sources with millimeter accuracy. The main determinant of the accuracy is the imaging resolution. Previously, we have shown that the accuracy can be enhanced by increasing the resolution. This can be accomplished by increasing the scan matrix or artificially by zero filling [149]. The obtained locations represented the location with respect to the isocenter of the scanner bore and therefore can easily be extrapolated to world coordinates. Furthermore, the distances between the tip at subsequent dynamics agreed well with the intended step

size of the retraction. The small differences are likely to be caused by the uncertainty of the co-RASOR localization and may be induced by the manual retraction of the source or source-cable. The location of the center of the tip of the brachytherapy source differed between the 3D and dual-plane co-RASOR. These were, amongst others, caused by the difference in the center of the scan plane, which induced rounding errors.

Determinants of the optimal frequency offset

The value of the optimal frequency offset in co-RASOR is determined by the (size of the signal void induced by) magnetic field of the field perturber. The whole device, that is the source including the steel cable, is responsible for the signal void and, thereby, for the induced signal pile-up. The source including the steel cable gives a high signal pile-up even in noisy areas, see e.g. bottom right image Figure 7.3. The artifact of the Ir-192 source without the cable is smaller, as shown in Figure 7.2. The smaller artifact results in less signal to be focused in the center of the source and therefore its center is more difficult to locate. Especially for the small artifacts, the source should be contained within the 2D slices, since the presence of the source determines the symmetry of the imaged artifact.

For the source to be located accurately, signal should be present surrounding the source. Otherwise localization is more difficult, as shown in Figure 7.2j from which the location of the device could not be obtained. Furthermore, a perturbing device is more difficult to localize accurately in areas with a lower SNR. The inter-leaved scanning method resulted in a band with a reduced steady state signal at their overlap, which makes the localization more difficult especially small field perturbing structures. Larger applicators, as for example used for brachytherapy at the cervix or esophagus, might perturb the magnetic field themselves or result in a large signal void surrounding the brachytherapy source. Future research is needed to study the applicability of co-RASOR in such situations.

7.4.3 Literature

When placing our results against literature findings, the following observations can be made. Over the years many tracking methods have been developed, which can principally be divided into two categories, namely active tracking and passive tracking methods [151, 152]. Active tracking methods are considered more complex, since they require modification of the stu-

died object by applying micro coils, self-resonant radio frequency circuits or electrified wire loops [152]. The brachytherapy source does not easily allow such a modification and therefore passive tracking is more suited to tracking it. Generally, however, passive tracking turns out to be slower than active tracking [152]. The tracking as applied in this work has been designed to provide as high an accuracy as possible within approximately 4 seconds, which corresponds to relevant source dwell times used in HDR brachytherapy. The tracking can be speeded up by applying methods used to speed up active tracking methods, such as parallel imaging techniques, e.g., SENSE, sparse imaging or using a lower imaging resolution [151].

7.4.4 Future prospects

The coordinates extracted from the co-RASOR acquisition might allow the scan plane to be updated automatically in sequential acquisitions, as used in active tracking methods [152]. By centering a subsequent dual plane acquisition on the coordinate located on the previous acquisition, the subsequent dual plane acquisition is more likely to enclose the brachytherapy source. Future research will focus on motion compensation and decreasing the acquisition time further [153].

7.4.5 Conclusion

In conclusion, we have shown a dual-plane 3D localization technique for tracking of an Ir-192 brachytherapy source with millimeter accuracy in approximately 4 seconds.

Start with what is right rather
than what is acceptable

P. F. Drucker

CHAPTER 8

On the utility of spectroscopic imaging as a tool for generating geometrically accurate MR images and parameter maps in the presence of field inhomogeneities and chemical shift effects

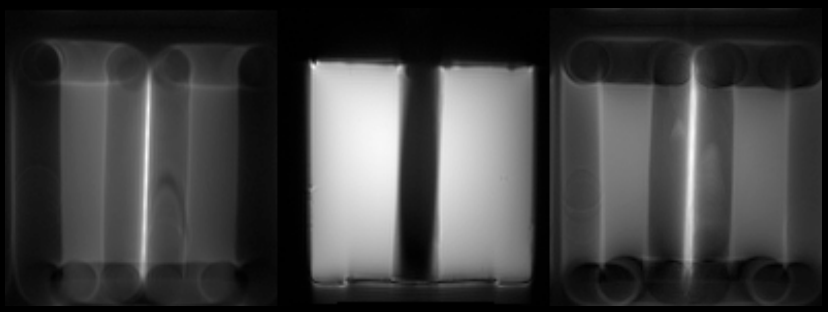

Accepted for publication as: C.J.G. Bakker, H. de Leeuw, G.H. van de Maat, J.S. van Gorp, J.G. Bouwman, and P.R. Seevinck. On the utility of spectroscopic imaging as a tool for generating geometrically accurate MR images and parameter maps in the presence of field inhomogeneities and chemical shift effects. *Magnetic Resonance Imaging*

Abstract

Lack of spatial accuracy is a well recognized problem in magnetic resonance imaging, which severely detracts from its value as a stand-alone modality for applications that put high demands on geometric fidelity, such as radiotherapy treatment planning and stereotactic neurosurgery. In this paper we illustrate the potential and discuss the limitations of spectroscopic imaging as a tool for generating purely phase encoded MR images and parameter maps that preserve the geometry of an object and allow localization of object features in world coordinates.

Experiments were done on a clinical MR imaging system with standard facilities for imaging and spectroscopy. Images were acquired with a regular spin echo sequence and a corresponding spectroscopic imaging sequence. In the latter, successive samples of the acquired echo data were used for the reconstruction of a series of evenly spaced images in the time and frequency domain. Experiments were performed on a spatial linearity phantom and a series of test objects representing a wide range of susceptibility and chemical shift induced off-resonance conditions.

Contrary to regular spin echo imaging, spectroscopic imaging was shown to be immune to off-resonance effects, such as caused by susceptibility, field inhomogeneity, chemical shift, f_0-offset, and field drift, and thereby to yield geometrically accurate images and parameter maps, which allowed object structures to be localized in world coordinates.

From these illustrative examples and a discussion of the limitations of purely phase encoded imaging methods it is concluded that spectroscopic imaging offers a fundamental solution to the geometric deficiencies of MRI which may evolve toward a practical solution when the full advantage of the current developments with regard to scan time reduction is put to use. This perspective is backed up by a demonstration of the significant reduction of the scan time that may be achieved by the use of compressed sensing for a simple phantom.

8.1 Introduction

Lack of spatial accuracy is a recognized problem in magnetic resonance imaging. In standard MR scans, the problem displays itself in two ways: first, the images do not faithfully represent the geometry of the object under investigation, especially in the presence of implants, internal and external devices, surgical tools, localization frames, etc.; second, the images do not exactly reveal the position of the object with respect to the world outside ('the laboratory'), i.e., uncertainty arises when trying to convert image coordinates to laboratory coordinates. This uncertainty diminishes the accuracy by which a certain volume of interest within the image (a 'target') can be localized in physical space, for example with respect to the tabletop of the scanner. Both geometric deficiencies have a detrimental effect on the value of MRI as a stand-alone modality for applications that put high demands on geometric fidelity, such as radiotherapy treatment planning, stereotactic neurosurgery, stereotactic laser and radiosurgery, and image-guided interventions, e.g., needle biopsies.

According to the vast literature on the subject (see, e.g., [2] and references therein), the lack of geometric accuracy in MRI is mainly caused by the nonlinearity of the imaging gradients and by off-resonance effects. The first factor, nonlinearity of the gradients, is largely a matter of system and sequence design and virtually independent of the object. It is optionally corrected for on most clinical MR systems and, therefore, not considered an issue here [154]. With regard to the second factor, off-resonance effects, several sources can be identified, including system related field inhomogeneities and instabilities, susceptibility induced field inhomogeneities, chemical shift related frequency offsets, and an overall frequency offset associated with the choice of a particular reference frequency, f_0. Usually, this f_0 is inferred from the frequency distribution in the part of the object to be imaged. The resultant f_0 is used to define the origin of image space along the slice selection and readout axes, but does not refer to a specific or exactly known location in physical space. As a consequence, the origin of image space will exhibit a usually small but unknown shift with respect to the origin of the laboratory frame in the slice selection and readout directions. Additional shifts may occur when the static magnetic field exhibits temporal variations, for example due to resistive heating of magnet structures [155]. Such shifts will be particularly harmful when scanning in the dynamic mode, as is typically done during diagnostic and therapeutic interventions.

An obvious way to deal with the geometric deficiencies associated with

MRI is the application of very strong slice selection and readout gradients. Since distortions are generally inversely proportional to the strengths of the gradients [5], this approach is effective in many cases. Yet, strong gradients do not provide the final solution for several reasons. First, strong slice selection and readout gradients go together with large excitation and readout bandwidths and, hence, large RF power depositions and low SNR images. Second, rapidly switching strong gradients produces noise and may cause peripheral nerve stimulation [156]. Besides, it induces short-term and long-term eddy currents, which act as sources of field inhomogeneities themselves and are often hard to compensate for. Third, gradient capabilities on clinical systems are usually not sufficient to overcome off-resonance effects at higher field strengths or invoked by large inhomogeneities such as associated with metallic devices, implants, needles, etc. At 7T, for instance, a readout gradient of 30 mT/m would already be required to keep distortions associated with air cavities ($\Delta\chi \approx 10$ ppm) within 1mm.

A more conclusive and fundamental solution to the indicated geometric problems would be to refrain from frequency encoding altogether and rely on phase encoding instead. In effect, this is exactly what is done in spectroscopic imaging, albeit with a different purpose in mind [157, 158]. In standard proton spectroscopic imaging (SI), for instance, the signals from water and fat are suppressed in order to enable visualization and analysis of low-concentration tissue metabolites like NAA, creatine and lactate. The signal from these metabolites is several orders of magnitude smaller than from water, so to go from tissue chemistry to structural imaging is a matter of leaving out the suppression techniques and an adaptation of the processing and display facilities. With suppression switched off, the acquired, purely phase encoded images will be completely dominated by the properties of the bulk water and fat protons and by line broadening and $T_2^\star$ effects from microscopic and macroscopic field inhomogeneities. As only one phase encoding step is applied after each excitation and prior to collection of a free induction decay (FID) or spin echo (SE) signal, each acquired data point in k-space will exhibit the same influence of dipolar interactions, chemical shifts, field inhomogeneities, diffusion, and other mechanisms. The resultant images, one $T_2^\star$-weighted complex image for each sample point, will, therefore, not be distorted by off-resonance effects, irrespective of the strength of the applied gradients. Evidently, this will also be the case for the frequency resolved images and the parameter maps, e.g., $T_2^\star$-maps and ΔB_0-maps, that may be derived from the acquired data.

To date, this non-standard use of spectroscopic imaging - i.e., for obtai-

ning geometrically accurate images of water as well as of fat protons rather than biochemical information - has not aroused much interest in the medical community, since the lengthy examination times associated with purely phase encoded imaging techniques have always been considered prohibitive. Recent developments with regard to scan time reduction such as parallel imaging and compressed sensing, however, make us believe that this barrier may not be as impregnable as might have seemed in the past. We, therefore, thought it a timely exercise to start and promote interest in this non-standard use of spectroscopic imaging by demonstrating its utility in generating time and frequency domain resolved images and parameter maps that (a) correctly depict the geometry of an object and (b) allow localization of object features in laboratory/world coordinates. By way of experiments with a spatial linearity phantom and various configurations of test tubes, spectroscopic imaging will be shown to yield images and parameter maps that are geometrically immune to off-resonance effects, such as caused by field inhomogeneity, susceptibility, chemical shift, f_0-offset, and field drift. Once we have demonstrated the potential of spectroscopic imaging in providing a fundamental solution to the geometric deficiencies of MRI, we will discuss how this solution may evolve towards a practical solution when full advantage will be taken of current developments with regard to scan time reduction. To back up this perspective, we will demonstrate the significant scan time reduction that may be achieved by the use of compressed sensing for a simple phantom.

8.2 Theory

In a 1D spin echo experiment with frequency encoding along the x axis (Figure 8.1, top), the p-th sample of the acquired signal can be written as:

$$s(p\Delta k) \propto \int \rho(x) exp[-\frac{\mathrm{TE} + p\tau}{T_2(x)}] e^{-i\gamma \Delta B(x) p\tau} exp[-i2\pi p \Delta k_x (x + \frac{\Delta B(x)}{G_r})] dx \quad (8.1)$$

with $-N_x/2 \leq p < N_x/2$, N_x the number of samples, ρ(x) the effective 1D spin density, incorporating T_1 and many other factors, G_r the amplitude of the applied readout gradient, $\delta k_x = \gamma G_r \tau$ the step-size in k-space, and $\Delta B(x) = B(x) - B_0$ the spatially dependent deviations from B_0 such as caused by field inhomogeneities, susceptibility deviations, chemical shifts, and f_0-shifts. The first and second exponential in Equation 8.1 describe the signal variations, as a function of p, due to $T_2^\star$ decay during data sampling. Al-

though often ignored, such variations cause blurring and impose a limit to the resolution that can be achieved in an experiment [5]. The third exponential in Equation 8.1 describes the distortion that is effected by field inhomogeneities. Utilizing the Fourier shift theorem, i.e., s(k)exp(-i2π ka)= FT[ρ(x-a)], it readily follows from Equation 8.1 that the reconstructed spin density distribution will be geometrically distorted according to:

$$\rho(x') = \rho\left(x - \frac{\Delta B(x)}{G_r}\right) \tag{8.2}$$

With regard to the static field B_0 and, hence, the deviations ΔB, it should be realized that, in the context of a particular imaging experiment, B_0 is no measured quantity but is defined in terms of the resonance frequency via $B_0 \equiv f_0/\gamma$. The resonance frequency f_0 is usually derived from the frequency distribution within the part of the object to be imaged. This f_0 serves as a reference in image space but is not related to a specific position in object space. As a consequence, an f_0-related, small but unknown, shift may occur between the origins of the coordinate systems in image space and physical space (the laboratory) in the frequency encoding direction(s).

In a 1D spectroscopic imaging experiment with spin echo detection, the p-th sample of the acquired k-space data for each point t=TE+mδt of the spin echo (Figure 8.1, bottom) can be written as:

$$s(p\Delta k) \propto \int \rho(x) exp\left[-\frac{\mathrm{TE} + m\delta t}{T_2(x)}\right] e^{-i\gamma\Delta B(x) m\delta t} exp[-i2\pi p\Delta k_x x]dx \tag{8.3}$$

with -$N_x/2 \leq p < N_x/2$, N_x the number of samples, ΔG_p the step-size of the phase encoding gradient, t_p the duration of the phase encoding gradient, and $\Delta k_x = \gamma G_p t_p$ the step-size in k-space. Equation 8.3 shows that, by applying only one phase encoding step per excitation, the s(pΔk_x) for each point t=TE+mδt of the spin echo will be equally affected by off-resonance effects. An undistorted image can thus be reconstructed for each individual sample point t=TE+mδt of the spin echo and blurring will be negligible when the dwell time δt is chosen sufficiently short. For each individual image the influence of dipolar interactions, chemical shifts, field inhomogeneities, diffusion, and other mechanisms is constant, but the influence may vary among the images. Off-resonance effects may thus be exploited as a contrast mechanism, without introducing geometric distortion and blurring.

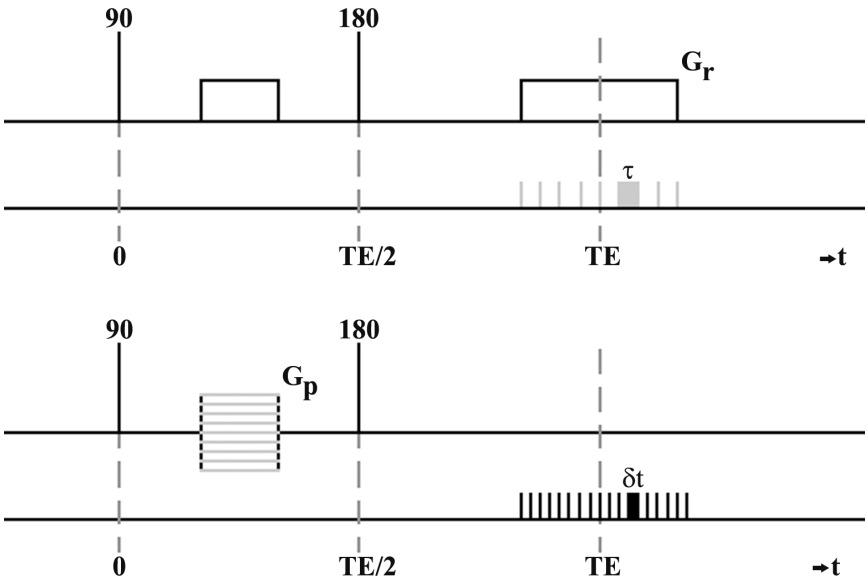

Figure 8.1: Pulse sequence diagram of, respectively, a 1D SE experiment with a frequency encoding gradient G_r (top) and a 1D SE spectroscopic imaging experiment with a stepped phase encoding gradient G_p (bottom). In the spectroscopic imaging experiment, a series of N_s images is obtained by reconstructing a separate image for each sample point t=TE+mδt of the spin echo, with $N_s/2 \leq m < N_s/2$ and N_s the number of samples.

8.3 Materials and methods

8.3.1 Phantoms

To illustrate the capabilities of the purely phase-encoded spectroscopic imaging sequences, we used a spatial linearity phantom and various configurations of cylinders and test tubes. The spatial linearity phantom consisted of a regular grid of 23×23 square holes of 9 by 9 mm, with a depth of 20 mm and a spacing of 1 mm drilled in an acrylic plate with a thickness of 2.5 cm (Promis Electro Optics BV, Eindhoven, The Netherlands). In the reported ex-

periments, only the central 5×5 elements of the grid were filled with an MR visible fluid, viz. manganese doped water with a T_1 of about 750 ms and a T_2 of about 80 ms at 1.5 T. The second phantom setup featured various configurations of cylinders and NMR test tubes with their longitudinal axes perpendicular to the tabletop and B_0. The first configuration (Figure 8.3, columns 1 and 2) consisted of a single cylinder with a diameter of 2.25 cm and a height of 10 cm and was filled with manganese doped water. In the second configuration (Figure 8.3, column 3), a 1-cm diameter test tube with sunflower oil was placed inside and parallel to the outer cylinder, so as to create a chemical shift difference. In the third configuration (Figure 8.3, column 4), oil was replaced by air to create a susceptibility difference of about 9 ppm. In the fourth configuration (Figure 8.5, column 1), fourteen 5-mm diameter test tubes with air were placed inside the cylinder to create multiple inhomogeneities at the scale of a voxel. In the fifth configuration (Figure 8.5, column 2), a 1-cm diameter test tube with doped water was placed outside the cylinder to create an external source of field disturbances. In the sixth configuration (Figure 8.6), a 1.8-mm titanium needle was placed in a 2.25-cm diameter test tube with doped water. The needle was oriented perpendicular to B_0 so as to create local field disturbances between -90 and +90 ppm.

8.3.2 Scan techniques

All imaging was done on a 1.5T clinical whole body system (Achieva 1.5T, Philips Healthcare, The Netherlands) using an 11-cm diameter, two-element flexible phased array coil for signal reception. Prior to the experiments, shim settings were determined for the homogeneous cylinder phantom (Figure 8.3, column 1) and maintained during further experimentation. Single-slice coronal images were obtained with a standard spin echo sequence (Figure 8.1, top) and a corresponding non-water-suppressed spectroscopic imaging sequence (Figure 8.1, bottom). In the spectroscopic imaging experiment, the spin echo signal was sampled at 128 equally spaced intervals of 125 μs, corresponding to a bandwidth of 8000 Hz. Note that a dwell time of 125 μs was considered to be adequate for the objects in our study but that the dwell time can readily be shortened, without technical impediment but at the cost of increased image noise, when $T_2^\star$ losses during the dwell time would become a problem. Examination parameters included an excitation bandwidth of 4 kHz, an echo time (TE) of 30 ms, a repetition time (TR) of 150ms, a flip angle of 90°, a scan matrix of 64×64, a field-of-view of 32×32 mm^2 or 64×64 mm^2, a reconstruction matrix of 64×64 or 128×128, a slice thickness of 10 mm,

two signal averages in SE, and one signal average in spectroscopic imaging, resulting in a scan duration of 20.4 seconds for the standard SE sequence and a scan duration of 10 minutes and 14 seconds for the SI sequence. In the standard SE sequence, the readout was along the left-right axis with a readout bandwidth of 50 Hz per pixel. The same gradient power was used for phase and frequency encoding in SE and phase encoding in SI (G_r=G_p in Figure 8.1). In the needle experiments, SE images were also acquired with an increased bandwidth of 500 Hz per pixel and 64 signal averages, yielding a scan time of 10 minutes and 14 seconds. Prior to further analysis, images were corrected for nonlinearities of the imaging gradients by the scanner software. The phantom setup, slice thickness and excitation bandwidth were such that the effects of an f_0 shift on the selected slice could be ignored.

8.3.3 Processing and display

Following on the spectroscopic imaging experiment, a complex image was reconstructed for each sample t=TE+mδt of the spin echo, with sampling δt=0.125 ms and -64$\leq$m$<$64, yielding a time resolved series of 128 complex images, which were converted to magnitude and phase maps for further analysis. Field maps were subsequently calculated by averaging across ten consecutive phase images acquired between t=TE (m=0) and t=TE+1.25 ms (m=10). A frequency resolved series of images was obtained by a 1D Fourier transform of the time resolved images along the time axis. This yielded 128 complex images with f=mδf, -64$\leq$m$<$64 and δf=1/(128δt)=62.5 Hz, covering the total spectroscopic bandwidth of 1/δt=8000 Hz. Magnitude averaging was applied when a lower temporal or spectral resolution was desired than the resolution at which the data was acquired, e.g., for display purposes.

8.3.4 Positioning of the object

To position the object, first the tabletop was moved out of the magnet and locked into the parking position. Next, the light visor system was used to project laser crosshairs onto the object indicating, respectively, a sagittal reference plane through the isocenter of the magnet and a transverse reference plane at a distance of 80.5 cm from the isocenter. The coronal reference plane through the isocenter was not indicated by the laser system but was verified to be located at a height of 12.0 cm above the tabletop. The object was positioned with respect to these reference planes and secured to the tabletop using the appropriate immobilization tools. Finally, the travel-to-

isocenter function was activated to move the transverse reference plane to the isocenter of the magnet and to complete positioning of the object with respect to the laboratory frame. The tabletop accuracy, as specified by the manufacturer, was 0.5 mm.

8.3.5 Determination of the resonance frequency

In preparation of each imaging experiment, the resonance frequency f_0 was determined with the object in place and using the f_0 of the previous scan as the reference for selection and readout. This was done by acquiring a volume selective spectrum of a $100\times100\times50$ mm box centered at the slice to be imaged using a PRESS sequence with a TE of 100 ms. The f_0 sequence was always preceded by a STIR sequence to null the fat signal. The center of gravity of the resultant power spectrum was taken as the frequency offset for updating f_0. In case of shimming, the f_0 determination was repeated after shimming. In some experiments, the f_0 sequence was skipped and f_0 was left unaltered or specified by the user.

8.4 Results

To demonstrate the different geometric responses of SE and SI to field inhomogeneity, in this case invoked by the shape, orientation and composition of the object, the spatial linearity phantom was subjected to a SE and a SI acquisition with equal gradient power for phase and frequency encoding. Prior to being imaged, the central 5×5 elements of the grid were brought to the isocenter and aligned with the principal axes of the gradient system using the laser positioning device. Slice selection effects were avoided by exciting a nominal slice of 10 cm, well beyond the 2.5 cm thickness of the phantom. The results of the SE and SI acquisitions are displayed in Figure 8.2 and give rise to the following observations. First, standard SE images show correct alignment in the phase encoding direction and exhibit distortions in the read direction (Figure 8.2, left). Second, the alignment is perfect in both phase encoding directions in the SI images (Figure 8.2, right). Third, the standard SE image exhibits a small f_0-shift along the read axis, which is associated with the determination of f_0, and which is absent in the SI image.

To demonstrate the utility of SI in eliminating geometric distortion due to off-resonance effects, various arrangements of test tubes were subjected to a standard SE acquisition and a corresponding spectroscopic imaging acqui-

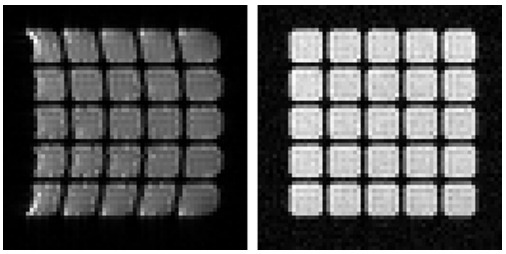

Figure 8.2: Images of the grid phantom positioned in the origin of the laboratory frame. The left panel displays the regular spin echo image with readout along the left-right axis (BW 50 Hz per pixel), the right panel the corresponding SI image (m=0, t=TE).

sition, the latter yielding 128 images with different t=TE+mδt. In all experiments, the center of the larger cylinder was always positioned in the origin of laboratory frame. The results are displayed in Figure 8.3 and lead to the following observations. First, both SE and SI yield geometrically reliable images in the absence of field inhomogeneities (Figure 8.3, column 1). Second, a shift of the resonance frequency causes a translation of the SE image along the readout axis, but leaves the SI images unaffected (Figure 8.3, column 2). In this case, f_0 was manually increased by 800 Hz. Third, chemical shift leads to misregistration along the readout axis in SE but is absent in SI images (Figure 8.3, column 3). Fourth, susceptibility deviations give rise to geometric distortions along the readout axis in SE and are absent in SI images (Figure 8.3, column 4). Overall, we observed correct alignment of SI images in all cases, correct alignment of SE images in the phase encoding direction, and susceptibility distortions, chemical shift and f_0-shift along the read direction in SE.

Next, the coaxial cylinder phantom (Figure 8.3, column 4) was used to demonstrate the utility of non-water-suppressed proton spectroscopic imaging in providing detailed information with regard to the distribution of microscopic and macroscopic field inhomogeneities within an object. For this purpose, the acquired time resolved images of the phantom, some of which are displayed in the top row of Figure 8.4, were 1D Fourier transformed to a set of frequency resolved images, some of which are displayed in the bottom row of Figure 8.4. The time and frequency resolved images respectively reflect the evolution of time signal and the frequency content of each voxel, as is illustrated for a few voxels by the diagrams in Figures 8.4d and 8.4h. The sinc modulation of the echoes in Figure 8.4d is indicative for the presence of macroscopic field gradients and points to the invalidity of a uni-exponential model in analyzing such data.

Time and frequency resolved images constitute an ideal starting point

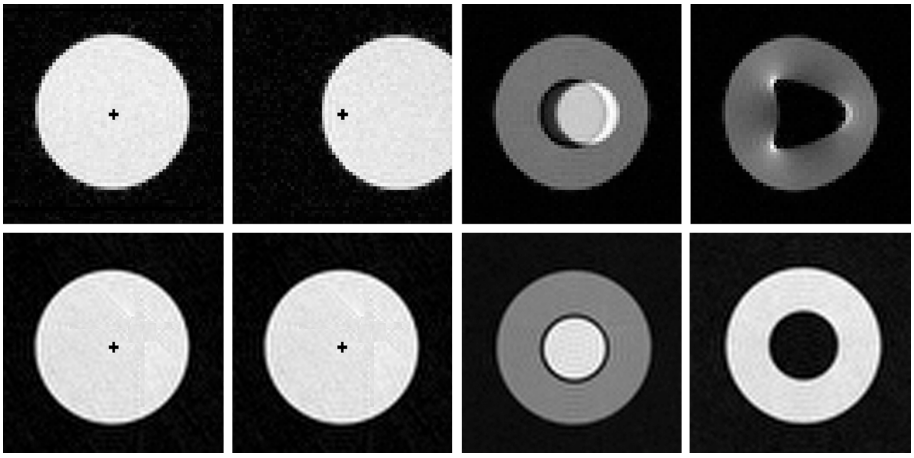

Figure 8.3: Coronal spin echo images (top row) and corresponding averaged spectroscopic images (bottom row) of a 2.25-cm diameter cylinder with doped water (columns 1 and 2) and the same cylinder with, respectively, a 10-mm diameter test tube with oil (column 3), and a 10-mm test tube with air (column 4). In the spin echo images (top row), the readout was always along the left-right axis. Black crosses in the left four images represent the origin of the laboratory frame.

for detailed studies of field inhomogeneity effects and off-resonance phenomena and for the derivation of various kinds of undistorted parameter maps and composite images. This was demonstrated by experiments with a cylinder with multiple susceptibility deviations (Figure 8.5, left column) and a cylinder in the presence of an external field disturbance (Figure 8.5, right column). In both cases, spectroscopic imaging yielded 128 SI images with different t=TE+mδt, resulting in a set of undistorted magnitude images with systematically varying $T_2^\star$-weighting and a set of undistorted phase maps describing the temporal evolution of the phase on either side of the spin echo top. As illustrated by Figure 8.5, such data sets can, for instance, be used for generating undistorted field maps.

Finally, the needle phantom was used for a comparative evaluation of conventional SE and spectroscopic imaging in the presence of larger field disturbances than commonly encountered in the human body. Figure 8.6 shows the severely distorted conventional spin echo image that results after applying a small readout bandwith (Figure 8.6a). The distortion is stron-

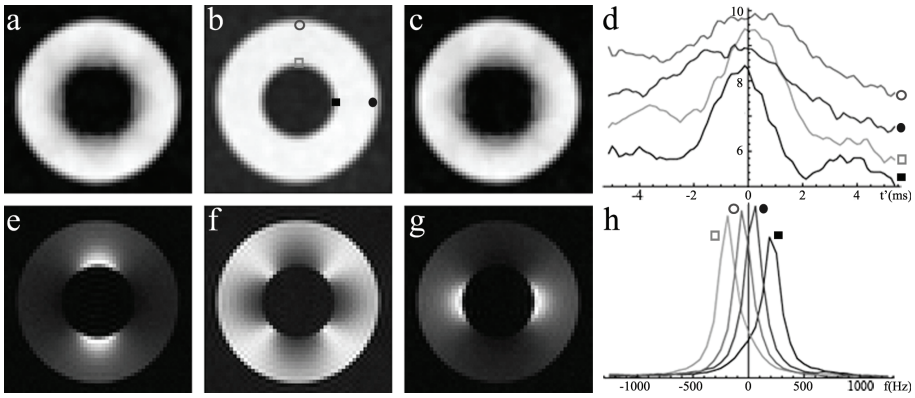

Figure 8.4: Coronal time resolved (top row) and frequency resolved (bottom row) spectroscopic images of a 2.25-cm diameter cylinder with doped water and a 10-mm coaxial test tube with air. Top row: t=TE+mδt with m=-64 (a), m=0 (b), and m=+63 (c). Bottom row: f=mδf with m=-1 (e), m=0 (f), and m=+1 (g). Herein δt=0.125ms, N=128, and δf =1/(Nδt)=62.5Hz. Graphs d and h, respectively, represent the time and frequency resolved signals for voxels at the locations indicated by the symbols in graph b.

gly reduced when using a much larger bandwidth, albeit at the expense of SNR, which is inversely proportional to the bandwidth (Figure 8.6b). When the number of signal averages is increased, so as to make the scan time of the conventional acquisition equal to the scan time of the spectroscopic acquisition, the SNR of the former and the latter are about equal (Figure 8.6c versus Figure 8.6d).

8.5 Discussion

In this work, proton spectroscopic imaging was deployed as a tool for investigating object structure and object-induced field distortions rather than tissue chemistry. This was achieved by leaving out the water and fat suppression techniques - so as to make image contrast governed by the properties of the bulk water and fat protons - and by adapting the processing and display capabilities of an otherwise standard spectroscopic imaging package. By way of phantom experiments, non-water-suppressed proton spectroscopic imaging was shown (a) to yield geometrically accurate time and frequency resolved images, (b) to enable localization of object structures in laboratory

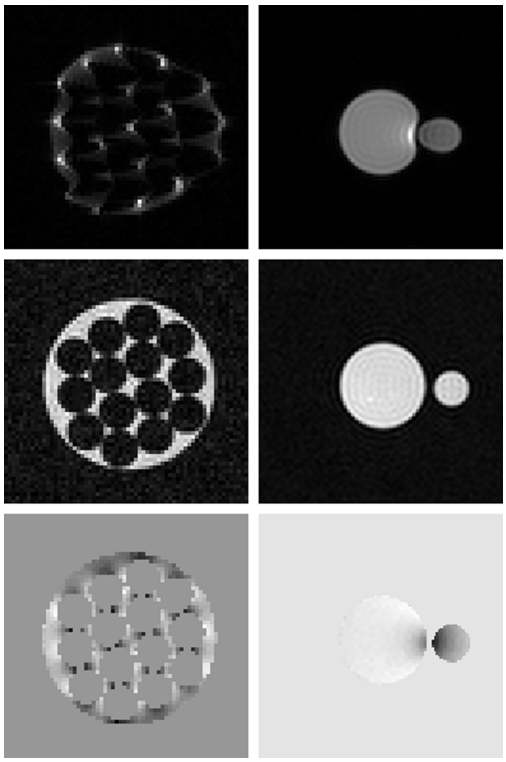

Figure 8.5: Coronal SE images (top row), SI images (middle row) and SI-derived field maps (bottom row) of a 2.25-cm diameter cylinder with doped water and fourteen 5-mm diameter test tubes with air (left column), and an external 10-mm diameter test tube with doped water (right column). In the spin echo images (top row), readout was along the left-right axis. The field-of view was doubled for examining the configuration with the external tube (right column). The field maps (bottom row) were derived from ten consecutive SI phase images that were acquired between δt=0.0 ms (m=0) and δt=1.25 ms (m=10).

coordinates, and (c) to effectuate geometrical immunity to off-resonance effects, such as caused by field inhomogeneity, susceptibility, chemical shift, f_0-offset, and field drift. Spectroscopic imaging was further shown (d) to allow detailed analysis of microscopic and macroscopic field inhomogeneities and (e) to provide a powerful base for the derivation of various kinds of undistorted parameter maps and composite images, e.g., undistorted field maps and positive contrast images.

In order to achieve geometric fidelity and localization in laboratory coordinates, several conditions have to be satisfied. First, the point where all three gradient coils produce zero magnetic fields, i.e., the isocenter of the gradient system (which typically is the same point as the isocenter of the magnet), has to exhibit a known relation with the origin of the laboratory frame as, for instance, indicated by the laser positioning system. Second, the laser positioning system has to be exactly aligned with the principal axes

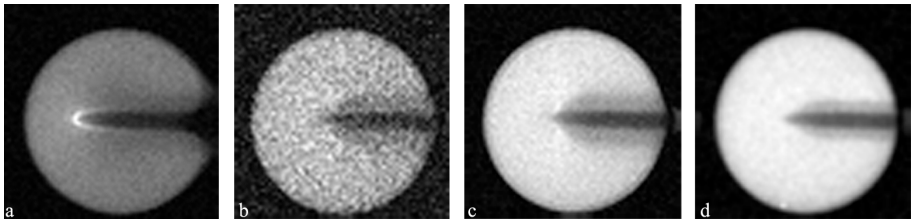

Figure 8.6: Coronal spin echo images (a,b,c) and corresponding averaged spectroscopic image (d) of a 2.25-cm diameter cylinder with doped water and a 1.8-mm diameter titanium needle. (a) SE with BW=50 Hz/pixel and 2 signal averages, scan time 20.4 s, (b) SE with BW=500 Hz/pixel and 2 signal averages, scan time 20.4 s, (c) SE with BW=500 Hz/pixel and 64 signal averages, scan time 10 min 14 s, (d) averaged spectroscopic image, scan time 10 min 14 s. B_0 along the vertical axis; readout along the horizontal axis for SE.

of the gradient system. Third, images have to be corrected for nonlinearities of the imaging gradients. Once these conditions have been satisfied, non-water-suppressed spectroscopic imaging emerges as an attractive research tool for applications that put high demands on geometric fidelity, such as radiotherapy treatment planning, stereotactic neurosurgery, stereotactic laser and radiosurgery, and image-guided interventions, e.g., needle biopsies, and adds to the value of MRI as a stand-alone modality for such applications. In addition, geometric fidelity and localization in laboratory coordinates may prove beneficial in many occasions, for instance when integrating MR images for different nuclei, e.g., ^{1}H and ^{19}F, or with other modalities, e.g., CT, or when there is a need to define or reproduce the geometry of a scan with respect to external landmarks, etc.

As compared to conventional imaging, spectroscopic imaging displays some beneficial features. Apart from providing additional information (see above), spectroscopic imaging is attractive in that encoding and acquisition are separated, as a result of which geometric perfection can be achieved with modest gradient strengths. This is different in conventional imaging, where the detrimental effects of field disturbances can be alleviated by using stronger readout gradients, but where the maximum gradient capability sets a limit to the field disturbances that can be accommodated. In addition to this, it should be realized that the use of very strong gradients may be undesirable for several reasons: a) the SNR is decreased by increasing the readout bandwidth; b) rapidly switching strong gradients induces large eddy

currents which are a source of geometric distortion themselves; c) rapidly switching strong gradients produces acoustic noise and may invoke physiological effects such as peripheral nerve stimulation.

With regard to applications, it is important to make a distinction between two complementary aspects of geometric fidelity, viz. absence of geometric distortion and localization in laboratory coordinates. The first property refers to the ability to accurately depict the object, even in the presence of implants, devices, surgical tools, etc. Obviously, this is a desirable property for procedures in which targets are defined with respect to external frames or fiducial markers, as is the case in, e.g., breast biopsy and stereotactic surgery, and for procedures in which MRI data is to be matched with data from other modalities, as in radiotherapy treatment planning [159]. The second property, localization in laboratory coordinates, is a feature that - to our knowledge - has not yet received any attention in the MRI literature. It implies that image coordinates can be directly converted into laboratory coordinates and vice versa. So, what is measured in the images will also be valid in the laboratory and, conversely, what is planned and measured in the laboratory will also be found in the images. In additions, this implies that scan planes can be directly defined or reproduced with respect to the light visor system, without having to rely on geometrically suspect scout views. It also means that the target of an intervention can be directly specified in laboratory coordinates. For interventions that do not or only minimally disturb the geometry of an object, e.g., stereotactic radiosurgery and MR-guided thermal therapies, this feature could open up new ways to MR-guided treatment.

From the foregoing discussion, MR spectroscopic imaging presents itself as an ideal tool for detailed time and frequency domain analysis of object-induced microscopic and macroscopic field inhomogeneities and may serve as the gold standard for applications that put high demands on geometric fidelity. Apart from effects associated with a limited coverage of k-space, this is indeed the case, at least for research purposes. Unfortunately, however, the favorable geometric properties of spectroscopic imaging and its wealth of information go together with a lack of efficiency. Since only one point in k-space is acquired after each excitation, as compared to, e.g., 256 points when a readout gradient is applied, spectroscopic imaging tends to be about two orders of magnitude slower than the corresponding standard imaging sequence, which imposes a limit to its clinical utility. In the present study, a 2D setup and small field-of-views and acquisition matrices were used to achieve adequate spatial resolution, while avoiding excessive scan times and still be able to demonstrate essential features. For a purely phase-encoded 3D scan,

scan times may easily become prohibitive, even more so because, in general, an oversized scan volume has to be chosen to ensure that all spins in the volume of interest have been excited. The situation may even get worse when, in the presence of extremely large field inhomogeneities, for example near steel implants, the maximum available or allowable RF bandwidth becomes too small to cover the full range of off-resonance frequencies. Multi-band excitation techniques, like those used in dedicated techniques for imaging near implants such as SEMAC [160] and MAVRIC [161], may be invoked to overcome this problem at the cost of efficiency. Further, it should be noted that conducting structures, such as metallic implants, also give rise to RF artifacts, including flip angle errors and phase errors, which may favor FID techniques over the SE techniques used in our study [162].

To put the efficiency issue in proper perspective, it should be emphasized that our study was performed on a clinical MR system with standard spectroscopic imaging capabilities and that no attempts were made to optimize the sequence with regard to scan duration, SNR, etc. In the past decades, however, several techniques have been proposed to speed up spectroscopic imaging, e.g., echo-planar techniques [163], multiple spin echo techniques [164], spiral imaging techniques [165], parallel imaging techniques [166], and sparse sampling [167]. To further improve efficiency, it can be considered to refrain from spectroscopic and temporal information altogether and only use the initial amplitude of the FID for the reconstruction of a single image. This is in fact what is done in so-called single-point imaging (SPI), a technique proposed by Emid and Creyghton in 1985 [168] and mainly employed in solid-state imaging and MR microscopy ever since. To date, applications of single-point imaging in medical research have been largely restricted to micro-imaging of solid and quasi-solid tissue specimens, e.g., bone, cartilage, tendon, and teeth [169], and prosthetic materials [170]. As with spectroscopic imaging, many techniques have been proposed to speed up the basic SPI experiment, including turbo spin-echo SPI [171–176], SPRITE, a technique in which one of the phase-encode gradients is ramped in equally spaced discrete steps [177], multi-point k-space mapping techniques [12, 178], single-point imaging with variable phase encoding interval [179], and, last but not least, sparse k-space sampling [180]. The latter technique, also termed compressed sensing (CS), has already been shown to be very effective when imaging objects which possess a sparse representation in a certain domain. This has, for instance, been shown to be the case for active and passive catheters [181, 182]. An illustration of the potential of CS for one of our phantoms is provided by Figure 7. The figure shows retrospectively recons-

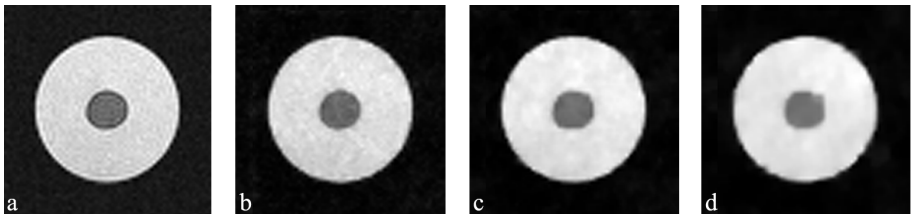

Figure 8.7: Coronal averaged spectroscopic images of a coaxial cylinder phantom with oil in the 10-mm diameter inner compartment and doped water in the 2.25-cm diameter outer compartment; images were retrospectively undersampled and reconstructed with, respectively, 100% (a), 25% (b), 10% (c) and 5% (d) of the complex k-space data.

tructed spectroscopic images of the water-oil phantom with undersampling factors 4, 10 and 20. A single spectroscopic input image was created by averaging 15 spectroscopic images around the echo top. Undersampling and reconstruction were done as described in reference [183].

Taking into account the rapid developments in multi-channel transmit techniques, parallel imaging and sparse sampling, spectroscopic imaging for investigating structure rather than chemistry may be expected to make its way to clinical MRI in the near future. At present, spectroscopic imaging techniques may already be considered for low-resolution and volume-selective studies, when the goal is to explore what MRI can achieve with regard to geometric accuracy, or when a gold standard or reference method is required against which to measure the effects of field perturbations in conventional MRI. Further, it should be realized that purely phase-encoded imaging is a natural alternative to conventional imaging when low SNR demands excessive signal averaging in conventional imaging. In that situation, which may easily arise in, for instance, fluorine and sodium imaging, phase encoding may take the place of signal averaging.

Conclusion

Non-water-suppressed spectroscopic imaging offers a fundamental solution to the geometric deficiencies of MRI. This solution may evolve towards a practical solution - and lend force to MRI as a stand alone modality for applications that require geometric accuracy - once full advantage will have been taken of recent developments with regard to scan time reduction.

They are ill discoverers that think there is no land, when they can see nothing but sea

F. Bacon

CHAPTER 9

Summary and discussion

9.1 Summary

In MR imaging a homogeneous magnetic field is used to generate a net magnetization of protons in a studied volume. The magnetic field determines the Larmor frequency, i.e., the frequency at which the magnetic moments of the individual protons precess about the magnetic field. Because of the lower potential energy for proton spins aligned parallel to the magnetic field compared to proton spins aligned anti-parallel, a net magnetization is created. This net magnetization can be perturbed by applying a radio frequency pulse at the Larmor frequency, encoded by applying field gradients, and recorded by a detection coil. The inverse Fourier transform of the acquired signal in the (spatial) frequency space results in an image. Ideally, the magnetic field over the studied volume is homogeneous, which implies that the resonance frequency is constant within the volume. However, practically this ideal situation is seldom obtained. Such non-idealities are generally caused by scanner imperfections and intrinsic properties of the studied volume which give rise to varying resonance frequencies. The varying resonance frequencies affect the acquired signal and hence the reconstructed images at various scales and in various ways.

In this thesis, the major effects of field inhomogeneities on the reconstructed images are studied. We have analyzed the effects of the field inhomogeneities on the reconstructed image and have assessed whether these inhomogeneities can be used to our advantage or can and should be compensated for. The effects of field inhomogeneities on the reconstructed image can be separated into effects on the signal phase and image distortion. The thesis is therefore subdivided into two parts. The first part concerns effects on the signal phase, while the second part covers the application and compensation of image distortion induced by field inhomogeneities.

In chapter 1, the physics behind the signal acquisition with and without inhomogeneities is described to provide the background that is needed to appreciate the subject matter. We demonstrate that whenever the magnetic field varies over a volume and hence the resonance frequency fluctuates across the volume, two effects on the reconstructed image can be distinguished. First, a gradient echo or a free induction decay acquisition will show a signal phase offset, which is determined by the amplitude and sign of the frequency offset and the echo time. Second, if frequency encoding is applied, the reconstructed image will be distorted in the frequency encoded direction. The first part of the thesis covers the effects on the signal phase, the second part is concerned with image distortions.

9.1.1 Analysis and manipulation of the effects of field inhomogeneities on the signal phase

Variations of the local Larmor frequency are generally mapped using the phase of the acquired image. Phase images are determined by applying the arctangent function on the acquired data. The arctangent function induces aliasing, which means that whenever a phase is larger than π or smaller than -π it is wrapped into the (-π, π]-interval. Due to this wrapping, a black and white stripe pattern is formed surrounding field perturbations, especially near strong field perturbing objects and for longer echo times. Phase unwrapping is difficult since it, amongst others, easily ends up in a local minimum and is error prone in areas that exhibit a low signal to noise ratio. In chapter 2, we show that phase unwrapping can be bypassed by applying the phase derivative. The phase derivative can be calculated via the derivatives of the real and imaginary signal, which do not experience wrapping.

The phase derivative allows perturbations of the image phase to be characterized. Paramagnetic field perturbing objects that locally increase the magnetic field can thereby be discriminated from diamagnetic field perturbing objects, which locally decrease the magnetic field (chapter 2, 4). The first order phase derivative magnitude provides high positive contrast surrounding a field perturbing structure (chapter 2). The phase derivative, however, is also sensitive to linear and non-linear field gradients that are caused by e.g. imperfect shimming of the main magnetic field of the scanner. The Laplacian of the image phase is shown to increase the specificity of the image phase, since it is zero in regions of constant or linearly varying susceptibility and nonzero at abrupt changes in susceptibility, for instance, at a single point, a ridge, an interface, an edge or a boundary (chapter 3).

In vivo, various field perturbing structures can be encountered, paramagnetic as well as diamagnetic. One example of a diamagnetic field perturbing object is micro-calcification in the breast. Micro-calcifications in the breast are considered to be an early indication of breast cancer. Conventional detection of breast cancer is done by mammography screening, which aims at detection of the calcified tissue. Although breast cancer can also be imaged using contrast enhanced MR imaging, the specificity of this MR based detection is relatively low. The specificity of MR based characterization and detection of breast cancer might be increased by including micro-calcification detection. In chapter 4 the discriminative power of the image phase derivative in gradient echo MRI is applied to differentiate diamagnetic micro-calcifications and paramagnetic substances, such as blood, in *ex vivo* breast

tissue, using CT as gold standard. The phase images are shown to provide valuable information, even in areas with low SNR. The discriminative power of the phase derivative is shown to increase at longer echo times. However, at longer echo times also shading due to strong field disturbing processes, for example water-fat transitions, is increased. A template matching algorithm is shown to allow automatic detection of the micro-calcifications.

The effect of field inhomogeneities on the transverse MR signal can be divided into microscopic effects, mesoscopic effects and macroscopic effects. Microscopic effects of field inhomogeneities on the transverse signal result in R_2 signal decay. This R_2 signal decay corresponds to variations of the magnetic field on a scale smaller than the diffusion length. The R_2 signal decay can not be inverted using a 180° refocusing pulse. Mesoscopic field inhomogeneities are governed by field inhomogeneities larger than the diffusion length, but smaller than the voxel size and are characterized by the R_2' signal dephasing constant. R_2' reflects local tissue characteristics and is therefore often the parameter of choice, for example in functional MRI and therapy assessment. The R_2' decay can be sampled by gradient echo acquisitions. Signal decay in a gradient echo experiment, however, is also sensitive to signal dephasing due to macroscopic field gradients. Macroscopic field gradients are field gradients over distances larger than the voxel size. As macroscopic signal dephasing does not reflect local tissue properties, it generally is a source of unwanted signal loss. In chapter 5, the macroscopic signal dephasing is assessed by calculating the phase derivatives and subsequently integrating these variations of the phase over the voxels. By dividing the data by an assessment of the macroscopic signal dephasing, the signal decay due to macroscopic signal dephasing is shown to be reduced. This method is shown to be more stable than methods that remove signal dephasing by fitting an adapted expression for the signal decay. Furthermore, by applying the correction, mesoscopic dephasing is maintained, while macroscopic signal dephasing is reduced or removed.

9.1.2 Manipulation of image distortions induced by field inhomogeneities

Frequency encoding of an image results in a positional shift of signal originating near a field perturbing object, along the direction of the frequency encoding gradient. Applying frequency encoding center-out and along all encoding directions, a so called center-out radial acquisition, results in signal pile-up symmetrically surrounding a field perturbing object. The center-out

RAdial Sampling at Off Resonance (co-RASOR) technique applies a global frequency offset to center-out encoded radial data. When this frequency offset is properly attuned to the field perturbing object, the signal pile-up surrounding the field perturbing object can be focused onto its geometrical center. In chapter 6, the frequency offset is applied during image reconstruction instead of during image acquisition. The reconstruction approach is shown to increase the flexibility and efficiency of co-RASOR, since multiple off-resonance reconstructions can be obtained from a single acquisition. The multiple frequency offsets are furthermore shown to allow the optimal frequency offset, and hence the center of a perturbing object, to be determined automatically in 3D.

The accurate localization provided by the co-RASOR technique can potentially improve MR guided tracking applications that require a high accuracy. One possible application, for 3D tracking using MRI, is the tracking of an High-Dose-Rate (HDR) brachytherapy source. Tracking of an HDR brachytherapy source would allow MRI based intra-procedural feedback on the exact location of the source with respect to tumor and critical organs, allowing dose distribution optimization during treatment. However, the 3D center-out radial acquisition as discussed in chapter 6, requires several minutes and is unsuitable for real-time tracking applications. In chapter 7 an improvement upon the 3D co-RASOR acquisition is presented. Two orthogonal 2D center-out encoded slices are shown to allow tracking of an HDR brachytherapy source in 3D. Each of the two 2D slabs allows the location to be determined accurately in-plane, while the through-plane coordinate is covered by one of the in-plane coordinates of the perpendicular slab. The dual-plane method allows tracking of the HDR brachytherapy source within 4 seconds, which corresponds to the source dwell times that are typically used in HDR brachytherapy.

Lack of spatial accuracy caused by frequency encoding of the data is a recognized problem in MR imaging for applications that put high demands on geometric fidelity, such as radiotherapy treatment planning and stereotactic neurosurgery. In chapter 8 a purely phase encoded image is shown to be geometrically immune to field inhomogeneities. The phase encoding in all imaging directions allows parameter maps to be generated that preserve the geometry of an object and allow localization of object features in world coordinates. These parameter maps allow the signal loss and the magnetic fields to be accurately sampled. A disadvantage of pure phase encoding, however, is that it is relatively slow. It is shown that, to some extent, the method can be speeded up, without losing geometrical accuracy, by applying

under-sampling strategies.

9.2 Discussion

9.2.1 Factors that determine the sensitivity of the phase

The effects of magnetic field perturbations on the image phase scale linearly with the magnetic field strength. Hence magnetic field perturbations are more noticeable at higher magnetic field strengths. However, all effects affecting the image phase scale with the magnetic field strength. In other words, the image phase is more sensitive to small perturbations, but also more easily disturbed by strong field perturbations at higher field strength. The phase image is thereby more easily clouded by strong field inhomogeneities and, for example, water-fat phase artifacts. Water-fat artifacts at high field strengths are caused by the multiple fat peaks, for which especially at higher magnetic field strengths and longer echo times, in-phase conditions cannot be obtained [86]. To image the micro-calcifications, which have sizes in the order of 60 μm, long echo times are needed [13, 24]. Unfortunately, the clinically relevant area for micro-calcification detection is the glandular tissue, at which water-fat transitions are to be expected. Future research is needed to determine the optimal choice for the echo times to discriminate micro-calcifications, while suppressing the effects of water-fat transitions on the image phase.

9.2.2 Limitations of the presented techniques

Limitations of using image derivatives

The derivatives as applied in chapter 2-5 show great potential. The derivatives however should be interpreted with great care. For example, the detection of micro-calcifications by applying the phase derivative images in chapter 4, needs to be performed in 3D. The branching of blood vessels can result in a pattern that is easily misinterpreted as a diamagnetic field perturbation. By using the 3D data, mis-interpretation of such branching structures can be avoided.

Calculating the phase derivative by applying the Fourier derivative theorem, as done in chapter 5, has the advantage that the derivative of the phase can be determined up to any order. However, higher order derivatives become more susceptible to artifacts, such as ringing. The Laplacian of the

phase is shown to increase the specificity of the phase derivative. Since the Laplacian of the phase already indicates abrupt transitions of the susceptibility, little additional information might be gained by calculating higher order phase derivative images. Note that the phase derivative as well as the Laplacian are also sensitive to abrupt changes in signal intensity, for example at the edges of the phantom.

Phase and phase derivative images are known to be sensitive to flow and movement [40, 184]. Phase derivative imaging *in vivo* is therefore more challenging than *ex vivo*, especially in the breast. For example, imaging in the breast *in vivo* is hampered by breathing, which causes movement and induces susceptibility artifacts due to the air in the lungs [94]. These two imaging artifacts influence the phase in two ways. First, the signal magnitude is reduced because of signal dephasing [12, 22]. Due to the reduced signal amplitude the effect of noise on the phase (derivative) images is higher. Second, the macroscopic fluctuations of the magnetic field result in fluctuations of the signal phase [11, 19, 23].

To correct for the macroscopic effects of field inhomogeneities, two approaches have been proposed: adaptation of the signal acquisition [3, 11, 48, 86, 105–109] and correction via postprocessing [12, 22, 23, 110, 111, 133]. As illustrated in chapter 5, the effects of macroscopic dephasing can be reduced by using postprocessing. However, for the correction to be applicable, some signal should be left. Furthermore, the first three polynomials of the Taylor series, which were applied in chapter 5, are only a good approximation for small values of the phase derivative. Hence not all effects can be removed by the method used in this work. In other words, for strong field perturbing objects other approaches might be beneficial to provide an estimate of the (mesoscopic) signal dephasing [185]. The best approach against field inhomogeneities would be to ensure that the magnetic field is as homogeneous as possible when performing the signal acquisition. One example of such an approach is accurate shimming, for example by using field probes [86, 186, 187]. Another example is to improve upon the homogeneity by using the data available from multiple receive coils [188, 189]. After the data acquisition, the postprocessing correction methods, such as presented in chapter 5, can still be applied to remove residual macroscopic signal dephasing effects.

Limitations of the co-RASOR technique

The co-RASOR method presented in chapter 7 showed potential of tracking devices with a frame rate of 0.25Hz. For many applications this frame rate is too low. Especially tracking of catheters and needles usually requires higher frame rates. Currently, methods are available that provide mm accuracy at frame rates up to 20 Hz [190, 191, 191–196]. For co-RASOR tracking, as presented in chapter 7, to be able to compete with these methods, it needs to be speeded up.

The methods presented in literature provide some approaches to do so [191, 196]. First, the data matrix can be reduced by reducing the field of view. A smaller data matrix does not necessarily decreases the anatomy displayed surrounding the determined position of the device, since the locations obtained by the dual-plane acquisitions can be projected onto a 3D acquisition that is obtained prior to the intervention. Another option to increase the frame rate is to use data under-sampling [134]. This method allows for a reduction of the acquisition duration without compromising the geometrical accuracy. Under-sampling up to 50% of the data has been shown to be possible. Already such small improvements would allow tracking with a frame rate in the order of 1 Hz or higher using co-RASOR.

Limitations of SPI imaging

SPI imaging has been shown to present undistorted images, which can be interpreted in world coordinates. Whether SPI will be applied in studies that require a high geometric accuracy in which conventional acquisitions fail, is uncertain. As discussed in chapter 8, the applicability *in vivo* of SPI will depend on the increase in efficiency that can be obtained. Although under-sampling strategies potentially can reduce the acquisition time considerably, they should be applied with care [151, 197]. By applying under-sampling strategies information is lost. As a consequence, the evolution of the signal over time, as illustrated in the figures in chapter 8, might show differences induced by the under-sampling.

9.2.3 Other approaches to image field perturbations

Susceptibility-weighted imaging

The potential of phase contrast has been gaining in interest ever since the introduction of increasingly high field strengths. An approach that has been

used frequently in clinical research is susceptibility-weighted imaging (SWI) [49]. In SWI imaging, a gradient echo sequence is used to obtain a complex image. The phase image is subsequently unwrapped and high-pass filtered to remove phase wraps and the influence of macroscopic field inhomogeneities. The resultant phase image is scaled between 0 and 1, windowed and thereafter used as a weighting map for the magnitude data. A phase or susceptibility weighted magnitude image is obtained by multiplying the weighting map and the magnitude image four times [49]. The simplicity of the SWI approach is attractive. The additional information obtained by weighting the magnitude image, however, is slight. The contrast of the SWI images resembles the contrast in the magnitude image. A more natural approach would be to visualize the additional information that is gained by studying the phase (derivative) itself.

Quantitative Susceptibility Mapping

Another approach to study the information contained in the signal phase is Quantitative Susceptibility Mapping (QSM) [66, 92, 198, 199]. Like the phase derivative images and SWI, QSM applies gradient echo acquisitions to extract information from the signal phase. In QSM the inverse problem is solved to assess the local susceptibility [199]. The inverse problem reconstructs the susceptibility distribution that gives rise to the observed magnetic field. However, a number of problems are associated with this inverse problem. First, phase has to be unwrapped and the effect of macroscopic field inhomogeneities on the signal phase should be removed. Second, the problem is ill-defined at the center of k-space. Third, at the so-called magic angle the Laplacian of the signal phase diverges. The divergence results in ill-defined solutions to the inverse problem [199]. To solve the ill-defined problem, many strategies have been proposed. These solutions include scanning of an object in many orientations with respect to the main magnetic field [200, 201] and postprocessing methods [199, 202].

The contrast provided by the QSM maps has ever since its introduction been a source of debate. The contrast, for example, has been shown to depend on the orientation of the objects with respect to the main magnetic field [203]. Although this may indicate that the susceptibility is not a scalar but a tensor, it may also reflect the microscopic and/or mesoscopic heterogeneity of tissues [204]. The Quantitative Susceptibility Maps thereby do not necessarily reflect an absolute tissue property, although the resemblance to the absolute quantity is certainly there. Furthermore, not all solutions to this

ill-defined problem are easily performed in clinical situations, e.g., multiple orientations of an object with respect to the scanner are impractical. However, the results presented so far are promising, especially in the brain [66, 92].

Potentially, QSM would be a valuable tool, since it would allow detection of perturbations based on their susceptibility, which unlike the signal phase, is a tissue property. For example, in breast images the detection of the microcalcifications could be simplified by calculating the susceptibility, since calcified tissue could in those instances be visualized by windowing the maps. The first result of QSM in breast tissue has already been shown as a conference proceeding [92]. However, the results presented in that work were obtained for rather large perturbations, which are more easy to detect. Small calcifications with sizes in the order of 60 μm, as routinely detected via CT mammography, are still very challenging to image using MR imaging.

9.2.4 Other applications of the presented techniques

The applications illustrated in this work form a subset of the applications that are conceivable. For example, the discriminative power of the phase and in particular the phase derivative has, for example, already been used to discriminate calcification and micro-bleedings in the brain [205]. Furthermore, the phase derivative magnitude has shown potential for increasing the specificity of the detection of micro-bleedings [206].

The reduction of the signal dephasing, as described in chapter 5, can be applied in a variety of imaged locations. For example, breast images suffer from dephasing due to air in the lungs, but also prostate images are known to suffer from macroscopic signal dephasing, for example because of air in the intestines. Also the quantification of holmium microspheres, which are used for treatment of liver metastases [185, 207], might be improved by removing macropscopic signal dephasing due to air in the lungs or air in the intestines. Moreover, temperature mapping algorithms, which fit the evolution of the signal over time, might perform better after removal of macroscopic field inhomogeneities [208].

The co-RASOR acquisition and co-RASOR tracking technique have several possible applications. Among these potential applications are the localization of I-125 brachytherapy seeds in the prostate [123]. Nowadays, clinical routine consists of MRI acquisitions for visualizing tumor and surrounding structures and a CT image to localize the brachytherapy seeds. We have shown accurate localization of these seeds using co-RASOR [4, 149], which might obviate the need for CT imaging. The tracking application focused

at HDR-brachytherapy of the prostate, but can possibly be applied to image guided brachytherapy at other locations, e.g. the oesophagus or the uterus, as well. Co-RASOR tracking might also be applied in needle interventions, for example in biopsy procedures [98].

The single point imaging technique may have applications in areas experiencing high and strongly varying field offsets, such as near the nasal cavity, near or in the ears or near metallic implants. However, first the imaging duration has to be significantly reduced before clinical applications become within reach. As a gold standard it might provide a good ground truth for (research) applications that require high geometric accuracy, such as the MRI accelerator [197].

9.3 Conclusion

Field inhomogeneities result in signal phase alterations as well as distortion of images when signal is frequency encoded. The signal phase is not easily interpreted because of phase wrapping, especially near areas of low SNR. These problems can be partially solved by calculating the phase derivative. The signal phase derivative can provide valuable contrast, which allows detection and discrimination of field perturbing objects, such as bleedings and micro-calcifications. The signal phase furthermore allows compensation of unwanted signal loss caused by macroscopic field gradients.

The image distortion caused by field inhomogeneities allows their center to be located accurately in 3D by applying a frequency offset to 3D center-out frequency encoded data. This frequency offset, which needs to be properly attuned to the object, is more effectively applied during reconstruction than during acquisition. By using a dual-plane center-out frequency encoded acquisition, a brachytherapy source can be located with mm accuracy in 4 seconds. Undistorted images in world coordinates can be obtained by using phase encoding in all imaging directions

In conclusion, we have shown that by careful analysis of the effects of field inhomogeneities, their effects on the signal can be understood and that by understanding the effects of field inhomogeneities on the reconstructed image, the effects can either be put to use or, in case of unwanted effects, can be (partially) compensated for.

Alles wat we schrijven, is een vertaling

K. Bruin

CHAPTER 10

Samenvatting en conclusie

10.1 Samenvatting

Magnetische resonantie beeldvorming (MRI) maakt gebruik van een sterk en homogeen magneetveld om een netto magnetisatie van protonen te creëren in een bestudeerd volume. De sterkte van het gebruikte hoofdmagneetveld bepaalt de precessiefrequentie van de protonen rondom dit magneetveld, de zogenaamde Larmorfrequentie. Protonen parallel aan het magneetveld hebben, ten opzichte van protonen anti-parallel aan het magneetveld, een lagere potentiële energie, waardoor een netto magnetisatie wordt gecreëerd binnen het object in het magneetveld. Deze netto magnetisatie kan vervolgens geëxciteerd worden door middel van een radiofrequente puls, met als draagfrequentie de Larmorfrequentie, waarna het signaal gecodeerd kan worden door veldgradiënten aan te leggen, om opgevangen te worden met behulp van een ontvangstspoel. Een inverse-Fouriertransformatie van het in de (spatiële) frequentieruimte (k-space) gecodeerde signaal resulteert vervolgens in een beeld.

In een ideaal MRI experiment is het hoofdmagneetveld homogeen over het bestudeerde volume, zodat ook de Larmorfrequentie constant is over het bestudeerde volume. In de praktijk wordt deze situatie echter zelden tot nooit bereikt. Variaties van de Larmorfrequentie binnen een object kunnen bijvoorbeeld veroorzaakt worden door onder andere scannerimperfecties en de intrinsieke magnetische eigenschappen van het bestudeerde volume. Deze, door veldinhomogeniteiten veroorzaakte, frequentievariaties hebben verschillende effecten op het geacquireerde signaal en de gereconstrueerde beelden. In dit proefschrift hebben we de belangrijkste gevolgen van veldinhomogeniteiten op het gereconstrueerde beeld geanalyseerd. Bij die analyse zijn de effecten van veldinhomogeniteiten op het gereconstrueerde beeld onderverdeeld in twee categorieën: allereerst effecten op de fase van het signaal en ten tweede vervormingen van het gereconstrueerde beeld. Na het introduceren van de basis in hoofdstuk 1, die nodig is om het geheel te kunnen appreciëren, hebben we in het proefschrift voor dezelfde tweedeling gekozen. In het eerste gedeelte (hoofdstukken 2 tot 5) worden de effecten op de fase beschouwd, terwijl in het tweede gedeelte (hoofdstukken 6 tot 8) het gebruik en de compensatie van de geïnduceerde vervorming worden behandeld.

10.1.1 I Analyse en manipulatie van de effecten van veldinhomogeniteiten op de fase van het signaal (Hoofdstuk 2-5)

Lokale variaties van de Larmorfrequentie worden doorgaans weergegeven in de fase van het acquireerde signaal. Echter, deze fasebeelden zijn in het algemeen moeilijk te interpreteren omdat de berekende fase alleen waarden binnen het (-π,π]-interval weergeeft. Waarden buiten dat interval worden in dit interval geprojecteerd door een aantal maal 2π bij de werkelijk fase op te tellen, of door een veelvoud van 2π van de werkelijke fase af te trekken. Door dit beperkte interval worden zwart-wit strepenpatronen geïnduceerd, voornamelijk rondom grote veldverstoringen en bij gebruik van lange echo- of acquisitietijden. Verwijderen van het strepenpatroon is moeilijk omdat deze procedures foutgevoelig zijn rondom gebieden met een lage signaal-ruisverhouding en makkelijk in een lokaal optimum eindigen. In hoofdstuk 2 laten we zien dat het verwijderen van het zwart-wit patroon kan worden omzeild door de verandering van de fase te bestuderen met behulp van de fase-afgeleide. De fase-afgeleide kan direct worden uitgerekend met behulp van de (verandering in de) geacquireerde complexe signalen en dus zonder gebruikmaking van de berekening van de fase die verantwoordelijk was voor het ongewenste strepenpatroon.

De afgeleide van de fase kan worden gebruikt om veldverstoringen te karakteriseren. Hierdoor kunnen paramagnetische en diamagnetische veldverstoorders, die respectievelijk het veld lokaal verhogen dan wel verlagen, worden onderscheiden (hoofdstuk 2,4). De grootte van de fase-afgeleide laat positief contrast zien rondom veldverstoringen (hoofdstuk 2). De fase-afgeleide is echter gevoelig voor lineaire en niet-lineaire veldgradienten die bijvoorbeeld worden veroorzaakt doordat het magneetveld, al dan niet na shimming, onvoldoende homogeen is. De Laplaciaan van de fase vergroot de specificiteit waarmee de fase kan worden bestudeerd, omdat deze nul is in gebieden met constante of lineair variërende susceptibiliteit en ongelijk aan nul rondom abrupte veranderingen in de susceptibiliteit, bijvoorbeeld bij een enkel punt, bij een rand, een overgang of een grens (hoofdstuk 3).

In vivo kan men verschillende veldverstorende structuren tegenkomen, zowel paramagnetisch als diamagnetisch. Micro-calcificaties in de borst zijn bijvoorbeeld diamagnetische veldverstoorders. Micro-calcificaties worden beschouwd als de eerste indicaties van borstkanker. De gangbare klinische insteek bij een vermoeden van borstkanker, mammografie, is gericht op het detecteren van gecalcificeerd weefsel. MRI beelden, waarbij het contrast is

verhoogd door middel van een contrastmiddel, kunnen gebruikt worden om borstkanker in beeld te brengen. De specificiteit van deze methode is echter relatief laag. De specificiteit van MRI kan mogelijk worden vergroot door microkalk ook met behulp van MRI te detecteren. In hoofdstuk 4 worden de onderscheidende eigenschappen van de fase-afgeleide gebruikt om microcalcificaties (diamagnetisch) te onderscheiden van paramagnetische veldverstoringen, zoals bloed, in *ex vivo* borstweefsel. De fase-afgeleide beelden geven, ter validatie, dezelfde calcificaties weer als de gouden standaard, CT beelden. De fase-afgeleide beelden laten waardevol contrast zien, zelfs op plaatsen met een relatief lage signaal-ruisverhouding. Het onderscheidend vermogen van de fase-afgeleide neemt toe bij langere echo tijden. Echter, bij langere echo tijden kunnen mogelijke relevante of interessante structuren ook eerder worden overschaduwd door sterke veldverstoringen, zoals water-vet overgangen.

De gevolgen van veldinhomogeniteiten op het gedetecteerde MRI signaal kunnen worden onderverdeeld in effecten op drie niveaus: microscopisch, mesoscopisch en macroscopisch. Microscopische effecten resulteren in R_2 signaalverval. Dit R_2 signaalverval wordt veroorzaakt door variaties van het magneetveld op een schaal kleiner dan de diffusielengte. Mesoscopische veldinhomogeniteiten worden veroorzaakt door veldinhomogeniteiten op een schaal groter dan de diffusielengte en worden gekarakteriseerd door de R_2' signaalvervalconstante. De R_2' vervalconstante weerspiegelt daardoor de lokale weefseleigenschappen en is daarom een vaak gebruikte parameter, bijvoorbeeld in functionele MRI en bij het beoordeling van de effectiviteit van therapieën. De R_2' vervalconstante kan worden gemeten met behulp van een gradient-echo MR opname. Het gradient-echo signaalverval wordt echter ook veroorzaakt door macroscopische veldinhomogeniteiten. Deze macroscopische veldinhomogeniteiten spelen op afstanden groter dan de voxelgrootte, waardoor deze meestal geen afspiegeling van het lokale weefsel zijn. Dit signaalverlies is daarom ook vaak ongewenst. In hoofdstuk 5 maken we een afschatting van dit signaalverlies door de fase-afgeleide te integreren over de voxels. Door de geacquireerde dataset te delen door het geschatte signaalverlies wordt het macroscopische signaalverlies gereduceerd, terwijl het mesoscopische signaalverlies wordt behouden. De methode is sneller en stabieler dan methodes die het macroscopische signaalverlies verwijderen door een aangepast model aan de data te fitten.

10.1.2 II Het gebruik en de compensatie van vervormingen van beelden geïnduceerd door veldinhomogeniteiten (Hoofdstuk 6-8)

Het gebruik van frequentiecodering, voor codering van het signaal van een object, veroorzaakt een verschuiving van signaal rondom de veldverstoorder parallel aan de frequentiecodering. Acquisities met frequentiecodering in alle coderingsrichtingen, zoals een vanuit het centrum radiaal gecodeerde beeldacquisitie, resulteren in symmetrische signaalophoping rondom een veldverstorend object. Center-out RAdial Sampling with Off-Resonance, dat afgekort co-RASOR wordt genoemd, past een globale resonantiefrequentieverschuiving toe op data die vanuit het centrum radiaal gecodeerd is. Door de resonantiefrequentie-verschuiving af te stemmen op het veldverstorende object kan signaalophoping, die zonder deze ingreep symmetrisch rondom de verstoorder zou zijn verdeeld, precies in het geometrische centrum van het object worden gefocused. De flexibiliteit en efficiëntie van de co-RASOR techniek kan worden verhoogd door de frequentieverschuiving toe te passen gedurende de beeldreconstructie in plaats van tijdens de beeldacquisitie, zoals aangetoond in hoofdstuk 6. Door deze aanpassing kunnen meerdere frequentieverschuivingen worden toegepast op één enkele acquisitie. De resultaten voor verschillende frequentieverschuivingen kunnen vervolgens worden gebruikt om de optimale frequentieverschuiving, en daarmee dus ook het centrum van de verstoorder(s), automatisch te vinden in 3D.

Een potentiele toepassing van de accurate lokalisatie, zoals die door co-RASOR wordt geboden, zijn tracking-experimenten die een hoge spatiele nauwkeurigheid vereisen, zoals bijvoorbeeld voor het MRI-geleid volgen van een HDR-brachytherapiebron. Het MRI-geleid volgen van een HDR-bron zou het mogelijk kunnen maken om, gedurende een procedure, de plaats van de bron ten opzichte van de tumor en kwetsbare organen te volgen, waardoor de distributie van de afgegeven dosis kan worden geoptimaliseerd. Echter, de 3D-acquisitie, zoals in hoofdstuk 6 werd gebruikt, duurt enkele minuten, waardoor deze te langzaam is om de plaats van een bron te volgen. Een verbetering op de 3D co-RASOR-techniek bestaande uit twee radiaal gecodeerde plakken die haaks op elkaar worden geplaatst wordt gepresenteerd in hoofdstuk 7. De 2D plakken staan nauwkeurige plaatsbepaling toe in de coördinaten in het gescande vlak, terwijl de positie in de derde richting door de tweede 2D opname, die loodracht op dat vlak is geacquireerd, kan worden bepaald. Door de tweevlaks acquisitie kan een HDR-brachytherapiebron worden gevolgd in 3D en met een verversingtempo van 4 seconden per ac-

quisitie, een duur die overeenkomt met een tijdspanne waarin een bron verplaatst wordt tijdens HDR brachytherapie.

Frequentiecodering van de data beperkt de spatiële nauwkeurigheid van MRI beelden. Deze beperking kan een probleem worden voor applicaties die hoge spatiële nauwkeurigheid vereisen, zoals radiotherapie planning en stereotactische neurochirurgie. In hoofdstuk 8 laten we zien dat een beeld dat gecodeerd is door fasecodering in alle richtingen (Single Point Imaging, SPI) geometrisch immuun is voor veldinhomogeniteiten. Met SPI kunnen hierdoor verschillende parameters, bijvoorbeeld het lokale signaalverlies en het lokale magneetveld, in kaart worden gebracht in een waarheidsgetrouwe afbeelding van een object. SPI opent daarnaast ook de mogelijkheid om coördinaten in het beeld direct te vertalen naar wereldcoördinaten. Een nadeel van het gebruik van fasecodering in alle richtingen is echter dat het veel tijd kost. Een versnelling van de acquisitie, zonder de geometrische nauwkeurigheid te verliezen, kan echter worden behaald, door het aantal meetpunten te verminderen.

10.2 Conclusie

Veldinhomogeniteiten verstoren de fase van het MRI signaal en induceren vervormingen van het MRI beeld bij frequentie-codering van het signaal. Het interpreteren van de fase is moeilijk, vooral in gebieden met een lage signaal-ruisverhouding en nabij sterke verstoringen van het magneetveld. Interpretatie van de fase door middel van fase-afgeleide beelden lost een aantal beperkingen van de fase-beelden op. Door gebruik te maken van fase-afgeleide beelden kan onder andere onderscheid tussen bloedingen en micro-calcificaties worden gemaakt. Daarnaast kan ook ongewenst signaalverlies, zoals onder meer veroorzaakt door macroscopische veldgradiënten, worden verminderd door de fase-afgeleides te gebruiken.

Vervormingen van het gereconstrueerde beeld, zoals veroorzaakt door veldinhomogeniteiten, kunnen worden toegepast om accuraat het centrum van symmetrische objecten, zoals bollen en cylinders, te vinden in 3D. Voor deze nauwkeurige plaatsbepaling moet een frequentieverschuiving worden toegepast op data die, vanuit het centrum, frequentiegecodeerd is in alle coderingsrichtingen. Deze frequentieverschuiving, die specifiek afgestemd moet worden op een object, kan effectiever worden toegepast tijdens de beeldreconstructie dan gedurende de beeldacquisitie. Accurate lokalisatie van objecten in 3D kan ook worden bereikt door gebruik te maken van twee,

vanuit het centrum, frequentiegecodeerde 2D vlakken. Die 2D acquisitie levert een versnelling op ten opzichte van de oorspronkelijke 3D-acquisitie. Een HDR-brachytherapie bron kan hierdoor worden gevolgd met millimeter nauwkeurigheid en binnen vier seconden per acquisitie. Aan de andere kan kunnen onvervormde beelden worden verkregen door gebruik te maken van fasecodering in alle coderingsrichtingen. In deze beelden corresponderen alle coördinaten 1-op-1 met de werkelijke coördinaten.

Samenvattend kunnen we stellen dat we hebben laten zien dat door de effecten van veldinhomogeniteiten op het geacquireerde signaal te begrijpen, we in staat zijn om de effecten te kunnen benutten of, in het geval van ongewenste effecten, hun effect kunnen verminderen.

Citer les pensées des autres, c'est regretter de ne pas les avoir trouvées soi-même

S. Guitry

CHAPTER 11

Bibliography

Bibliography

[1] F. Bloch. Nuclear Induction. *Phys.Rev.*, 70:460–474, 1946.

[2] J. F. Schenck. The role of magnetic susceptibility in magnetic resonance imaging: MRI magnetic compatibility of the first and second kinds. *Medical Physics*, 23:815–850, 1996.

[3] J. H. Seppenwoolde, M. A. Viergever, and C. J. G. Bakker. Passive tracking exploiting local signal conservation: The white marker phenomenon. *Magnetic Resonance in Medicine*, 50(4):784–790, 2003.

[4] P. R. Seevinck, H. de Leeuw, C. Bos, and C. J. G. Bakker. Highly localized positive contrast of small paramagnetic objects using 3D center-out RAdial Sampling with Off-Resonance reception. *Magnetic Resonance in Medicine*, 65:146–156, 2011.

[5] E. M. Haacke, R. W. Brown, M. R. Thompson, and R. Venkatesan. *Magnetic Resonance Imaging: Physical Principles and Sequence Design*. New York: John Wiley and Sons, Inc., 1999.

[6] N. Bloembergen, E. M. Purcell, and R. V. Pound. Relaxation Effects in Nuclear Magnetic Resonance Absorption. *Phys.Rev.*, 73:679–746, 1948.

[7] R. M. Weisskoff and S. Kiihne. Mri susceptometry: Image-based measurement of absolute susceptibility of mr contrast agents and human blood. *Magnetic Resonance in Medicine*, 24:375–383, 1992.

[8] J. A. Hopkins and F. W. Wehrli. Magnetic susceptibility measurement of insoluble solids by NMR: Magnetic susceptibility of bone. *Magnetic Resonance in Medicine*, 37(4):494–500, 1997.

[9] L. Li and J. S. Leigh. Quantifying arbitrary magnetic susceptibility distributions with MR. *Magnetic Resonance in Medicine*, 51(5):1077–1082, 2004.

[10] D. A. Yablonskiy and E. M. Haacke. Theory of NMR signal behavior in magnetically inhomogeneous tissues - the static dephasing regime. *Magnetic Resonance in Medicine*, 32(6):749–763, 1994.

[11] S. Baudrexel, S. Volz, C. Preibisch, J. C. Klein, H. Steinmetz, R. Hilker, and R. Deichmann. Rapid Single-Scan $T_2^\star$-Mapping Using Exponential Excitation Pulses and Image-Based Correction for Linear Background Gradients. *Magnetic Resonance in Medicine*, 62(1):263–268, 2009.

[12] M. A. Fernandez-Seara and F. W. Wehrli. Postprocessing technique to correct for background gradients in image-based $R_2^\star$ measurements. *Magnetic Resonance in Medicine*, 44(3):358–366, 2000.

[13] R. Baker, K. D. Rogers, N. Shepherd, and N. Stone. New relationships between breast micro-calcifications and cancer. *British Journal of Cancer*, 103(7):1034–1039, 2010.

[14] C. J. Allegra, D. R. Aberle, P. Ganschow, S. M. Hahn, Clara N. Lee, S. Millon-Underwood, M. C. Pike, S. D. Reed, A. F. Saftlas, S. A. Scarvalone, A. M. Schwartz, C. Slomski, G. Yothers, and R. Zon. National Institutes of Health State-of-the-Science Conference Statement: Diagnosis and Management of Ductal Carcinoma In Situ September 22-24, 2009. *Journal of the National Cancer Institute*, 102(3):161–169, 2010.

[15] R. Holland and J. H. C. Hendriks. Micro-calcifications associated with Ductal Carcinoma In-Situ - Mammographic-Pathological correlation. *Seminars in Diagnostic Pathology*, 11(3):181–192, 1994.

[16] M. M. A. Conijn, M. I. Geerlings, P. R. Luijten, J. J. M. Zwanenburg, F. Visser, G. J. Biessels, and J. Hendrikse. Visualization of Cerebral Microbleeds With Dual-Echo T2*-Weighted Magnetic Resonance Imaging at 7.0 T. *Journal of Magnetic Resonance Imaging*, 32(1):52–59, 2010.

[17] J. G. Ojemann, E. Akbudak, A. Z. Snyder, R. C. McKinstry, M. E. Raichle, and T. E. Conturo. Anatomic localization and quantitative analysis of gradient refocused echo-planar fMRI susceptibility artifacts. *NeuroImage*, 6(3):156–167, 1997.

[18] S. Ogawa, T. M. Lee, A. R. Kay, and D. W. Tank. Brain Magnetic-Resonance-Imaging with contrast dependent on Blood Oxygentation. *Proceedings of the National Academy of Sciences of the United States of America*, 87(24):9868–9872, 1990.

[19] S. Volz, E. Hattingen, C. Preibisch, T. Gasser, and R. Deichmann. Reduction of susceptibility-induced signal losses in multi-gradient-echo

images: Application to improved visualization of the subthalamic nucleus. *NeuroImage*, 45(4):1135–1143, 2009.

[20] M. A. Moerland, R. Beersma, R. Bhagwandien, H. K. Wijrdeman, and C. J. G. Bakker. Analysis and correction of geometric distortions in 1.5T Magnetic Resonance Images for use in Radiotherapy Treatment Planning. *Physics in Medicine and Biology*, 40(10):1651–1664, 1995.

[21] C. J. G. Bakker, J. H. Seppenwoolde, and K. L. Vincken. Dephased MRI. *Magnetic Resonance in Medicine*, 55(1):92–97, 2006.

[22] X. Yang, S. Sammet, P. Schmalbrock, and M. V. Knopp. Postprocessing correction for distortions in $T_2^\star$-decay caused by quadratic cross-slice B_0 inhomogeneity. *Magnetic Resonance in Medicine*, 63(5):1258–1268, 2010.

[23] H. de Leeuw and C. J. G. Bakker. Correction of gradient echo images for first and second order macroscopic signal dephasing using phase derivative mapping. *NeuroImage*, 60(1):818–829, 2012.

[24] J. R. Reichenbach, R. Venkatesan, D. A. Yablonski, M. R. Thompson, S. Lai, and E. M. Haacke. Theory and application of static field inhomogeneity effects in gradient-echo imaging. *Journal of Magnetic Resonance Imaging*, 7:266–279, 1997.

[25] M. D. Robson, P. D. Gatehouse, M. Bydder, and G. M. Bydder. Magnetic resonance: An introduction to ultrashort TE (UTE) imaging. *Journal of Compute Assisted Tomography*, 27(6):825–846, 2003.

[26] J. Frahm, K. D. Merboldt, and W. Hänicke. Direct FLASH MR imaging of magnetic field inhomogeneities by gradient compensation. *Magnetic Resonance in Medicine*, 6(4):474–480, 1988.

[27] Z. H. Cho, D. J. Kim, and Y. K. Kim. Total inhomogeneity correction including chemical shifts and susceptibility by view angle tilting. *Medical Physics*, 15(1):7–11, 1988.

[28] P. A. Hardy, W. Kucharczyk, and R. M. Henkelman. Cause of signal loss in mr images of old hemorrhagic lesions. *Radiology*, 174(2):549–555, 1990.

[29] S. Posse. Direct imaging of magnetic field gradients by group spin-echo selection. *Magnetic Resonance in Medicine*, 25:12–29, 1992.

[30] R. J. Ordidge, J. M. Gorell, J. C. Deniau, R. A. Knight, and J. A. Helpern. Assessment of relative brain iron concentrations using T_2-weighted and $T_2^\star$-weighted MRI at 3 Tesla. *Magnetic Resonance in Medicine*, 32(3):335–341, 1994.

[31] J. Frahm, K. D. Merboldt, and W. Hanicke. The effects of intravoxel dephasing and incomplete slice refocusing on susceptibility contrast in Gradient-Echo MRI. *Journal of magnetic resonance series B*, 109(2):234–237, 1995.

[32] R. T. Constable. Functional mr imaging using gradient-echo echo-planar imaging in the presence of large static field inhomogeneities. *Journal of Magnetic Resonance Imaging*, 5:746–752, 1995.

[33] Q. X. Yang, B. J. Dardzinski, S. Z. Li, P. J. Eslinger, and M. B. Smith. Multi-gradient echo with susceptibility inhomogeneity compensation (MGESIC): Demonstration of fMRI in the olfactory cortex at 3.0 T. *Magnetic Resonance in Medicine*, 37(3):331–335, 1997.

[34] Q. X. Yang, G. D. Williams, R. J. Demeure, T. J. Mosher, and M. B. Smith. Removal of local field gradient artifacts in $T_2^\star$-weighted images at high fields by gradient-echo slice excitation profile imaging. *Magnetic Resonance in Medicine*, 39(3):402–409, 1998.

[35] G. H. Glover. 3D z-shim method for reduction of susceptibility effects in BOLD fMRI. *Magnetic Resonance in Medicine*, 42(2):290–299, 1999.

[36] R. T. Constable and D. D. Spencer. Composite image formation in z-shimmed functional MR imaging. *Magnetic Resonance in Medicine*, 42(1):110–117, 1999.

[37] K. D. Merboldt, J. Finsterbusch, and J. Frahm. Reducing inhomogeneity artifacts in functional mri of human brain activation - thin sections vs gradient compensation. *Journal of Magnetic Resonance*, 145(2):184–191, 2000.

[38] H. Jara and F. W. Wehrli. Determination of background gradients with diffusion mr imaging. *Journal of Magnetic Resonance Imaging*, 4(6):787–797, 1994.

[39] W. S. Price, P. Stilbs, B. Jonsson, and O. Soderman. Macroscopic Background Gradient and Radiation Damping Effects on High-Field

PGSE NMR Diffusion Measurements. *Journal of Magnetic Resonance*, 150(44):49–56, 2001.

[40] R. M. Hoogeveen, C. J. G. Bakker, and M. A. Viergever. Phase derivative analysis in MR angiography: Reduced V-enc dependency and improvement vessel wall detection in laminar and disturbed flow. *Journal of Magnetic Resonance*, 7:321–330, 1997.

[41] D. C. Ghiglia and M. D. Pritt. *Two-dimensional Phase Unwrapping: Theory, Algorithms, And Software*. John Wiley and Sons, Inc., 1998.

[42] C. J. G. Bakker and R. de Roos. Concerning the preparation and use of substances with a magnetic susceptibility equal to the magnetic susceptibility of air. *Magnetic Resonance in Medicine*, 56(5):1107–1113, 2006.

[43] H. Dahnke, T. Schaeffter, S. Winkelmann, R. Bowtell, and P. Börnert. Quantitative Mapping of Susceptibility Gradients from Regular Gradient Echo Images and First Application at 7T. In *Proceedings of the ISMRM*, page 1768, 2007.

[44] Y. Xu, J. A. Balschi, and C. S. Springer. Magnetic-Susceptibility Shift Selected Imaging - MESSI. *Magnetic Resonance in Medicine*, 16(1):80–90, 1990.

[45] C. H. Cunningham, T. Arai, P. C. Yang, M. V. McConnell, J. M. Pauly, and S. M. Conolly. Positive contrast magnetic resonance imaging of cells labeled with magnetic nanoparticles. *Magnetic Resonance in Medicine*, 53(5):999–1005, 2005.

[46] V. Mani, K. C. Briley-Saebo, V. V. Itskovich, D. D. Samber, and Z. A. Fayad. Gradient echo acquisition for superparamagnetic particles with positive contrast (GRASP): sequence characterization in membrane and glass superparamagnetic iron oxide phantoms at 1.5T and 3T. *Magnetic Resonance in Medicine*, 55(1):126–135, 2006.

[47] P. H. Mills and E. T. Ahrens. Sensitive positive contrast imaging of paramagnetic contrast agent distributions by visualizing phase gradients. In *Proceedings of the ISMRM*, page 525, 2007.

[48] M. Stuber, W. D. Gilson, M. Schär, D. A. Kedziorek, L. V. Hofmann, S. Shah, E. J. Vonken, J. W. M. Bulte, and D. L. Kraitchman. Positive

contrast visualization of iron oxide-labeled stem cells using Inversion-Recovery with ON-Resonant water suppression (IRON). *Magnetic Resonance in Medicine*, 58(5):1072–1077, 2007.

[49] M. E. Haacke, Y. Xu, N. Y-C. Cheng, and R. J. Reichenbach. Susceptibility weighted imaging (SWI). *Magnetic Resonance in Medicine*, 52(3):612–618, 2004.

[50] M. A. Bernstein, K. F. King, and X. J. Zhou. *Handbook of MRI pulse sequences*. Amsterdam: Elsevier, 2004.

[51] H. Dahnke, W. Liu, D. Herzka, J. A. Frank, and T. Schaeffter. Susceptibility gradient mapping SGM: A new postprocessing method for positive contrast generation applied to superparamagnetic iron oxide particle (SPIO)-labeled cells. *Magnetic Resonance in Medicine*, 60(3):595–603, 2008.

[52] C. J. G. Bakker, H. de Leeuw, K. L. Vincken, E-J. Vonken, and J. Hendrikse. Phase gradient mapping as an aid in the analysis of object-induced and system-related phase perturbations in MRI. *Physics in Medicine and Biology*, 53(18):N349–N358, 2008.

[53] E. J. P. A. Vonken, M. Schar, and M. Stuber. Positive contrast visualization of nitinol devices using susceptibility gradient mapping. *Magnetic Resonance in Medicine*, 60(3):588–594, 2008.

[54] P. H. Mills and E. T. Ahrens. Enhanced Positive-Contrast Visualization of Paramagnetic Contrast Agents Using Phase Images. *Magnetic Resonance in Medicine*, 62(5):1349–1355, 2009.

[55] F. Franconi, C. Chapon, J. J. Le Jeune, P. Richomme, and L. Lemaire. Susceptibility gradient quantization by MRI signal response mapping (SIRMA) to dephaser. *Medical Physics*, 37(2):877–884, 2010.

[56] G. Varma, R. E. Clough, P. Acher, J. Senegas, H. Dahnke, S. F. Keevil, and T. Schaeffter. Positive Visualization of Implanted Devices With Susceptibility Gradient Mapping Using the Original Resolution. *Magnetic Resonance in Medicine*, 65(5):1483–1490, 2011.

[57] J. Langley, W. Liu, E. K. Jordan, J. A. Frank, and Q. Zhao. Quantification of SPIO Nanoparticles in vivo Using the Finite Perturber Method. *Magnetic Resonance in Medicine*, 65(5):1461–1469, 2011.

[58] Q. Zhao, J. Langley, S. Lee, and W. Liu. Positive contrast technique for the detection and quantification of superparamagnetic iron oxide nanoparticles in MRI. *NMR in Biomedicine*, 24(5):464–472, 2011.

[59] H. Zhu, K. Demachi, and M. Sekino. Phase gradient imaging for positive contrast generation to superparamagnetic iron oxide nanoparticle-labeled targets in magnetic resonance imaging. *Magnetic Resonance Imaging*, 29(7):891–898, 2011.

[60] L. Li and J. S. Leigh. High-precision mapping of the magnetic field utilizing the harmonic function mean value property. *Journal of Magnetic Resonance*, 148(2):442–448, 2001.

[61] L. Li, E. M. Shapiro, and J. S. Leigh. Significant precision improvement for temperature mapping. *Magnetic Resonance in Medicine*, 46(4):678–682, 2001.

[62] L. Li. Averaging of harmonic physical fields over an annular region enclosing field sources. *American Journal of Physics*, 70(10):1029–1033, 2002.

[63] D. J. Griffiths. *Introduction to electrodynamics, 3rd edition*. New Jersey: Prentice-Hall, 1999.

[64] R. Salomir, B. D. De Senneville, and C. T. W. Moonen. A Fast Calculated Method for Magnetic Field Inhomogeneity due to an Arbitrary Distribution of Bulk Susceptibility. *Concepts in Magnetic Resonance*, 19B(1):26–34, 2003.

[65] C. G. Koay, J. E. Sarls, and E. Ozarslan. Three-dimensional analytical magnetic resonance Imaging phantom in the Fourier domain. *Magnetic Resonance in Medicine*, 58(2):430–436, 2007.

[66] Liu C. Li W, Wu B. Quantitative susceptibility mapping of human brain reflects spatial variation in tissue composition. *NeuroImage*, 55(4):1645–1656, 2011.

[67] A. Rosenfeld and A. C. Kak. *Digital picture processing*. London: Academic Press, 1976.

[68] G. Varma, S. F. Pedersen, M. Taupitz, R. M. Botnar, H. Dahnke, S. F. Keevil, and T. Schaeffter. Utilizing different methods for visualizing susceptibility from a single multi-gradient echo dataset. *Magnetic Resonance Materials in Physics Biology and Medicine*, 22(5):297–308, 2009.

[69] P. J. Van Diest. Ductal carcinoma in situ in breast carcinogenesis. *Journal of Pathology*, 187(4):383–384, 1999.

[70] G. D. Leonard and S. M. Swain. Ductal carcinoma in situ, complexities and challenges. *Journal of the National Cancer Institute*, 96(12):906–920, 2004.

[71] A. H. J. Verschuur-Maes, C. H. van Gils, M. A. A. J. van den Bosch, P. C. De Bruin, and P. J. van Diest. Digital mammography: more microcalcifications, more columnar cell lesions without atypia. *Modern Pathology*, 24(9):1191–1197, 2011.

[72] L. Feeley, D. Kiernan, T. Mooney, F. Flanagan, G. Hargaden, M. Kell, M. Stokes, and M. Kennedy. Digital mammography in a screening programme and its implications for pathology: a comparative study. *Journal of Clinical Pathology*, 64(3):215–219, 2011.

[73] X. Ying, Y. Lin, X. Xia, B. Hu, Z. Zhu, and P. He. A comparison of mammography and ultrasound in women with breast disease: a receiver operating characteristic analysis. *The breast journal*, 18(2):130–138, 2012.

[74] W. E. Barlow, C. D. Lehman, Y. Y. Zheng, R. Ballard-Barbash, B. C. Yankaskas, G. R. Cutter, P. A. Carney, B. M. Geller, R. Rosenberg, K. Kerlikowske, D. L. Weaver, and S. H. Taplin. Performance of diagnostic mammography for women with signs or symptoms of breast cancer. *Journal of the National Cancer Institute*, 94(15):1151–1159, 2002.

[75] K. Flobbe, E. S. van der Linden, A. G. H. Kessels, and J. M. A. van Engelshoven. Diagnostic value of radiological breast imaging in a non-screening population. *International Journal of Cancer*, 92(4):616–618, 2001.

[76] N. Houssami, L. Irwig, J. M. Simpson, M. McKessar, S. Blome, and J. Noakes. The contribution of work-up or additional views to the accuracy of diagnostic mammography. *Breast*, 12(4):270–275, 2003.

[77] N. Houssami, L. Irwig, J. M. Simpson, M. McKessar, S. Blome, and J. Noakes. The influence of clinical information on the accuracy of diagnostic mammography. *Breast Cancer Research and Treatment*, 85(3):223–228, 2004.

[78] J. G. Elmore, S. L. Jackson, L. Abraham, D. L. Miglioretti, P. A. Carney, B. M. Geller, B. C. Yankaskas, K. Kerlikowske, T. Onega, R. D. Rosenberg, E. A. Sickles, and D. S. M. Buist. Variability in Interpretive Performance at Screening Mammography and Radiologists' Characteristics Associated with Accuracy. *Radiology*, 253(3):641–651, 2009.

[79] A. Jensen, I. Vejborg, N. Severinsen, S. Nielsen, F. Rank, G. J. Mikkelsen, J. Hilden, D. Vistisen, U. Dyreborg, and E. Lynge. Performance of clinical mammography: A nationwide study from Denmark. *International Journal of Cancer*, 119(1):183–191, 2006.

[80] E. Warner, K. Hill, P. Causer, D. Plewes, R. Jong, M. Yaffe, W. D. Foulkes, P. Ghadirian, H. Lynch, F. Couch, J. Wong, F. Wright, P. Sun, and S. A. Narod. Prospective Study of Breast Cancer Incidence in Women With a BRCA1 or BRCA2 Mutation Under Surveillance With and Without Magnetic Resonance Imaging. *Journal of Clinical Oncology*, 29(13):1664–1669, 2011.

[81] A. P. S. van der Velden, M. S. Schlooz-Vries, C. Boetes, and T. Wobbes. Magnetic resonance imaging of ductal carcinoma in situ: what is its clinical application? A review. *American Journal of Surgery*, 198(2):262–269, 2009.

[82] F. Pediconi, S. Padula, V. Dominelli, M. L. Luciani, M. Telesca, V. Casali, M. A. Kirchin, R. Passariello, and C. Catalano. Role of Breast MR Imaging for Predicting Malignancy of Histologically Borderline Lesions Diagnosed at Core Needle Biopsy: Prospective Evaluation. *Radiology*, 257(3):653–661, 2010.

[83] J. H. Menell, E. A. Morris, D. D. Dershaw, A. F. Abramson, E. Brogi, and L. Liberman. Determination of the presence and extent of pure ductal carcinoma in situ by mammography and magnetic resonance imaging. *Breast Journal*, 11(6):382–390, 2005.

[84] M. N. Mariano, M. A. A. J. van den Bosch, B. L. Daniel, K. W. Nowels, R. L. Birdwell, K. J. Fong, P. S. Desmond, S. Plevritis, L. A. Stables, M. Zakhour, R. J. Herfkens, and D. M. Ikeda. Contrast-enhanced MRI of ductal carcinoma in situ: Characteristics of a new intensity-modulated parametric mapping technique correlated with histopathologic findings. *Journal of Magnetic Resonance Imaging*, 22(4):520–526, 2005.

[85] A. Fatemi-Ardekani, C. Boylan, and M. D. Noseworthy. Identification of breast calcification using magnetic resonance imaging. *Medical Physics*, 36(12):5429–5436, 2009.

[86] V. O. Boer, M. P. Luttje, P. R. Luijten, and D. W. J. Klomp. Bias in Breast B_0 mapping; shimming lipid rich parts of the body at 7T. In *Proceedings of the ISMRM 2012*, volume 611, May 2012.

[87] Astrid L. H. M. W. van Lier, David O. Brunner, Klaas P. Pruessmann, Dennis W. J. Klomp, Peter R. Luijten, Jan J. W. Lagendijk, and Cornelis A. T. van den Berg. $B_1(+)$ Phase mapping at 7 T and its application for in vivo electrical conductivity mapping. *Magnetic Resonance in Medicine*, 67(2):552–561, 2012.

[88] S. Klein, M. Staring, K. Murphy, M. A. Viergever, and J. P. W. Pluim. elastix: a toolbox for intensity based medical image registration. *IEEE Transactions on Medical Imaging*, 29(1):196–205, 2010.

[89] Z. Wu, S. Mittal, K. Kish, Y. Yu, J. Hu, and E. M. Haacke. Identification of calcification with MRI using susceptibility-weighted imaging: A case study. *Journal of Magnetic Resonance Imaging*, 29(1):177–182, 2009.

[90] M. Jenkinson. Fast, Automated, N-Dimensional Phase Unwrapping Algorithm. *Magnetic Resonance in Medicine*, 49:193–197, 2003.

[91] J. Langley and Q. Zhao. Unwrapping magnetic resonance phase maps with Chebyshev polynomials. *Magnetic Resonance Imaging*, 27(9):1293–1301, 2009.

[92] F. Schweser, K. H. Herrmann, A. Deistung, M. Atterbury, P. A. Baltzer, H. P. Burmeister, W. A. Kaiser, and J. R. Reichenbach. Quantitative magnetic susceptibility mapping (QSM) in breast disease reveals additional information for MR-based characterization of carcinoma and calcification. In *Proceedings of the ISMRM 2011*, 1014, May 2011.

[93] J. Mende, J. Wild, D. Ulucay, M. Radicke, A. L. Kofahl, B. Weber, R. Krieg, and K. Maier. Acoustic radiation force contrast in MRI: Detection of calcifications in tissue-mimicking phantoms. *Medical Physics*, 37(12):6347–6356, 2010.

[94] V. O. Boer, B. L. vd Bank, G. van Vliet, P. R. Luijten, and D. W. J. Klomp. Direct B_0 field monitoring and real-time B_0 field updating in the human breast at 7 tesla. *Magnetic Resonance in Medicine*, 67(2):586–591, 2012.

[95] J. F. W. Nijsen, J. H. Seppenwoolde, T. Havenith, C. Bos, C. J. G. Bakker, and A. D. V. H. Schip. Liver tumors: MR imaging of radioactive holmium microspheres - Phantom and rabbit study. *Radiology*, 231(2):491–499, 2004.

[96] H. Dahnke and T. Schaeffter. Limits of detection of SPIO at 3.0 T using $T_2^\star$ relaxometry. *Magnetic Resonance in Medicine*, 53(5):1202–1206, 2005.

[97] J. H. Seppenwoolde, J. F. W. Nijsen, L. W. Bartels, S. W. Zielhuis, A. D. V. Schip, and C. J. G. Bakker. Internal radiation therapy of liver tumors: Qualitative and quantitative magnetic resonance imaging of the biodistribution of holmium-loaded microspheres in animal models. *Magnetic Resonance in Medicine*, 53(1):76–84, 2005.

[98] N. H. G. M. Peters, C. Meeuwis, C. J. G. Bakker, W. P. Th. M. Mali, A. M. Fernandez-Gallardo, R. van Hillegersberg, M. E. I. Schipper, and M. A. A. J. van den Bosch. Feasibility of MRI-guided large-core-needle biopsy of suspiscious breast lesions at 3 T. *European Radiology*, 19(7):1639–1644, 2009.

[99] J. Dennie, J. B. Mandeville, J. L. Boxerman, S. D. Packard, B. R. Rosen, and R. M. Weisskoff. NMR imaging of changes in vascular morphology due to tumor angiogenesis. *Magnetic Resonance in Medicine*, 40(6):793–799, 1998.

[100] P. R. Seevinck, L. H. Deddens, and R. M. Dijkhuizen. Magnetic resonance imaging of brain angiogenesis after stroke. *Angiogenesis*, 13(2):101–111, 2010.

[101] J. C. Wood, C. Enriquez, N. Ghugre, J. M. Tyzka, S. Carson, M. D. Nelson, and T. D. Coates. MRI R_2 and $R_2^\star$ mapping accurately estimates hepatic iron concentration in transfusion-dependent thalassemia and sickle cell disease patients. *Blood*, 106(4):1460–1465, 2005.

[102] Z. Wu, S. Mittal, K. Kish, Y. Yu, J. Hu, and E. M. Haacke. Identification of Calcification With MRI Using Susceptibility-Weighted Imaging: A Case Study. *Journal of Magnetic Resonance Imaging*, 29(1):177–182, 2009.

[103] M. M. A. Conijn, M. I. Geerlings, G. J. Biessels, T. Takahara, T. D. Witkamp, J. J. M. Zwanenburg, P. R. Luijten, and J. Hendrikse. Cerebral Microbleeds on MR Imaging: Comparison between 1.5 and 7T. *American Journal of NeuroRadiology*, 32(6):1043–1049, 2011.

[104] J. Sedlacik, C. Kutschbach, A. Rauscher, A. Deistung, and J. R. Reichenbach. Investigation of the influence of carbon dioxide concentrations on cerebral physiology by susceptibility-weighted magnetic resonance imaging (SWI). *NeuroImage*, 43(1):36–43, 2008.

[105] S. Posse, Z. Shen, V. Kiselev, and L. J. Kemna. Single-shot $T_2^\star$ mapping with 3D compensation of local susceptibility gradients in multiple regions. *Neuroimage*, 18(2):390–400, 2003.

[106] R. Deichmann, O. Josephs, C. Hutton, D. R. Corfield, and R. Turner. Compensation of susceptibility-induced BOLD sensitivity losses in echo-planar fMRI Imaging. *Neuroimage*, 15(1):120–135, 2002.

[107] K-J. Jung, H. Peng, T. Zhao, G. Avidan, and M. Behrmann. Recovery of signal loss due to an in-plane susceptibility gradient in the gradient echo EPI through acquisition of extended phase-encoding lines. *Magnetic Resonance Imaging*, 28(6):777–783, 2010.

[108] W. G. Zhang. Conditions for Achieving Artifact-Free $T_2^\star$ Preparation in MRI. *Magnetic Resonance in Medicine*, 32(2):230–235, 1994.

[109] G. Zheng and W. S. Price. Suppression of background gradients in (B_0 gradient-based) NMR diffusion experiments. *Concepts in Magnetic Resonance*, 30A(5):261–277, 2007.

[110] H Schomberg. Off-resonance correction of MR images. *IEEE Transactions on Medical Imaging*, 18(6):481–495, 1999.

[111] W. Chen, C. T. Sica, and C. H. Meyer. Fast Conjugate Phase Image Reconstruction Based on a Chebyshev Approximation to Correct for B0 Field Inhomogeneity and Concomitant Gradients. *Magnetic Resonance in Medicine*, 60(5):1104–1111, 2008.

[112] T. Knopp, H. Eggers, H. Dahnke, J. Prestin, and J. Senegas. Iterative off-resonance and signal decay estimation and correction for multi-echo mri. *IEEE Transactions on Medical Imaging*, 28(3):394–404, 2009.

[113] J. Strand and T. Taxt. Two-dimensional phase unwrapping using robust derivative estimation and adaptive integration. *IEEE Transactions on Image Processing*, 11(10):1192–1200, 2002.

[114] R. N. Bracewell. *The Fourier Transform and Its Applications*. McGraw-Hill Book comapny, 1978.

[115] E. W. Weisstein. "Least Squares Fitting–Exponential." MathWorld–A Wolfram Web Resource, 2011.

[116] F. Testud, D. N. Splitthoff, O. Speck, J. Hennig, and M. Zaitsev. Direct Magnetic Field Estimation Based on Echo Planar Raw Data. *IEEE Transactions on Medical Imaging*, 29(7):1401–1411, 2010.

[117] N. K. Chen, C. C. Dickey, S. S. Yoo, C. R. G. Guttman, and L. P. Panych. Selection of voxel size and slice orientation for fMRI in the presence of susceptibility field gradients: application to imaging of the amygdala. *Neuroimage*, 19(3):817–825, 2003.

[118] N. K. Chen, K. Oshio, and L. P. Panych. Application of k-space energy spectrum analysis to susceptibility field mapping and distortion correction in gradient-echo EPI. *NeuroImage*, 31(2):609–622, 2006.

[119] F. K. Wacker, S. Vogt, A. Khamene, J. A. Jesberger, S. G. Nour, D. R. Elgort, F. Sauer, J. L. Duerk, and J. S. Lewin. An augmented reality system for MR image-guided needle biopsy: Initial results in a swine model. *Radiology*, 238(2):497–504, 2006.

[120] C. Perlet, A. Heinig, X. Prat, J. Casselman, L. Baath, H. Sittek, C. Stets, J. Lamarque, I. Anderson, P. Schneider, P. Taourel, M. Reiser, and S. H. Heywang-Kobrunner. Multicenter study for the evaluation of a dedicated biopsy device for MR-guided vacuum biopsy of the breast. *European Radiology*, 12(6):1463–1470, 2002.

[121] R. H. El Khouli, K. J. Macura, P. B. Barker, L. M. Elkady, M. A. Jacobs, J. Vogel-Claussen, and D. A. Bluemke. MRI-Guided Vacuum-Assisted Breast Biopsy: A Phantom and Patient Evaluation of Targeting Accuracy. *Journal of Magnetic Resonance Imaging*, 30(2):424–429, 2009.

[122] Y. Dori, M. Sarmiento, A. C. Glatz, M. J. Gillespie, V. M. Jones, M. A. Harris, K. K. Whitehead, M. A. Fogel, and J. J. Rome. X-Ray Magnetic Resonance Fusion to Internal Markers and Utility in Congenital Heart Di-

sease Catheterization. *Circulation-Cardiovascular imaging*, 4(4):415–424, 2011.

[123] M. A. Moerland, H. K. Wijrdeman, R. Beersma, C. J. G. Bakker, and J. J. Battermann. Evaluation of permanent I-125 prostate implants using radiography and magnetic resonance imaging. *International Journal of Radiation Oncology Biology Physics*, 37(4):927–933, 1997.

[124] M. R. van den Bosch, M. R. Moman, M. van Vulpen, J. J. Battermann, E. Duiveman, L. J. van Schelven, H. de Leeuw, J. J. W. Lagendijk, and M. A. Moerland. MRI-guided robotic system for transperineal prostate interventions: proof of principle. *Physics in Medicine and Biology*, 55(5):N133–N140, 2010.

[125] E. A. Petersen, E. M. Holl, I. Martinez-Torres, T. Foltynie, P. Limousin, M. I. Hariz, and L. Zrinzo. Minimizing Brain Shift in Stereotactic Functional Neurosurgery. *Neurosurgery*, 67(3):213–221, 2010.

[126] A. A. C. De Leeuw, M. A. Moerland, C. Nomden, R. H. A. Tersteeg, J. M. Roesink, and I. M. Jurgenliemk-Schulz. Applicator reconstruction and applicator shifts in 3D MR-based PDR brachytherapy of cervical cancer. *Radiotherapy and Oncology*, 93(2):341–346, 2009.

[127] V. Lagerburg, M. A. Moerland, J. H. Seppenwoolde, and J. J. W. Lagendijk. Simulation of the artefact of an iodine seed placed at the needle tip in MRI-guided prostate brachytherapy. *Physics in Medicine and Biology*, 53(5):N59–N67, 2008.

[128] G. P. Teitelbaum, W. G. Bradley, and B. D. Klein. MR Imaging artifacts, ferromagnetism, and magnetic torque of intravascular filters, stents, and coils. *Radiology*, 166(3):657–664, 1988.

[129] M. E. Ladd, P. Erhart, J. F. Debatin, B. J. Romanowski, P. Boesiger, and G. C. McKinnon. Biopsy needle susceptibility artifacts. *Magnetic Resonance in Medicine*, 36(4):646–651, 1996.

[130] M. Gawenda, A. Gossmann, K. Kruger, M. Zaehringer, M. Hahn, G. Wassmer, and J. Brunkwall. Comparison of magnetic resonance imaging and computed tomography of 8 aortic stent-graft models. *Journal of Endovascular Therapy*, 11(6):627–634, 2004.

[131] A. Glowinski, G. Adam, A. Bucker, J. van Vaals, and R. W. Gunther. A perspective on needle artifacts in MRI: An electromagnetic model for experimentally separating susceptibility effects. *IEEE Transactions on Medical Imaging*, 19(12):1248–1252, 2000.

[132] M. L. Lauzon and B. K. Rutt. Effects of polar sampling in k-space. *Magnetic Resonance in Medicine*, 36(6):940–949, 1996.

[133] D. C. Noll, J. M Pauly, C. H. Meyer, D. G. Nishimura, and A. Macovski. Deblurring for non-2D Fourier Transform Magnetic Resonance Imaging. *Magnetic Resonance in Medicine*, 25(2):319–333, 1992.

[134] P. R. Seevinck, H. de Leeuw, M. A. Moerland, and C. J. G. Bakker. Fast and Reliable Localization of Brachytherapy Seeds Using Undersampled co-RASOR. In *Proceedings of the ISMRM 2011*, May 2011.

[135] T. B. Harshbarger and D. B. Twieg. Iterative reconstruction of single-shot spiral MRI with off resonance. *IEEE Transactions on Medical Imaging*, 18(3):196–205, 1999.

[136] P. Irarrazabal, C. H. Meyer, D. G. Nishimura, and A. Macovski. Inhomogeneity correction using an estimated linear field map. *Magnetic Resonance in Medicine*, 35(2):278–282, 1996.

[137] K. S. Nayak and D. G. Nishimura. Automatic field map generation and off-resonance correction for projection reconstruction imaging. *Magnetic Resonance in Medicine*, 43(1):151–154, 2000.

[138] M. L. Lauzon and B. K. Rutt. Polar sampling in k-space: Reconstruction effects. *Magnetic Resonance in Medicine*, 40(5):769–782, 1998.

[139] P. A. Kupelian, L. Potters, D. Khuntia, J. P. Ciezki, C. A. Reddy, A. M. Reuther, T. P. Carlson, and E. A. Klein. Radical prostatectomy, external beam radiotherapy $>$ 72 Gy, external beam radiotherapy $<=$ 72 Gy, permanent seed implantation, or combined seeds/external beam radiotherapy for stage T1-T2 prostate cancer. *International Journal of Radiation Oncology Biology Physics*, 58(1):25–33, 2004.

[140] D. J. Demanes, A. A. Martinez, M. Ghilezan, D. R. Hill, L. Schour, D. Brandt, and G. Gustafson. High-Dose-Rate monotherapy: Safe and Effective Brachytherapy for patients with localized Prostate Cancer. *International Journal of Radiation Oncology Biology Physics*, 81(5):1286–1292, 2011.

[141] P. Hoskin. High dose rate brachytherapy for prostate cancer. *Cancer Radiotherapie*, 12(6-7):512–514, 2008.

[142] T. J. Polascik and V. Mouraviev. Focal therapy for prostate cancer. *Current opinion in Urology*, 18(3):269–274, 2008.

[143] C. R. King. LDR vs. HDR brachytherapy for localized prostate cancer: the view from radiobiological models. *Brachytherapy*, 1(4):219–226, 2002.

[144] F. Vicini, C. Vargas, G. Gustafson, G. Edmundson, and A. Martinez. High dose rate brachytherapy in the treatment of prostate cancer. *World Journal of Urology*, 21(4):220–228, 2003.

[145] A. Van 't Riet, A. C. A. Mak, H. J. Teloo, C. J. M. Hoekstra, and V. G. M. Althof. Verification of Source Position in Interstitial and Intralumenal Brachytherapy. *Radiotherapy and Oncology*, 33(2):167–170, 1994.

[146] L. Liu, S. C. Prasad, D. A. Bassano, J. Heavern, B. Keshler, and S. S. Hahn. A dwell position verification method for high dose rate brachytherapy. *Journal of applied clinical medical physics*, 5(1):1–5, 2004.

[147] J. Adamson and Q. Wu. Inferences about prostate intrafraction motion from pre- and posttreatment volumetric imaging. *International Journal of Radiation Oncology Biology Physics*, 75(1):260–267, 2009.

[148] M. R. Moman, C. A. T. van den Berg, A. E. Boeken-Kruger, J. J. Battermann, M. A. Moerland, U. A. van der Heide, and M. van Vulpen. Focal Salvage Guided by T_2-weighted and Dynamic Contrast-Enhanced Magnetic Resonance Imaging for Prostate Cancer Recurrences. *International Journal of Radiation Oncology Biology Physics*, 76(3):741–746, 2010.

[149] H. de Leeuw, P. R. Seevinck, and C. J. G. Bakker. Center-out radial sampling with off-resonant reconstruction for efficient and accurate localization of punctate and elongated paramagnetic structures. *Magnetic Resonance in Medicine*, 2012.

[150] G. M. Daskalov, E. Loffler, and J. F. Williamson. Monte Carlo-aided dosimetry of a new high dose-rate brachytherapy source. *Medical Physics*, 25(11):2200–2208, 1998.

[151] C. O. Schirra, S. Weiss, S. Krueger, D. Caulfield, S. F. Pedersen, R. Razavi, S. Kozerke, and T. Schaeffter. Accelerated 3D Catheter Visualization From Triplanar MR Projection Images. *Magnetic Resonance in Medicine*, 64(1):167–176, 2010.

[152] S. Kos, R. Huegli, G. M. Bongartz, A. L. Jacob, and D. Bilecen. MR-guided endovascular interventions: a comprehensive review on techniques and applications. *European Radiology*, 18(4):645–657, 2008.

[153] S. Zhang, K. T. Block, and J. Frahm. Magnetic Resonance Imaging in Real Time: Advances Using Radial FLASH. *Journal of Magnetic Resonance Imaging*, 31(1):101–109, 2010.

[154] S. Langlois, M. Desvignes, J. M. Constans, and M. Revenu. MRI geometric distortion: A simple approach to correcting the effects of non-linear gradient fields. *Journal of Magnetic Resonance Imaging*, 9(6):821–831, 1999.

[155] A. M. El-Sharkawy, M. Schar, P. A. Bottomley, and E. Atalar. Monitoring and correcting spatio-temporal variations of the MR scanner's static magnetic field. *Magnetic Resonance Materials in Physics Biology and Medicine*, 19(5):223–236, 2006.

[156] P. M. Glover. Interaction of MRI field gradients with the human body. *Physics in Medicine and Biology*, 54(21):R99–R115, 2009.

[157] T. R. Brown, B. M. Kincaid, and K. Ugurbil. NMR Chemical-Shift Imaging in 3 dimensions. *Proceedings of the National Academy of Sciences of the United States of America -Biological Sciences*, 79(11):3523–3526, 1982.

[158] T. R. Brown. Practical applications of chemical-shift imaging. *NMR in biomedicine*, 5(5):238–243, 1992.

[159] J. V. Hajnal, D. L. G. Hill, and D. J. Hawkes. *Medical Image Registration*. New York: CRC Press, 2001.

[160] W. Lu, K. B. Pauly, G. E. Gold, J. M. Pauly, and B. A. Hargreaves. SEMAC: Slice Encoding for Metal Artifact Correction in MRI. *Magnetic Resonance in Medicine*, 62(1):66–76, 2009.

[161] K. M. Koch, J. E. Lorbiecki, R. S. Hinks, and K. F. King. A Multispectral Three-Dimensional Acquisition Technique for Imaging Near Metal Implants. *Magnetic Resonance in Medicine*, 61(2):381–390, 2009.

[162] C. R. Camacho, D. B. Plewes, and R. M. Henkelman. Nonsusceptibility Artifacts due to Metallic Objects in MR-Imaging. *Journal of Magnetic Resonance Imaging*, 5(1):75–88, 1995.

[163] P. Mansfield. Spatial-Mapping of the Chemical-Shift in NMR. *Magnetic Resonance in Medicine*, 1(3):370–386, 1984.

[164] J. H. Duyn and C. T. W. Moonen. Fast Proton Spectroscopic Imaging of Human Brain using multiple Spin-Echoes. *Magnetic Resonance in Medicine*, 30(4):409–414, 1993.

[165] E. Adalsteinsson, P. Irarrazabal, S. Topp, C. Meyer, A. Macovski, and D. M. Spielman. Volumetric spectroscopic imaging with spiral-based k-space trajectories. *Magnetic Resonance in Medicine*, 39(6):889–898, 1998.

[166] U. Dydak, K. P. Pruessmann, M. Weiger, J. Tsao, D. Meier, and P. Boesiger. Parallel spectroscopic imaging with spin-echo trains. *Magnetic Resonance in Medicine*, 50(1):196–200, 2003.

[167] P. E. Z. Larson, S. Hu, M. Lustig, A. B. Kerr, S. J. Nelson, J. Kurhanewicz, J. M. Pauly, and D. B. Vigneron. Fast Dynamic 3D MR Spectroscopic Imaging With Compressed Sensing and Multiband Excitation Pulses for Hyperpolarized C-13 Studies. *Magnetic Resonance in Medicine*, 65(3):610–619, 2011.

[168] S. Emid and J. H. N. Creyghton. High-Resolution NMR Imaging in Solids. *Physica B & C*, 128(1):81–83, 1985.

[169] M. L. H. Gruwel, P. Latta, M. Tanasiewicz, V. Volotovskyy, M. Sramek, and B. Tomanek. MR imaging of teeth using a silent single point imaging technique. *Applied Physics A- Materials Science & Processing*, 88(4):763–767, 2007.

[170] P. Ramos-Cabrer, J. P. M. van Duynhoven, A. Van der Toorn, and K. Nicolay. MRI of hip prostheses using single-point methods: in vitro studies towards the artifact-free imaging of individuals with metal implants. *Magnetic Resonance Imaging*, 22(8):1097–1103, 2004.

[171] P Bendel. Echo Projection Imaging - A method to obtain NMR Images undistorted by Magnetic Field Inhomogeneities. *IEEE Transactions on Medical Imaging*, 4(2):114–119, 1985.

[172] J. B. Miller and A. N. Garroway. Removal of Static-Field Inhomogeneity and Chemical-Shift effects in NMR Imaging. *Journal of Magnetic Resonance*, 67(3):575–579, 1986.

[173] T. S. Wong and D. Rosenfeld. Spin-Inversion Imaging - A technique for NMR Imaging under magnetic-fields with High-Field nonuniformities. *IEEE Transactions on Medical Imaging*, 6(2):148–156, 1987.

[174] J. C. Sharp, R. W. Bowtell, and P. Mansfield. Elimination of Susceptibility distortions and reduction of diffusion attenuation in NMR microscopy by line-narrowed 2DFT. *Magnetic Resonance in Medicine*, 29(3):407–410, 1993.

[175] D. J. O. McIntyre, F. Hennel, and P. G. Morris. SPARE: A robust method for magnetic resonance imaging in inhomogeneous fields. *Journal of Magnetic Resonance*, 130(1):58–62, 1998.

[176] S. D. Beyea, B. J. Balcom, I. V. Mastikhin, T. W. Bremner, R. L. Armstrong, and P. E. Grattan-Bellew. Imaging of heterogeneous materials with a turbo spin echo single-point imaging technique. *Journal of Magnetic Resonance*, 144(2):255–265, 2000.

[177] B. J. Balcom, R. P. MacGregor, S. D. Beyea, D. P. Green, R. L. Armstrong, and T. W. Bremner. Single-point ramped imaging with T-1 enhancement (SPRITE). *Journal of Magnetic Resonance Series A*, 123(1):131–134, 1996.

[178] Z. H. Cho and Y. M. Ro. Multipoint K-space Point Mapping (KPM) technique for NMR Microscopy. *Magnetic Resonance in Medicine*, 32(2):258–262, 1994.

[179] P. Latta, M. L. H. Gruwel, V. Volotovskyy, M. H. Weber, and B. Tomanek. Single-point imaging with a variable phase encoding interval. *Magnetic Resonance Imaging*, 26(1):109–116, 2008.

[180] P. Parasoglou, D. Malioutov, A. J. Sederman, J. Rasburn, H. Powell, L. F. Gladden, A. Blake, and M. L. Johns. Quantitative single point imaging with compressed sensing. *Journal of Magnetic Resonance*, 201(1):72–80, 2009.

[181] C. O. Schirra, S. Weiss, S. Krueger, S. F. Pedersen, R. Razavi, T. Schaeffter, and S. Kozerke. Toward True 3D Visualization of Active Catheters Using Compressed Sensing. *Magnetic Resonance in Medicine*, 62(2):341–347, 2009.

[182] J. Yerly, M. L. Lauzon, H. S. Chen, and R. Frayne. A Simulation-Based Analysis of the Potential of Compressed Sensing for Accelerating Passive MR Catheter Visualization in Endovascular Therapy. *Magnetic Resonance in Medicine*, 63(2):473–483, 2010.

[183] M. Lustig, D. Donoho, and J. M. Pauly. Sparse MRI: The application of compressed sensing for rapid MR imaging. *Magnetic Resonance in Medicine*, 58(6):1182–1195, 2007.

[184] R. M. Hoogeveen, C. J. G. Bakker, and M.A. Viergever. MR phase-contrast flow measurement with limited resolution in small vessels: value of model-based image analysis. *Magnetic Resonance in Medicine*, 41:520–528, 1999.

[185] G. H. van de Maat, P. R. Seevinck, C. Bos, and C. J. G. Bakker. Quantification of holmium-166 loaded microspheres: estimating high local concentrations using a conventional multiple gradient echo sequence with S0-fitting. *Journal of Magnetic Resonance Imaging*, 35(6):1453–1461, 2012.

[186] G. Morell and D. Spielman. Dynamic shimming for multi-slice magnetic resonance imaging. *Magnetic Resonance in Medicine*, 38:477–483, 1997.

[187] N. De Zanche, C. Barmet, J. A. Nordmeyer-Massner, and K. P. Pruessmann. NMR probes for measuring magnetic fields and field dynamics in MR systems. *Magnetic Resonance in Medicine*, 60(1):176–186, 2008.

[188] B. J. Wilm, C. Barmet, M. Pavan, and K. P. Pruessmann. Higher order reconstruction for MRI in the presence of spatiotemporal field perturbations. *Magnetic Resonance in Medicine*, 65(6):1690–1701, 2011.

[189] B. J. Wilm, C. Barmet, and K. P. Pruessmann. Fast Higher-Order MR Image Reconstruction Using Singular-Vector Separation. *IEEE Transactions on Medical Imaging*, 31(7):1396–1403, 2012.

[190] J. Anders, P. SanGiorgio, X. Deligianni, F. Santini, K. Scheffler, and G. Boero. Integrated active tracking detector for MRI-guided interventions. *Magnetic Resonance in Medicine*, 67(1):290–296, 2012.

[191] S. Patil, O. Bieri, P. Jhooti, and K. Scheffler. Automatic Slice Positioning (ASP) for Passive Real-Time Tracking of Interventional Devices Using Projection-Reconstruction Imaging with Echo-Dephasing (PRIDE). *Magnetic Resonance in Medicine*, 62(4):935–942, 2009.

[192] B. B. Frericks, D. R. Elgort, C. Hillenbrand, J. L. Duerk, J. S. Lewin, and F. K. Wacker. Magnetic Resonance Imaging-Guided Renal Artery Stent Placement in a Swine Model: Comparison of Two Tracking Techniques. *Acta Radiologica*, 50(1):21–27, 2009.

[193] A. de Oliveira, J. Rauschenberg, D. Beyersdorff, W. Semmler, and M. Bock. Automatic passive tracking of an endorectal prostate biopsy device using phase-only cross-correlation. *Magnetic Resonance in Medicine*, 59(5):1043–1050, 2008.

[194] M. Bock, S. Muller, S. Zuehlsdorff, P. Speier, C. Fink, P. Hallscheidt, R. Umathum, and W. Semmler. Active catheter tracking using parallel MRI and real-time image reconstruction. *Magnetic Resonance in Medicine*, 55(6):1454–1459, 2006.

[195] H. F. Smits, C. Bos, R. van der Weide, and C. J. G. Bakker. Interventional MR: vascular applications. *European Radiology*, 9(8):1488–1495, 1999.

[196] J. J. Derakhshan and J. L. Duerk. Update to pulse sequences for interventional mr imaging. *Magn Reson Imaging Clin N Am*, 13(3):415–429, 2005.

[197] S. P. Crijns, C. J. G. Bakker, P. R. Seevinck, de Leeuw H., J. J. Lagendijk, and B. W. Raaymakers. Towards inherently distortion-free MR images for image-guided radiotherapy on an MRI accelerator. *Physics in Medicine and Biology*, 57(5):1349–1358, 2012.

[198] T. Liu, P. Spincemaille, L. de Rochefort, R. Wong, M. Prince, and Y. Wang. Unambiguous identification of superparamagnetic iron oxide particles through quantitative susceptibility mapping of the nonlinear response to magnetic fields. *Magnetic Resonance Imaging*, 28(9):1383–1389, 2010.

[199] L. de Rochefort, T. Liu, B. Kressler, J. Liu, P. Spincemaille, V. Lebon, J. Wu, and Y. Wang. Quantitative susceptibility map reconstruction from mr phase data using bayesian regularization: validation and application to brain imaging. *Magnetic Resonance in Medicine*, 63:194–206, 2010.

[200] T. Liu, P. Spincemaille, de Rochefort L., B. Kressler, and Y. Wang. Calculation of susceptibility through multiple orientation sampling (COSMOS): a method for conditioning the inverse problem from measured magnetic field map to susceptibility source image in MRI. *Magnetic Resonance in Medicine*, 61(1):196–204, 2009.

[201] S. Wharton, A. Schäfer, and R. Bowtell. Susceptibility mapping in the human brain using threshold-based k-space division. *Magnetic Resonance in Medicine*, 63(5):1292–1304, 2010.

[202] K. Shmueli, J. A. de Zwart, P. van Gelderen, T. Q. Li, S. J. Dodd, and J. H. Duyn. Magnetic susceptibility mapping of brain tissue in vivo using MRI phase data. *Magnetic Resonance in Medicine*, 62(6):1510–1522, 2009.

[203] J. Li, S. Chang, T. Liu, Q. Wang, D. Cui, X. Chen, M. Jin, B. Wang, M. Pei, C. Wisnieff, P. Spincemaille, M. Zhang, and Y. Wang. Reducing the object orientation dependence of susceptibility effects in gradient echo MRI through quantitative susceptibility mapping. *Magnetic Resonance in Medicine*, 2012.

[204] W. Li, B. Wu, A. V. Avram, and C. Liu. Magnetic susceptibility anisotropy of human brain in vivo and its molecular underpinnings. *NeuroImage*, 59(3):2088–2097, 2012.

[205] H. de Leeuw, M. Conijn, P. R. Seevinck, J. Hendrikse, G. H. van de Maat, and C. J. G. Bakker. Characterization of local field disturbances through phase derivative mapping. In *Proceedings of the ISMRM 2010*, volume 5359, May 2010.

[206] H. J. Kuijf, H. de Leeuw, C. J. G. Bakker, and K. L. Vincken. Powerful detection of cerebral microbleeds on 7.0T MR phase gradient magnitude images using the radial symmetry transform. In *Proceedings of the ISMRM 2012*, volume 1066, May 2012.

[207] M. A. D. Vente, T. C. de Wit, M. A. A. J. van den Bosch, W. Bult, P. R. Seevinck, B. A. Zonnenberg, H. W. A. M. de Jong, G. C. Krijger, C. J. G. Bakker, A. D. van het Schip, and J. F. W. Nijsen. Holmium-166 poly(L-lactic acid) microsphere radioembolisation of the liver: technical aspects studied in a large animal model. *European Radiology*, 20(4):862–869, 2010.

[208] S. M. Sprinkhuizen, C. J. G. Bakker, and L. W. Bartels. Absolute MR Thermometry Using Time-Domain Analysis of Multi-Gradient-Echo Magnitude Images. *Magnetic Resonance in Medicine*, 64(1):239–248, 2010.

Writing a book is an adventure. To begin with it is a toy and amusement. Then it becomes a mistress, then it becomes a master, then it becomes a tyrant. The last phase is that just as you are about to be reconciled to your servitude, you kill the monster and fling him out to the public

W. Churchill

CHAPTER 12

Publications

Papers in international journals:

- G.H. van de Maat, P.R. Seevinck, M. Elschot, M.L.J. Smits, H. de Leeuw, A.D. van het Schip, M.A.D. Vente, B.A. Zonnenberg, H.W.A.M. de Jong, M.G.E.H. Lam, M.A. Viergever, M.A.A.J. van den Bosch, J.F.W. Nijsen, and C.J.G. Bakker. MRI-based biodistribution assessment of holmium-166 poly(L-lactic acid) microspheres after radioembolisation *European Radiology* DOI 10.1007/s00330-012-2648-2

- H. de Leeuw, P.R. Seevinck, and C.J.G. Bakker. Center-out radial sampling with off-resonant reconstruction for efficient and accurate localization of punctate and elongated structures. (*MRM accepted*)

- C.J.G. Bakker, H. de Leeuw, G.H. van de Maat, J.S. van Gorp, J.G. Bouwman, and P.R. Seevinck. On the utility of spectroscopic imaging as a tool for generating geometrically accurate MR images and parameter maps in the presence of field inhomogeneities and chemical shift effects (*MRI* accepted)

- C.J.G. Bakker, H. de Leeuw, and P.R. Seevinck. Selective depiction of susceptibility transitions using Laplace-filtered phase maps *Magnetic Resonance Imaging*, 30(5):601-609, 2012

- S.P.M. Crijns, C.J.G. Bakker, P.R. Seevinck, H. de Leeuw, J.J.W. Lagendijk, and B.W. Raaymakers. Distortion free MR images for IGRT on an MRI-accelerator *Physics in Medicine and Biology* 57(5) 1349-1358, 2012

- T. Waelbers, K. Peremans, S. Vermeire, K. Piron, M. Doom, V.O. Boer, H. de Leeuw, M.A.D. Vente, A. Dobbeleir, I. Gielen, K. Audenaert, and I. Polis. Effects of medetomidine and ketamine on the regional cerebral blood flow in cats: A SPECT study *Veterinary Journal* 192(1) 81-88, 2012

- H. de Leeuw, and C.J.G. Bakker. Correction of gradient echo images for first and second order macroscopic signal dephasing using phase derivative mapping *NeuroImage* 60(1) 818-829, 2012

- W. Bult, H. de Leeuw, O.M. Steinebach, M.J. van der Bom, H.Th. Wolterbeek, R.M.A. Heeren, C.J.G. Bakker, A.D. van het Schip, W.E. Hennink, and J.F.W. Nijsen. Radioactive Holmium Acetylacetonate Microspheres for Interstitial Microbrachytherapy: An In Vitro and In Vivo Stability Study. *Pharmaceutical Research* 29(3) 827-836, 2012

- P. Seevinck, H. de Leeuw, C. Bos, and C. Bakker. Highly localized positive contrast of small paramagnetic objects using 3D center-out RAdial Sampling with Off-Resonance reception. *Magnetic Resonance in Medicine* 65:146-156, 2011

- M. van den Bosch, H. de Leeuw, J.J.M. Zwanenburg, J.J.W. Lagendijk, and M.A. Moerland. Single shot MR tagging to quantify local tissue deformation during MRI-guided needle interventions: A feasibility study. *Medical Physics* 38:5321-5329, 2011

- M. van den Bosch, M. Moman, M. van Vulpen, J. Battermann, E. Duiveman, L. van Schelven, H. de Leeuw, J. Lagendijk, and M. Moerland. MRI guided robotic system for transperineal prostate interventions: proof of principle. *Physics in Medicine and Biology*, 55(5):N133-N140, 2010

- W. Bult, R. Varkevisser, F. Soulimani, P. Seevinck, H. de Leeuw, C. Bakker, P. Luijten, A. van Het Schip, W. Hennink, and J. Nijsen. Holmium nanoparticles:preparation and in vitro characterization of a new device for radioablation of solid malignancies. *Pharm Res*, 27:2205-2012, 2010

- T. Waelbers, K. Peremans, S. Vermeire, K. Piron, K. Audenaert, A. Dobbeleir, V. Boer, H. de Leeuw, M. Vente, and I. Polis.Medetomidine alone and in combination with ketamine causes changes in the regional cerebral blood flow measured with single photon emission computed tomography in cats. *Journal of Nuclear Medicine and molecular imaging*, 37: S352-S353, 2010

- C.J.G. Bakker, H. de Leeuw, K.L. Vincken, E-J. Vonken, and J. Hendrikse. Phase gradient mapping as an aid in the analysis of object-induced and system-related phase perturbations in MRI. *Physics in Medicine and Biology*, 53(18):N349-N358, 2008

Begegnet uns jemand, der uns Dank schuldig ist, gleich fällt es uns ein. Wie oft können wir jemand begegnen, dem wir Dank schuldig sind, ohne daran zu denken

J. W. von Goethe

CHAPTER 13

Dankwoord

Dit laatste gedeelte van het proefschrift is een van de moeilijkste gedeeltes, aangezien dit de uitgelezen mogelijkheid is om de vele mensen die ik dank ben verschuldigd ben, deze dank ook te geven. Helaas is de lijst van mensen die ik wil bedanken te lang om in dit stuk aan een ieder persoonlijk het woord te richten. Een aantal mensen wil ik echter graag in het bijzonder noemen.

Allereerst wil ik graag mijn co-promotor bedanken. Chris, je hebt mij op ongelooflijk veel manieren geholpen. Allereerst, heb ik dankzij jou kunnen promoveren in deze groep. Daarnaast was je de hele tijd een goede basis om op terug te kunnen vallen. Je hebt me geleerd hoe je onderzoek goed vormgeeft en je enthousiasme werkte aanstekelijk. Tijdens de scanavonden heb ik geleerd hoe de scanner werkt en dit waar nodig te omzijlen, dank daarvoor! Het grote aantal experimenten, besprekingen van resultaten, en vooral ook kritische revisies van grote stukken tekst die ik je stuurde zijn van onschatbare waarde. Het aantal revisies dat je hebt gemaakt van mijn stukken vult waarschijnlijk enkele papiercontainers. Ik zal de discussies over MRI, de behaalde resultaten en het wielrennen ook zeker gaan missen. Veel dank dat je mij hebt willen begeleiden!

Ook mijn promotor wil ik bedanken. Max, ik vind het bewonderingswaardig hoe je zo'n grote diverse groep managed en toch bij iedereen een vinger aan de pols houdt. Het best kan ik mijn dank omschrijven aan de hand van een uitspraak van een franse schrijver, Henry de Montherlant: *"Jonge mensen hebben geen meesters nodig om te leren denken, maar om hun weg te vinden"*. Dank voor het mogelijk maken om mijn eigen weg te kiezen en gaan en voor de juiste aanwijzingen op de momenten dat dit nodig was.

Rien Moerland, over de jaren hebben we vaak samen mogen werken. In eerste instantie, samen met Michiel, aan het robotproject en later ook voor het tracken van de HDR-brachytherapiebron met co-RASOR. Je kritische, betrokken en vooruitstrevende instelling zorgt er voor dat projecten op een prettige en goede manier blijven lopen. Het was ontzettend fijn om met je samen te werken en ik hoop in de toekomst nog vaker met je samen te kunnen werken. Bedankt voor de discussies en al je hulp.

Peter Seevinck, vaak was je lijdend voorwerp als ik een onderwerp of probleem scherper moest stellen of formuleren. Meer dan eens leek het of we het oneens waren, wat leidde tot vurige discussies. Vaak echter begrepen we elkaar niet goed. Mijn kennis en inzicht zijn mede dankzij die discussies met grote sprongen vooruit gegaan. Het was goed om samen, vanuit twee verschillende inzichten, tot een mooi geheel te komen. Bedankt voor alle discussies en input. Veel goeds samen met Doreen en Floor.

Michiel van de Bosch, ook met jou was het prettig samenwerken. De sca-

navonden waren altijd gezellig en liepen door je nauwkeurige manier van werken vrijwel altijd vlekkeloos. Samen met jou heb ik veel mogen leren op het gebied van de tracking, interventie robots en MRI veiligheid. Ook de vele discussies over de MRI fysica hebben me geholpen om dit duidelijk op een rijtje te krijgen. Bedankt en veel succes in Eindhoven. Ik hoop dat je vooruitstrevende instelling je als klinisch fysicus (in opleiding) ook zo goed af blijft gaan!

De konijnexperimenten samen met Wouter Bult waren, op een goede manier, altijd een feest. Helaas was het resultaat van het scannen van de konijnen niet wat je ervan hoopte, maar ik heb met veel plezier samen met jou de resultaten geacquireerd en beoordeeld. Het was fijn om samen met een betrokken en bevlogen persoon die vrijdagmiddag experimenten uit te voeren. Ik heb bewondering voor de respectvolle en nauwgezette manier waarop je de experimenten uitvoerde. Ik heb nu nog baat bij alle kennis die we hebben opgedaan toen we de scans hebben geoptimaliseerd om binnen een zo kort mogelijke tijd zo veel mogelijk resultaat te boeken. Daarnaast natuurlijk ook bedankt voor al je hulp bij het oplossen van de chemische problemen waar die rare fysici af en toe mee komen.

Af en toe had ik het medelijden met mensen die met mij samen moesten werken. Bertine Stehouwer, wellicht heb jij wel het meest met mij te stellen gehad. Alle rare, bijna niet te interpreteren beelden van fantomen en *ex vivo* materiaal, die ik je voorschotelde moeten je af en toe angst hebben ingeboezemd. Daarnaast hebben we veel moeten experimenteren en lang gewacht op goede samples en resultaten. Gelukkig is het uiteindelijk gelukt. Bedankt voor de gezellige scanuurtjes en veel succes met het afronden van je eigen promotie!

Mijn kamergenoot, Gerrit, bedankt voor alle discussies en adviezen. Het was fijn om een kamergenoot te hebben waar ik af en toe een snelle, domme vraag aan kon stellen. Ook op de conferenties was je een gezellige kamergenoot. Veel succes met het afronden van je eigen promotie. Ook veel goeds samen met Berdien, Noah en jullie toekomstige nieuwe gezinslid.

Graag wil ik ook graag alle coauteurs van alle artikelen waaraan ik heb (mee)gewerkt bedanken voor de discussies, inzichten en revisies. Bas, Bernard, Clemens, Chris, Dennis, Ed, Evert-Jan, Fred, Frank, Hugo, Jaco, Jan, Jeroen, Job, Koen, Leonard, Maaike, Maarten Vente, Maarten Smits, Mandy, Marnix, Martijn, Maurice, Marco, Mattijs, Paul, Peter, Sjoerd Crijns, Sjoerd van Gorp, Tim, Vincent, Wim en Wouter bedankt dat ik deel uit mocht maken van de teams die al die ideeën tot een eindproduct hebben gemaakt!

Over de jaren heb ik ook een aantal studenten mogen begeleiden en/of

helpen. Bart, Hasna, Jessica, Job en Rik, bedankt voor alles wat jullie mij ook hebben geleerd. Veel succes met jullie verdere carrière!

Veel dank gaat ook uit naar alle mensen die mij geholpen hebben met de zogenaamde randzaken. Ondanks dat ik op hen gelukkig niet te vaak een beroep hoefde te doen ben ik ze zeker dankbaar, aangezien ze, juist als je ze niet te vaak nodig hebt, goed werk voor je hebben geleverd. Jacqueline, Marjan, Renée bedankt voor alle administratieve zaken die jullie voor mij hebben geregeld. Daarnaast ook bedankt voor de gezellige gesprekken als ik eens langskwam en natuurlijk ook voor de door jullie goed georganiseerde groepsuitjes zoals de Sinterklaasviering. Gerard, bedankt voor het oplossen van al mijn pc problemen en vaak op de korte termijn die daarvoor zo fijn is. Remmert, bedankt voor alle ondersteuning in het lab. Het was erg fijn om voor de problemen op het scheikunde vlak op je terug te kunnen vallen.

In de eerste jaren heb ik veel gehad aan het scriptje om mijn data om te zetten naar een leesbaar bestandsformaat. Sandra, bedankt voor het scriptje dat je daarvoor had geschreven. Natuurlijk ook bedankt voor alle gesprekken en adviezen voor de promotie. Je was een gezellige kamergenoot!

Als vaste kracht in de koffiekamer heb ik vaak gezellige discussies gehad, verhalen kunnen vertellen en verhalen mogen horen. Het is fijn om af en toe wat frustraties te kunnen delen met mensen die ongeveer op hetzelfde punt in hun promotietraject zitten. In het bijzonder wil ik Hugo, Jeroen, Maartje en Sjoerd hiervoor bedanken.

Over alle jaren heb ik veel collega's en ganggenoten gehad. Het was fijn om over koetjes en kalfjes te praten al dan niet letterlijk (Nynke), stukjes te filmen, gewoon het nieuws te bespreken of om gezellig mee te borellen op vrijdag, op conferenties of omdat we er aan toe waren. Agnes, Alexander Leemans, Alexander Schmitz, Alessandro, Anette, Anja, Anna, Anne, Arnold, Astrid, Bastiaan, Bruno, Casper, Catalina, Chantal, Chris Oerlemans, Christian, Daniël, Erik, Evelien, Ewoud, Floor, Floris, Fredy, Hans, Harriët, Hugo, Ivan, Ivana, Jan-Henry, Jeroen Siero, Joana, Joffrey, Josien, Jurriaan, Kajo, Kenneth, Lisette Charbonnier, Lisette Deddens, Maaike, Marco, Marijn, Mariska, Marja, Mark, Marloes, Miekee, Mies, Mitko, Nicky, Nynke, Özlem, Patrik, Paul Baron, Paul Smeets, Pavel, Pieter, Pim, Rick, Robin, Roel, Sabina, Sara, Sascha, Thessa, Thomas, Ula, Umesh, Wilbert, Wim, Wouter, Wout-jan, Wybe, Yinghe en Yolanda, bedankt voor de gezelligheid!

Naast alle werkgerelateerde bedankjes wil ik ook graag mensen bedanken die daar buiten belangrijk zijn. Zij hebben de basis gevormd om dit alles voor mij mogelijk te maken.

Allereerst wil ik hier mijn schoonfamilie bedanken. Oscar, Jos & Yvonne,

bedankt dat jullie me zo welkom hebben laten voelen. Sorry dat ik de laatste periode weinig tijd meer voor jullie over had, gelukkig kan ik de komende tijd vaker langskomen. Ik kom graag binnenkort weer eens gezellig een spel met jullie spelen... en zal natuurlijk mijn best doen deze ook te winnen ;).

Marius, Hans en Arie-Willem, mijn broers. Lang hebben we samen onder een dak geleefd en veel met elkaar beleefd. Af en toe mis ik dat wel. Marius, veel succes met je post-doc in Zwitserland. Hans jij succes met het laatste jaar van je PhD in Reading. Arie-Willem, als laatste kon je natuurlijk niet achterblijven. Jij ook veel succes met je PhD in Utrecht. Ik kom graag nog eens een wielerkoersje of andere sportwedstrijd met je kijken.

Pa & Moe, ik weet dat jullie liever niet uitgebreid genoemd willen worden. Toch, kort en krachtig. Fijn dat jullie alle tijd achter me hebben gestaan en alles met me mee wilden beleven. Het is leuk dat jullie mijn paranimfen willen zijn op deze dag!

Ilona, mijn lieve vrouw. Het mooiste aan mijn tijd bij het ISI is zeker dat ik jou heb ontmoet. Ik ben erg blij dat je met me wilde trouwen. Doordat ik je in de laatste periode van mijn promotie ben tegengekomen had ik het constant druk en is de tijd voorbij gevlogen. Vooral het laatste jaar was pittig en moest je wel eens genoegen nemen met minder aandacht. Hopelijk wordt dit het begin van een wat rustigere periode. Ik heb zin om nog lang zo gelukkig met je te blijven!

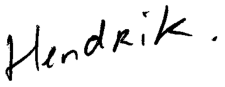

Make it thy business to know thyself, which is the most difficult lesson in the world

M. de Cervantes

CHAPTER 14

Curriculum vitae

I, Hendrik de Leeuw, was born the 9th of August 1984 in Schoonrewoerd, the Netherlands. In 2002 I graduated from secondary school, VWO at the Heerenlanden College in Leerdam. In 2002 I started the bachelor physics, which I finished in 2005. After the bachelor Physics, I started the master programme Biomedical Image Sciences at the Image Science Institute at the University Medical Center Utrecht. In the autumn 2006 I started the master research project entitled "Phase derivative mapping", under supervision of dr. Chris Bakker. On the first of April 2008 I joined the MR physics group of the same institute as a PhD student on the subject "Magnetic resonance imaging-guided internal radiation therapy of liver tumors with holmium-loaded microspheres". The results obtained during this period are presented in this thesis.

Index